universität wien

DISSERTATION / DOCTORAL THESIS

Titel der Dissertation /Title of the Doctoral Thesis

„Characterising the Relationship Between the Magnetic Response and Architecture of Magnetic Filaments“

verfasst von / submitted by

Deniz Mostarac MSc

angestrebter akademischer Grad / in partial fulfilment of the requirements for the degree of

Doktor der Naturwissenschaften (Dr. rer. Nat.)

Wien, 2022 / Vienna 2022

Studienkennzahl lt. Studienblatt / degree programme code as it appears on the student record sheet:	A 796 605 411
Dissertationsgebiet lt. Studienblatt / field of study as it appears on the student record sheet:	Physik
Betreut von / Supervisor:	Univ.-Prof. Dr. Sofia Kantorovich, Privatdoz.

ABSTRACT

Polymeric, stimuli-responsive materials are one of the central research topics in modern soft mater physics. This thesis is a study of polymer-like structures with magnetic nanoparticles as monomers, systems that emerged in attempts to capitalize on the potential of magneto-responsive materials, commonly referred to as magnetic filaments. Using magnetic fields as a stimulus is interesting because of the dynamic intensity control and/or great spatial resolution that can be achieved with them, in addition to the fact that they typically do not interfere with biological tissues and processes.

Using Molecular dynamics simulations as the principal tool of investigation, we encompass key elements of magnetic filament design: microstructure, crosslinking, magnetic nature and shape of monomers, and systematically relate them to the properties of a single filament at equilibrium and its rheological response to shear flow. Furthermore, we explore the effects of van der Waals and electrostatic forces in terms of a central attraction between the monomers of a filament, and using the Lattice-Boltzmann method, encompass hydrodynamic effects on the rheology of magnetic filaments.

A magnetic filament, as a representative member of highly magneto-responsive, smart nanomaterials, is a compelling system only as far as it has a flexible backbone and a highly tunable microstructure. Flexible, nanoscopic magnetic filaments, with a finely tunable microstructure, have not been synthesized yet. The key difficulty in such an endeavor is instilling selective, anisotropic interactions between nanoobjects that are otherwise entirely isotropic, with colloids that are chemically stable and when crosslinked, remain so permanently. To this end, we present a theoretical investigation of magnetic filaments based on DNA nanochambers, nanoobjects that have been used to synthesize nanopolymers. We analyze their mechanical response to compression and study the rheology of magnetic filaments based on DNA nanochambers, subjected to the simultaneous action of shear flow and a stationary external magnetic field perpendicular to the flow. We demonstrate that DNA nanochambers represent a compelling, finely tunable platform for creating highly magneto-responsive, nanoscopic, polymer-like structures.

ZUSAMMENFASSUNG

Eines der zentralen Forschungsthemen der modernen Physik der weichen Materie sind Polymer-artige, auf Stimuli reagierende Materialien. In dieser Dissertation werden polymerähnliche Strukturen, deren Monomere aus magnetischen Nanopartikeln bestehen, sogenannte magnetic filaments, untersucht. Diese Systeme wurden entwickelt, um das Potenzial magnetisch reagierender Materialien auszuschöpfen. Der Einsatz von Magnetfeldern als Stimulus ist wünschenswert, da sich mit ihnen dynamische Intensitätskontrolle und hohe räumliche Auflösung erzielen lassen, und da Magnetfelder in der Regel nicht mit biologischem Gewebe oder Prozessen interferieren.

Durch die Nutzung von Molekulardynamik-Simulationen als Untersuchungsmethodik erfassen wir die Schlüsselelemente des Designs magnetischer Filamente: Mikrostruktur, Vernetzung, magnetische Eigenschaften und Form der Monomere, und setzen sie systematisch in Beziehung zu den Eigenschaften eines einzelnen Filaments im thermodynamischen Gleichgewicht und seiner rheologischen Reaktion auf Scherströmung. Darüber hinaus erforschen wir die Auswirkungen von van der Waals- und elektrostatischen Kräften in Bezug auf die zentrale Anziehung zwischen den Monomeren und nutzen die Lattice-Boltzmann Methode, um die Auswirkungen der Hydrodynamik auf die Rheologie von magnetischen Filamenten zu erfassen.

Ein magnetisches Filament als Exemplar von hochmagnetisch reagierenden, "smart"-en Nanomaterialien ist nur dann von Interesse, wenn es ein flexibles Rückgrat und eine hochgradig abstimmbare Mikrostruktur aufweist. Solche nanoskopischen magnetischen Filamente wurden bisher noch nicht synthetisiert. Die Hauptschwierigkeit bei einem solchen Unterfangen besteht darin, selektive, anisotrope Wechselwirkungen zwischen Nanoobjekten, die ansonsten isotrop sind, mit Kolloiden zu erzeugen, die chemisch stabil sind und im Falle einer Vernetzung dauerhaft so bleiben. Zu diesem Zweck präsentieren wir eine theoretische Untersuchung von magnetischen Filamenten auf der Grundlage von DNA-Nanokammern, das bedeutet von Nanoobjekten, die zur Synthese von Nanopolymeren verwendet wurden. Wir analysieren die mechanische Reaktion auf Kompression und die Rheologie von magnetischen Filamenten auf der Basis von DNA-Nanokammern, die der gleichzeitigen Wirkung eines Scherflusses und eines stationären externen Magnetfeldes senkrecht zum Fluss ausgesetzt sind. Wir zeigen, dass DNA-Nanokammern eine überzeugende, fein abstimmbare Plattform für die Schaffung hochgradig magnetisch reagierender, nanoskopischer, polymerähnlicher Strukturen darstellen.

PUBLICATIONS

Some ideas, paragraphs, tables and figures in this thesis have been previously published as a part of peer-reviewed journal articles or are a part of a submitted manuscript in peer-review. A list of these articles can be found bellow:

[1] Deniz Mostarac and Sofia Kantorovic. "Rheology of a nanopolymer, synthesised through directional assembly of DNA nanochambers, for magnetic applications." Article submitted. 2022.

[2] Deniz Mostarac, EV Novak, Pedro A Sánchez, and SS Kantorovich. "The impact of magnetic field on the conformations of supracolloidal polymer-like structures with super-paramagnetic monomers." In: *Journal of Molecular Liquids* 305 (2020), p. 112761.

[3] Deniz Mostarac, Pedro A Sánchez, and Sofia Kantorovich. "Characterisation of the magnetic response of nanoscale magnetic filaments in applied fields." In: *Nanoscale* 12.26 (2020), pp. 13933–13947.

[4] Deniz Mostarac, Leo Vaughan, Pedro A Sánchez, and Sofia S Kantorovich. "The influence of crosslinkers and magnetic particle distribution along the filament backbone on the magnetic properties of supracolloidal linear polymer-like chains." In: *Journal of Magnetism and Magnetic Materials* 497 (2020), p. 166029.

[5] Deniz Mostarac, Yan Xiong, Oleg Gang, and Sofia Sergeevna Kantorovich. "Nanopolymers for magnetic applications: how to choose the architecture?" In: *Nanoscale* (2022).

[6] Yan Xiong, Zhiwei Lin, Deniz Mostarac, Brian Minevich, Qiuyuan Peng, Guolong Zhu, Pedro A Sánchez, Sofia Kantorovich, Yonggang Ke, and Oleg Gang. "Divalent Multilinking Bonds Control Growth and Morphology of Nanopolymers." In: *Nano Letters* 21.24 (2021), pp. 10547–10554.

Volume 12
Number 26
14 July 2020
Pages 13843-14300

Nanoscale

rsc.li/nanoscale

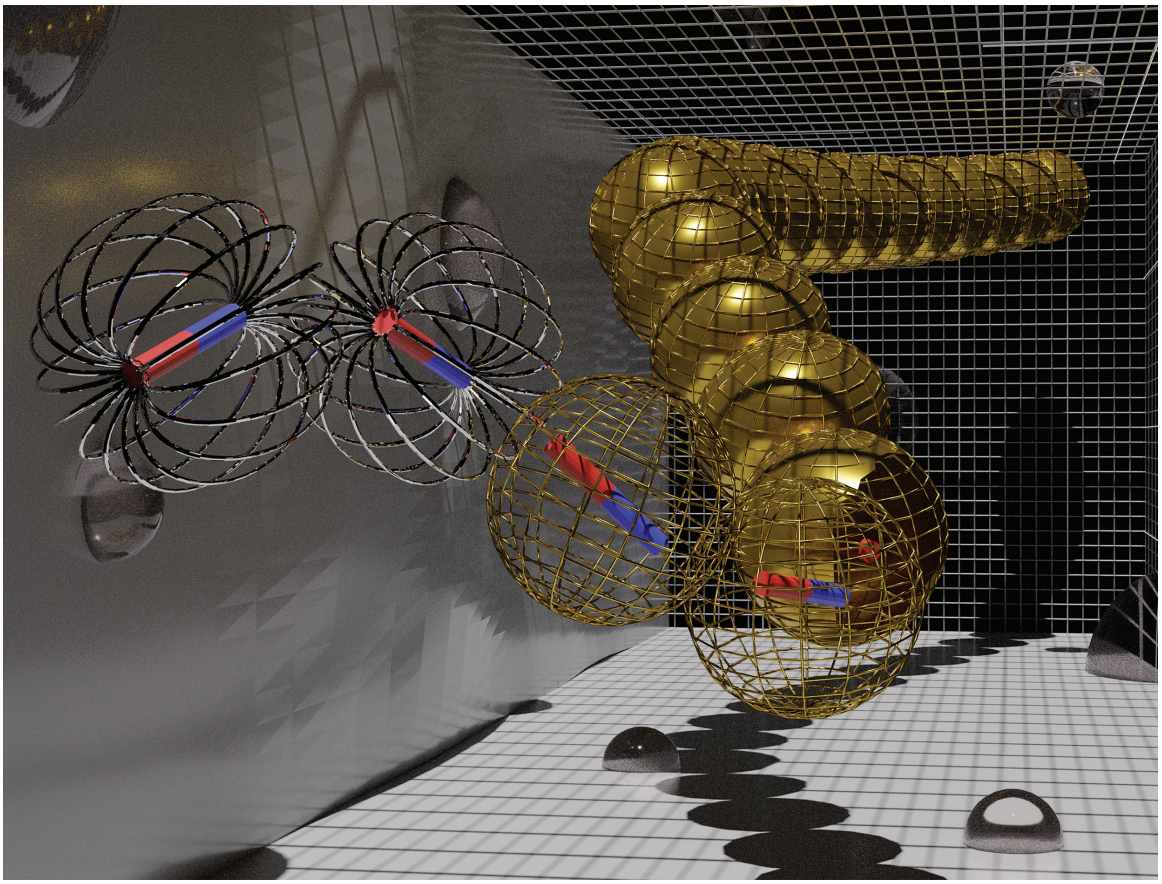

ISSN 2040-3372

ROYAL SOCIETY OF CHEMISTRY

PAPER
Deniz Mostarac *et al.*
Characterisation of the magnetic response of nanoscale magnetic filaments in applied fields

NCNST

NANO LETTERS

December 22, 2021
Volume 21, Number 24
pubs.acs.org/NanoLett

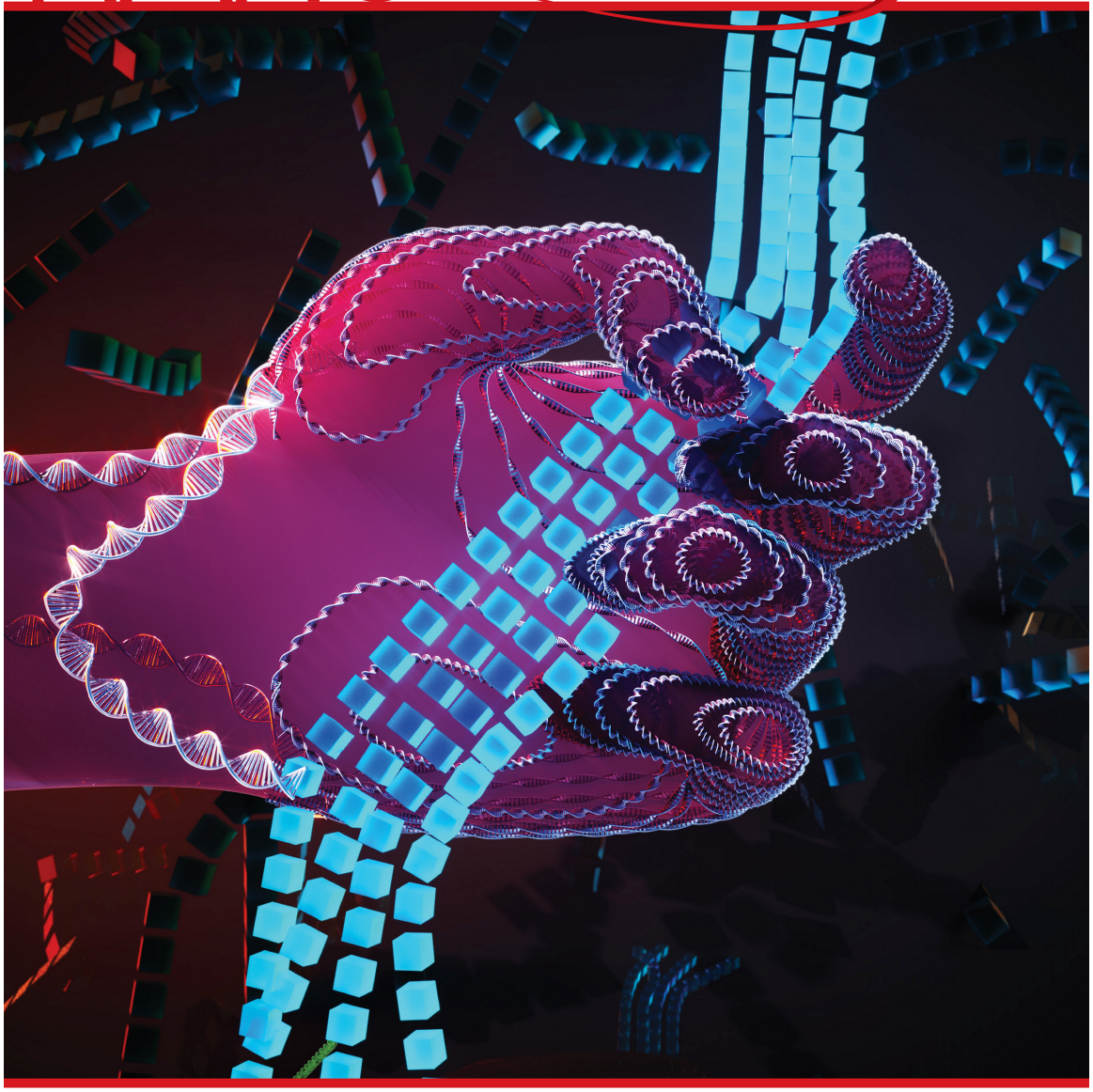

ACS Publications
Most Trusted. Most Cited. Most Read.

www.acs.org

It's just a ride.

— Bill Hicks

ACKNOWLEDGEMENTS

...and what a ride it was. I have to say that even though doing a PhD is indisputably difficult, on many levels the least of which is emotional, as I am writing this acknowledgements section, I am certain that submitting this thesis will not be the cathartic moment, the sense of achievement I was hoping it would be. Getting the degree was not the main challenge. The main challenge was and to some degree still is, to accept the fact that I am a "grown up". And every ounce of stress and relief, all the exciting and disappointing that this experience has brought me, was moving me along in life to a point where suddenly, there are stakes. I became invested in a narrative of my own making, moving along in a timeline, trying my darndest not to let it be the darkest one. Luckily, I have not been fighting alone. All the love, appreciation and support I have gotten along the way, looking back from where I'm sitting in my kitchen now, listening to the water sloshing in the dishwasher, made it a relatively smooth sailing. So, I suppose thanks are in order. I am first and foremost thankful that my supervisor, Prof. Sofia Kantorovich, would take a risk on me, and give me the opportunity to try something new, something I had no clue how to do beforehand, and that she would share unselfishly all the knowledge and experience she could. I am thankful for all the fancy food and drinks I was exposed to, that are a part of my life now, with a special mention for the blue cheese and walnuts on olive bread combo. I am thankful for my colleagues and collaborators, and the work environment we have established. I am thankful that I had someone to share my excitement whenever new GPUs were unveiled, and to venture into more philosophical discussions. I am thankful that I had someone to join me on my journey through the supernatural and the occult, and explore all the alternative personalities I could possibly invent, whenever I was avoiding doing that one thing, I really needed but hated to do. I am thankful for my friends that kept being in my life no matter what, kept insisting I should not be a hermit, kept organizing, pushing and supporting. I am thankful to my girlfriend, that would meet me in our home with excitement and love, give affection selflessly and provide endless entertainment. You truly did most of the heavy lifting, for every deadline, resubmission, revision and rejection. And most of the "kinji". Finally, I am thankful to my parents and family that gave everything they could and more, for a chance for me to get something of my own. This is for you.

CONTENTS

1 PROLOGUE

If one was trying to demarcate human history in epochs, predominantly used materials would be great markers. Books encompass the protohistory of humankind with the Stone, Bronze, and Iron age. In 1920, Staudinger proposed the macromolecular hypothesis,[165] by which he unequivocally defined what is a polymer. Namely, polymers (Greek: poly-, "many" + -mer, "part") are supramolecular chains, formed from a sequence of chemically identical units or sequences thereof, referred to as monomers. Polymeric, stimuli-responsive materials are one of the central research topics in modern soft mater physics,[7, 79] and are the focus of this thesis. Currently, available responsive materials are sensitive to a broad range of stimuli, like temperature, electromagnetic radiations,[87] pH,[38] ionic strength,[111] specific additives and substances,[181] and external fields.[147] M. Rubinstein proclaimed that the 20th century is the Polymer age, in his famous book on Polymer physics.[148] In the spirit of his proclamation, the 21st century could be called the Nanomaterial age.

Responsiveness to magnetic fields is of particular interest among the plethora of stimuli one can use to modify material properties in case it is advantageous to have dynamic intensity control and/or great spatial resolution. Furthermore, magnetic fields typically do not interfere with biological tissues and processes, which makes them useful for in-vivo stimulation of engineered materials.[174] The nonexistence of known polymer substances with pronounced magnetic properties, except for a few compounds at very low temperatures,[19, 90, 134] suggests the necessity of combining polymers with magnetic micro- or nanoparticles (MNPs).[171] Indeed, Staudinger's polymer definition reads quite naturally if one envisions MNPs as monomers, (chemical monomers in this context) while the crosslinkers establish the backbone of a polymer.

Polymer-like structures with MNPs, commonly referred to as magnetic filaments (MFs) are one of the soft matter systems that emerged in attempts to capitalize on the potential of magneto-responsive materials. The elegant simplicity of merging polymer-like systems and MNPs as a solution to the problem of magneto-responsive material design has naturally sparked a great deal of research. Magnetic nanoparticles in liquid carriers were first stabilized in the second half of the XX-th century and are named ferrofluids.[1] These colloidal dis-

1 Ferrofluids (ferrocolloids, magnetic fluids) are stable colloidal suspensions of single-domain particles of ferromagnetic or ferrimagnetic materials in liquid carriers.[143] The term ferrofluids was coined in Resler and Rosensweig [137]. The idea for ferrofluids initially came from NASA, as they were trying to create rocket fuel that

persions of magnetic iron oxides in hydrocarbon oil, represent probably the first application of magnetic materials in a novel form.[2] These magnetic systems have been studied theoretically and experimentally for more than 50 years.[74, 151, 184] Properties of magnetic fluids were shown to strongly depend on self-assembly of magnetic particles within them. In general, self-assembly has been recognized as a key mechanism for appropriating soft mater systems as building blocks for enhanced magnetic fluids and complex magneto-responsive structures. Numerous systems based on self-assembly have been studied, such as patchy colloids,[17, 131, 164] blunt-end DNA duplexes,[92, 117, 146, 210] and magneto-rheological suspensions.[126, 160] Self-assembled structures can further be stabilized and/or modified by introducing additional bonding mechanisms, such as crosslinkers, to the system. This allows the creation of supramolecular structures with specific properties, such as magnetic gels [58, 190, 219] and DNA origami structures.[125, 144, 209] Using crosslinked structures instead of sole nanoparticles has a tremendous impact on the thermodynamics and the microstructure of the bulk system. Interesting examples of realized crosslinked structures are dense arrays of non-permanent linear chains, adopting a transient polymer brush-like structure on a surface,[176] created via the field-induced assembly of polymer-coated magnetic particles, or polymer brushes embedded with MNPs directly.[36] The picture of polymer-MNP composite structures is clearly a compelling way to envision materials with a pronounced response to magnetic fields.

In recent years, chained, magnetic structures have found a growing range of applications.[187] Chain-like aggregates of MNPs have been shown as promising candidates for the design of recording media and sensor systems, biomedical materials and tunable photonic crystals.[187] Initial need for synthesis of chain-like aggregates of nanoparticles, arose for magnetically controlled microfluidic implementations. In particular, the main application of MFs explored to date, is their use as magnetically actuated artificial cilia, which can be used to create micro-swimmers.[10, 26, 47, 84] More generally, they are promising candidates to replace conventional magnetic fluids,[184, 195] in any application that may benefit from the enhancement of magneto-rheological responsiveness. Magnetic filaments can make the design of magnetically controlled micro-fluidic valves and micro-filter devices significantly simpler,[45] and might find use in magnetically controlled dampener designs or polishing systems.[126, 184, 195] Most existing crosslinking procedures for synthesis of composite materials are based on the functionalization of nanoparticle surface. Even though crosslinking through nanoparticle functional-

could be guided towards fuel pumps in a gravity-less environment using magnetic fields.

2 Their preparation was based on mechanical grinding of the bulk oxide in the presence of surfactant oleic acid and a hydrocarbon solvent.

ization has afforded much in terms of responsive magnetic material synthesis, it has proven an insurmountable obstacle, to create systems with a finely controllable microstructure. Furthermore, it has not been possible to utilize them in bio-compatible applications. Finding chemicals which will not dissociate in a polar solvent and remain bio-compatible is the main roadblock in application of any ferrofluid and more generally any material containing MNPs, for medical purposes.[85]

Theoretically, the properties of MFs exposed to external magnetic fields have mostly been explored in bulk.[9, 26–29, 52, 100, 158]. MFs with super-paramagnetic MNPs have been theoretically investigated in artificial swimmer designs.[62, 140, 141] In-field behavior (*i.e.* buckling, coiling and bending) of MFs with super-paramagnetic MNPs has been investigated under multiple conditions,[80, 215] such as having the MFs grafted to a surface,[192] or exposed to a rotating or fast precessing magnetic fields.[42, 99, 183]. MFs in general have proven very interesting as a basis for bio-medical application designs.[124, 129, 154] MFs with paramagnetic monomers have been investigated and characterized as potential micro-mixers,[18] as well as for cargo capture and transport purposes.[205]

Despite what the amount or research summarized here might suggest, it remains a matter of fact that flexible, nanoscale MFs, with a finely tunable microstructure, have not been synthesized yet. The key difficulty in such an endeavor is instilling selective, anisotropic interactions between nanoobjects that are otherwise entirely isotropic, with colloids that are chemically stable and when crosslinked, remain so permanently. Furthermore, despite the extremely broad spectrum of potential applications, research on MFs is still in an early stage, with huge gaps in understanding. Most of the aforementioned applications have barely been explored, if at all (both theoretically and experimentally). This thesis is a conglomeration of theoretical investigations aimed to provide a deep and comprehensive insight into fundamental properties of MFs and the phenomenology they exhibit.

1.1 THESIS OUTLINE

Results compiled in this thesis are presented in four, largely self-sufficient parts that broadly speaking, communicate how filament architecture, monomer properties, such as their magnetic nature and shape, are linked to the response of MFs to external magnetic fields. In the adjoining chapters comprising Part i of this thesis, a discussion of the principles and ideas that permeate through the topics covered, is presented. In general, however, the guiding principle adhered to in this work is to present concepts where first necessary. Therefore, each part of the thesis has its own, task specific exposition section. The rest of the thesis can be summarized as follows:

- **Part ii: Shaping the magnetic response of nanoscopic magnetic filaments**
  The second part of this thesis is a scrutinization of how microstructure and monomer properties relate to the structural and magnetic properties of MFs, at equilibrium. We encompass the effects of crosslinking and backbone stiffness in terms of inter-particle correlations. Together with the magnetic nature of monomers, we capture in a very general way how one can engineer equilibrium properties of MFs. Special attention is given to MF designs with super-paramagnetic monomers, where research was previously lacking. We develop a computation approach for super-paramagnetic MNPs that accounts for magnetization effects of dipolar fields, which are commonly neglected in literature. However, magnetization effects prove to be the key that unlock the door to exciting backbone bending phenomenology otherwise inaccessible. Furthermore, we investigate the effects of central attraction on the conformations of a single MF with super-paramagnetic monomers. In effect, by recognizing the key factors that determine magnetoresponsiveness of MFs, from fundamental theoretical investigations, we establish best practice guidelines for MF design, encompassing crosslinking, magnetic nature of monomers, microstructure, and effects of central attraction in a solution.

- **Part iii: Directional assembly of DNA nanocuboids as a platform for synthesis of MFs**
  Part iii of the thesis is focused on a specific, prospective design of MFs, that might in fact be the first instance of a synthesized MF that fulfills the criteria we underline and scrutinize throughout the thesis. Assembly of nanoscale objects into linear architectures is a basic organization resulting from divalent interactions. In particular, divalent cuboid DNA nanochambers (DNCs) can form nanopolymers and can be used as templates for targeted assembly of nanoparticles. [104, 201] We relate DNC nanoobject reactivity to polymerization and polymeric properties of the

resulting polymer-like morphologies. We underline that DNC-based nanopolymers represent a compelling, finely tunable platform for creating magneto-responsive materials. In effect, this part of the thesis establishes guidelines how to efficiently use DNCs to engineer MFs with desired properties.

- **Part iv: In-field Dynamics of MFs in Shear Flow**
  We present a study of the effects of the shape and magnetic nature of monomers on the behavior of MFs subjected to the simultaneous action of shear flow and a stationary external magnetic field perpendicular to the flow. We find that based on the magnetic nature of monomers, MFs exhibit completely different reorientational dynamics. While it was understood that non-equilibrium conformations and reorientation dynamics of polymer-like structures can be modified in a multitude of ways, here we not only elucidate that magnetic fields can be used to effectively control filaments in shear flow, but that their response can be architected with considerations of magnetic nature and shape of monomers.

In its entirety, this work envelops the phenomenology of a single MF in magnetic fields, both at equilibrium and in shear flow, and links it with corresponding design choices. With that we qualify the statement that MFs exhibit vastly different and systematically controllable behaviors. Depending on the use case, there are clear-cut advantages for filament designs based on crosslinking, the magnetic nature and shape of monomers. All of this is contextualized with a prospective filament design, based on a novel, experimentally realized, and theoretically well understood system.

Part I

FOUNDATIONS

In this part, a discussion of ideas, concepts, and techniques that form the foundations on which this work stands and builds upon, is presented. In effect, this part is the exposition of topics common to all the parts of the thesis, necessary for the digestion of the results. Key aspects that contextualize this research and form the bedrock of the investigation can broadly be enveloped by: Molecular dynamics simulations, Polymer physics and Magnetism, all from the point of view of nanotechnology and nanoparticles. The discussion is, however, not meant to be exhaustive, as a comprehensive overview of either of the aforementioned topics would require us to venture far beyond the intended scope. Therefore, conscious effort is made to keep the "world building" aspect this work short and to the point, covering only the most salient aspects.[3]

3 The author reserves the right to indulge in some sidequests along the way.

2

MOLECULAR DYNAMICS

Molecular dynamics (MD) is a deterministic computer simulation technique used to study the dynamics of classical many-body systems. The basic idea of MD is simple and somewhat parallel to what would happen in an experimental setting (in the laboratory or in nature). An outline of the basic idea could go as follows:

- In a lab, one would firstly engage in sample preparation. For MD simulations this typically means initializing a system in equilibrium. However, depending on the investigation, one can specify a system with any set of positions and momenta.
- Investigations of sample properties would be performed using a measuring device over a time. Longer measurements decrease statistical errors. In MD simulations, we propagate the system in small timesteps, by solving Newtons equations of motion. While the system evolves in time, we measure some property.
- Statistically relevant and representative results are obtained as averages of multiple, separate measurements.

MD simulations with velocity rescaling thermostats can be thought of as Monte Carlo simulations with MD moves and velocity rescaling moves.

First MD simulations were carried out by Alder and Wainwright in 1956 to investigate whether a hard sphere system undergoes a (purely entropic) first order transition from the fluid phase to a crystalline phase.[5] Confirming that this is in fact the case was one of the first major successes of computer simulations.

2.1 THE BASIC STRUCTURE OF AN MD SCHEME

MD simulations follow the natural time evolution of a system, and as such can be applied to study not only systems in equilibrium but also system out of equilibrium, and their dynamics. Consider a system of N point particles with a mass m_i. Interactions between the particles are expressed through the potential energy $U(\vec{r}^N)$, where $\vec{r}^N$ is the lab frame Cartesian coordinates vector. The total energy of the system is given by the Hamilton function:

$$H(\vec{r}^N, \vec{p}^N) = \sum_i^N \frac{\vec{p}_i^2}{2m_i} + U(\vec{r}^N), \tag{2.1}$$

with the Hamilton equations of motion given by:

$$\frac{\partial \vec{r}_i}{\partial t} = \frac{\vec{p}_i}{m_i}; \quad \frac{\partial \vec{p}_i}{\partial t} = -\nabla_i U(\vec{r}^N) = \vec{F}_i. \tag{2.2}$$

This is a set of 6N coupled ordinary first order differential equations, that are deterministic and reversible. Solving these equations of motion (given initial conditions) yields particle trajectories, where the positions and momenta of the particles are specified as functions of time. MD simulations therefore inherit the conservation laws from Hamiltonian dynamics. A time-independent Hamiltonian implies strict total energy conservation. Translationally invariant potential energy implies total (linear) momentum conservation. In principle, for an isolated system the total angular momentum is also conserved by Hamiltonian dynamic. Hamilton's equations of motion also conserve phase space volume.

In general, solving the Hamiltonian equations analytically is challenging and usually not possible except for simple and/or small systems (*i.e.*, free particle or for a harmonic oscillator). Equations of motion are commonly solved numerically in small, discrete timesteps. This is exactly the idea behind MD simulations. MD simulations in this work have been performed in the NVT ensemble at a constant temperature. We specify the scheme below.

2.2 LANGEVIN THERMOSTAT AND THE INTEGRATION SCHEME

Molecular dynamics schemes for carrying out simulations at constant temperature are called thermostats. A few examples where such schemes are useful would be sampling the canonical ensemble at equilibrium or removing dissipated energy in a non-equilibrium system driven by an external perturbation. For instance, one would need to do so for a liquid between sheared plates or dipole moments in an external magnetic field. Without a suitable thermostat, the energy would increase indefinitely precluding the possibility of every reaching a non-equilibrium steady state. The central quantity that connects the microscopic and the macroscopic world is the canonical partition function Q_{NVT}:

$$Q_{NVT} = \frac{1}{N!(2\pi\hbar)^{3N}} \int d\vec{r}^N d\vec{p}^N e^{-\frac{H(\vec{r}^N, \vec{p}^N)}{k_b T}}. \tag{2.3}$$

Analysis on the level of statistical mechanics is related to thermodynamics through the relation between Q_{NVT} and thermodynamic potentials, namely:

$$\mathcal{F}(N, V, T) = -k_b T \ln Q_{NVT} = E - TS, \tag{2.4}$$

where $\mathcal{F}(N, V, T)$ is the free energy and S is entropy. Thermodynamic inner energy E is equal to the expectation value of the Hamilton function in the canonical ensemble. The probability of observing a particular microstate in the canonical ensemble is proportional to the Boltzmann factor $exp(-H(\vec{r}^N, \vec{p}^N)/k_b T)$. The ratio of the probability of

observing a particular microstate and Q_{NVT} therefore makes a probability density function. In the canonical ensemble, it is important to keep in mind the instantaneous temperature T_k, is a fluctuating quantity, and only on average corresponds to the temperature T of the thermostat.[1] In fact, the probability distribution of T_k in the canonical ensemble can in general be given with:

$$P(T_k) = \frac{1}{T}\frac{3N/2}{\Gamma(3N/2)}\left(\frac{3NT_k}{2T}\right)^{3N/2-1} e^{3NT_k/2T}. \tag{2.5}$$

There are many thermostats that can produce a canonical ensemble for a given temperature such as the Anderson, Nosé-Hoover, and Bearsden thermostats.[75] In principle, they are based on propagating Newtons equation of motion with velocity rescaling in regular intervals, to fit an appropriate distribution. However, for equilibrium properties simulations, we use a thermostat based on an extension of Newtons equation of motion, namely the Langevin equations, which are very computationally efficient and reliable.[66] The Langevin equations are stochastic differential equations which describe the evolution of a system coupled to fast degrees of freedom, implicitly reflected by random forces. A typical example would be colloids immersed in a liquid, where the colloid has a much larger mass compared to the solvent. The Langevin equations description applies at times much greater than the characteristic collision time of the system. Therefore, we assume that the solvent molecules exert random forces (Brownian motion). The Langevin equations are given by:

$$M_i \frac{d\vec{v}_i}{dt} = \vec{F}_i - \Gamma_{Tl}\vec{v}_i + 2\vec{\xi}_i^{Tl} \tag{2.6}$$

$$I_i \frac{d\vec{\omega}_i}{dt} = \vec{\tau}_i - \Gamma_R\vec{\omega}_i + 2\vec{\xi}_i^{R}, \tag{2.7}$$

where for the i-th particle in Eq. (2.6), M_i is the mass tensor, $\vec{v}_i$ denotes the translational velocity, $\vec{F}_i$ is the force acting on it, Γ_{Tl} denotes the translational friction coefficient, $\vec{\xi}_i^{Tl}$ is a stochastic force modelling the random forces of the implicit solvent. In Eq. (2.7), I_i denotes i-th particle inertia tensor, $\vec{\omega}_i$ is its rotational velocity, $\vec{\tau}_i$ is torque acting on it, Γ_R denotes the rotational friction coefficient, and the $\vec{\xi}_i^{R}$ is a stochastic torque serving for the same purpose as $\vec{\xi}_i^{Tl}$. The friction terms account for dissipation in a surrounding fluid whereas the random force mimics collisions of the particles with solvent molecules at a fixed temperature. Both stochastic terms satisfy the following conditions on their time averages [180]:

$$\langle\vec{\xi}^{R/Tl}\rangle_t = 0 \tag{2.8}$$

$$\langle\vec{\xi}_l^{Tl/R}(t)\vec{\xi}_k^{Tl/R}(t')\rangle = 2\Gamma_{Tl/R}k_BT\delta_{l,k}\delta(t-t'), \tag{2.9}$$

1 In fact, the magnitude of the instantaneous temperature fluctuates as $1/\sqrt{N}$ with a relative variance $\sigma^2_{T_k} = 2T^2/3N$, as expected for a quantity that represents a sum of many independent contributions.

where $k, l = x, y, z$.

Forces and torques in Eq. (2.6) and (2.7) are calculated from inter-particle interaction potentials. In absence of friction and random forces Eq. (2.6) and (2.7) reduce to Newtons equation of motion. Since the fast degrees of freedom are implicitly taken as stochastic terms inside the Langevin thermostat, we can choose relatively large timesteps. Trajectories of point like particles are described by the equations of motion:

$$\frac{\partial \vec{v}_i(t)}{\partial t} = \frac{\vec{F}_i(\{\vec{r}_j\}, \vec{v}_i, t)}{m_i} \tag{2.10}$$

$$\frac{\partial \vec{r}_i(t)}{\partial t} = \vec{v}_i(t). \tag{2.11}$$

In practice, Langevin equations of motion are discretized and integrated over time t numerically in Δt increments, usually and preferably using the Velocity Verlet algorithm.[135]. Numerical integration of Eq. (2.10) and (2.11) discretized using the Velocity Verlet algorithm transpires in the following steps:

- Calculate the particle velocity at the half of the time interval $\Delta t/2$

$$\vec{v}_i(t + \Delta t/2) = \vec{v}_i(t) + \frac{\vec{F}_i(\{\vec{r}_j(t)\}, \vec{v}_i(t - \Delta t/2), t)}{m_i} \Delta t/2 \tag{2.12}$$

- Determine particle position propagated by the time interval Δt

$$\vec{r}_i(t + \Delta t) = \vec{r}_i(t) + \vec{v}_i(t + \Delta t/2)\Delta t \tag{2.13}$$

- Determine the total force acting on the particle at the new position

$$\vec{F}_i = \vec{F}_i(\{\vec{r}_j(t + \Delta t)\}, \vec{v}_i(t + \Delta t/2), t + \Delta t) \tag{2.14}$$

- Calculate velocity based on new forces at position $x(t + \Delta t)$

$$\vec{v}_i(t + \Delta t) = \vec{v}_i(t + \Delta t/2) + \frac{\vec{F}_i}{m_i} \Delta t/2 \tag{2.15}$$

The Velocity Verlet algorithm is a self-starting algorithm, that keeps our simulations fully time-reversible and phase volume conserving. This implies energy conservation. The global error associated with the Verlet algorithm is third order for the position and second order for the velocity.

2.3 TECHNICAL AND IMPLEMENTATION NOTES

This thesis is a collection of theoretical investigations on polymer-like systems with MNPs, using MD simulations. The goal is, however, to gain insight into the fundamental physics behind the phenomenology. What makes that, what can operationally be describes as computational modelling, into fundamental research? The answer lies in, what is commonly referred to as coarse graining. One systematically re-envisages and reformulates the problem at hand into a distilled representation that consists of only the fundamental, necessarily elements. In the context of this work, this means that by using coarse grained computational models, we pinpoint the basic principles and interactions that govern the phenomenology at hand, and therefore uncover at the fundamental level how their interplay reverberates back into reality. All the simulation work presented in this thesis were done using the ESPResSo simulation package.[193] What ESPResSo is, is well described by a quote from the documentation:

> ESPResSo *is a simulation package designed to perform Molecular dynamics (*MD*) and Monte Carlo (MC) simulations. It is meant to be a universal tool for simulations of a variety of soft matter systems. It features a broad range of interaction potentials which opens possibilities for performing simulations using models with different levels of coarse graining. It also includes modern and efficient algorithms for treatment of electrostatics (P3M, MMM-type algorithms, constant potential simulations, dielectric interfaces, . . .), hydrodynamic interactions (Dissipative Particle Dynamics, Lattice-Boltzmann), and Magnetostatics / Dipolar interactions, only to name a few. It is designed to exploit the capabilities of parallel computational environments. The program is being continuously extended to keep the pace with current developments both in the algorithms and software. The kernel of* ESPResSo *is written in* C++ *with computational efficiency in mind. Interaction between the user and the simulation engine is provided via a Python scripting interface. This enables setup of arbitrarily complex systems, with simulation parameters that can be modified at runtime.*

Simulations performed in the scope of this thesis, while mostly concerned with the properties of a single filament (with the notable exception of the content discussed in Chapter 11) have also explored environments (simulation box and constraints) of varying shape, dimensionality, and periodicity. Unless otherwise noted, the default space configuration in this thesis is a 3D, non-periodic simulation box with a side length corresponding to 25 times the characteristic length scale of the system we are simulating.

It is worthwhile to justify Langevin dynamics as the principal tool used for much of the work presented in this thesis. While certainly

not the only appropriate method, it is the pragmatic choice. As opposed to the Berendsen thermostat, for example, where it is necessary to sum up the kinetic energies over the whole system, Langevin thermostat is purely local. This means that computationally, calculations can be done in parallel (excluding long range interactions) on the level of the cell domain decomposition. Furthermore, Langevin thermostat is much more efficient and stable in thermalizing dilute systems. For example, the Anderson thermostat randomly reassign the velocities of a selection of particles, drawing from a Maxwell-Boltzmann distribution with the desired temperature. This leads to sudden and random decorrelations of particle velocities. Therefore, it is very complicated to be used correctly if one is interested in dynamical quantities.[2] A well-documented artifact of algorithms used in MD simulations, known as the "flying ice cube effect", manifests in simulations of particles in vacuum, where the simulated system acquires high linear momentum with overdamped internal dynamics, freezing the system into a conformation reminiscent of an ice cube flying through space. Essentially, the energy of high-frequency fundamental modes is absorbed into low-frequency modes, particularly into zero-frequency motions such as overall translation and rotation of the system. In general, schemes such as the Berendsen thermostat, fail when the rescaling is done with respect to a kinetic energy distribution of an ensemble that is not invariant under microcanonical MD.

A system can be treated as having periodic or non-periodic boundaries. Periodic boundary conditions (PBC) allow simulations to mimic the conditions present in bulk.

There are several technical optimizations that we relied on heavily. They are outlined in no particular order bellow. We use cell domain decomposition based using Verlet lists for interaction calculations.[3] With a Langevin thermostat, this means that the order of pair interactions is $O(N)$, excluding long range interactions. Although there are highly efficient algorithms for calculation of long-range magnetostatic interactions such as the P3M method,[31], the system we simulate cannot benefit from them. We calculate energies and forces between dipoles by explicitly summing over all pairs, which adds the bulk of computational cost (order of pair interactions $O(N^2)$) in our simulations. For the directions in which the simulation box is periodic, we use the minimum image convention, *i.e.*, the interaction is effectively cut off at half the image box length. We rely heavily on the concept of virtual sites.[193] A virtual site is fixed with respect to the reference frame of the "real" particle to which it is attributed. The interactions between virtual-virtual and virtual-real particles can be specified using any suitable potential. All forces exerted on the virtual sites because of such interactions are instantaneously propagated to

2 It is necessary to select the collision rate appropriately.

3 Verlet list is a data structure in MD simulations that contains sets of interaction partners for each particle within a cut-off distance. Short-range interactions pair interactions can be considered negligible after the cut-off distance. Usually, Verlet lists are supplemented by a buffer that allows for some overlap between cells.

the reference, real particle, at each timestep. This feature allows us to make rigid bodies with any shape by defining proper arrangements of virtual sites. This will be further elaborated for each application and implementation.

Finally, it is worth noting, while ESPResSo, as a toolbox for computational investigation of soft matter is very comprehensive and robust, the results in this work are heavily reliant on custom tools and code that is not part of the ESPResSo codebase. Regardless, ESPResSo has a very accommodating way to implement custom tools directly into it without having to interfere with the core or risk of breaking core functionality, by using a Cython mediator layer for example.

2.4 ABOUT UNITS

Length scale choice when simulating hydrodynamic interactions are restricted based on algorithm implementation. This is discussed at length in Part iv.

Throughout this work, we extensively use reduced units. This highlights the fact that the results presented in this work, are, just like law of corresponding states, representative for many states with different units. What is probably one of the most confusing subjects for the uninitiated, the freedom afforded by not predefining any units, facilitates a relative way of thinking about scales. As longs as ratios are maintained, the system can be arbitrarily rescaled. In any case, physically, absolute values are meaningless if not relative to something else. Reduced unit system is the embodiment of this paradigm.

The length, time and energy scales can be freely chosen. Once these scales are fixed, all remaining units are derived from them. Length scale in our simulations is chosen in relation to monomer size, because the phenomenology we are interested in is on the level of the overall polymeric structure.[4] Apart from freely choosing the length scale, one needs to choose the energy scale. Temperature is coupled to the energy scale by the Boltzmann constant. Temperature scaling is outside the scope of this thesis. Therefore, by choosing room temperature as the standard choice, one specifies the energies of all the other interactions in units of thermal energy. Scaling interaction energy with respect to the strength of thermal fluctuations is a very intuitive and generalizable way to scale parameters.

The final choice to make is either the time or mass scale. For investigations of properties at equilibrium, mass is irrelevant, as it is completely absent from the partition function.[5] Therefore, it is sensible to derive the mass based on the time scale. When extracting equilibrium properties, one implicitly assumes that the duration of simulation is long enough that we have sampled the phase space sufficiently to make conclusion about the equilibrium. Therefore, time

4 Internal particle dynamics do not propagate with the equations of motion and are therefore external to the MD scheme.

5 Investigation of dynamics, where mass is crucial, is tackled in the Introduction of Part iv.

scale should be chosen as large as possible. Of course, it should not be so high that one would not be able to resolve the eigenfrequencies of the processes we are looking to capture. Furthermore, sampling frequency, while not entirely a physical consideration, should be chosen in conjunction with the time scale, because it should be smaller than the eigenfrequencies we are trying to resolve but large enough to sample statistically independent microstates. By default, ESPResSo uses a reduced mass of 1 for all particles, so that the mass unit is simply the mass of one particle. Combined with the energy and length scale, this is sufficient to derive the resulting time scale:

$$[\mathrm{time}] = [\mathrm{length}]\sqrt{\frac{[\mathrm{mass}]}{[\mathrm{energy}]}}. \tag{2.16}$$

Actual values of reduced units we use are discussed for each part of the thesis separately, together with conversions to SI units.

3

POLYMERS

In this chapter, an overview of basic concepts in polymer physics is presented. We begin with a quote from the inspiring book Piazza [130], that skillfully and eloquently envelops just how much polymers permeate our lives:

> *Packaging, bags, and food containers. Synthetic fibers, sunglasses, and pantyhose. Furniture, mattresses, and tubing. Videotapes, records, and DVDs. Glues, sealants, and varnishes. Switches, electric cables, and optical fibers. Car tires, bumpers, and dashboard. Keyboard, mouse, and screen of the computer I am using... And so on and so forth. From children's toys to space probes, the world as we see it today could not exist without the essential contribution of what we call plastic materials.*

Polymers are the common motif for all abovementioned things. Although the chemical properties are set by the specific chemical nature of the monomers, most of the physical properties that make polymers so different from simple molecules are very general, and stem from their being long and flexible macromolecules. Let us qualify this statement.

3.1 LENGTH AND TIME SCALE

The most common catalysts consist of titanium(III) chloride, the so-called Ziegler-Natta catalysts. Another common catalyst is the Phillips catalyst, prepared by depositing chromium (VI) oxide on silica.[50]

Consider the simplest polymer known and coincidentally the most widely used one today, polyethylene. Monomers that make out the polymer in this case are instances of hydrocarbon ethylene (C_2H_4). When catalyzed, the double bond between the carbon atoms (C) in ethylene can be broken to essentially form a double methylene sequence ($-CH_2-CH_2-$) where each methylene has a free bond. Therefore, polyethylene is denoted as $(-CH_2-CH_2-)_n$. The angle between consecutive carbon atoms is well-defined, and as such for every triplet of carbon atoms the relative orientation can be described by a fixed angle. However, between every triplet there is an additional degree of freedom,[1] as C triplets can be rotated with respect to each other. In fact, there is a discrete set of possibilities of the relative orientation between C triplets, corresponding to the energy minima in the potential energy. [2]

1 The main source of flexibility in polyethylene is the variation in the so-called torsion angle.

2 The potential energy depends on the angle between successive C triplets. There are three energy minima due to excluded volume interactions, corresponding to three

Let us consider a closed system where the only source of energy is thermal fluctuations. If the thermal energy k_bT is comparable to the energy difference between discrete configurations of polyethylene $\Delta\epsilon$, for a long chain, on average we would have a coiled-up polymer. In other words, when $\Delta\epsilon/k_bT < 1$, we are in the flexible polymer regime. As we increase the ratio $\Delta\epsilon/k_bT$ however, conformations will tend to form based on the global minimum, and as such become more rigid. It is important to understand that rigidity can be recast in terms of the length scale of a problem. Regardless of the value of the $\Delta\epsilon/k_bT$, a sufficiently long chain will be coiled up. Energy scale and its energy ratios essentially determine what is the length scale at which a polymer is flexible. Using the nomenclature used in De Gennes [40] we denote this the length scale of static flexibility of a polymer. Rigidity can also be understood in terms of time scale. The ratio between the energy barrier between the discrete conformational states ΔE and k_bT, gives us the time it takes to transition between them. Energy scale and its energy ratios determine what is the time scale at which a polymer is flexible. Again, using the nomenclature used in De Gennes [40] we denote this the time scale of dynamic flexibility of a polymer. In this thesis, we are interested exclusively in the static flexibility length scale and dynamic flexibility time scale of polymer-like objects. In other words, we are interested in local properties: conformations and motions inside the chain, and their dependence on monomer properties and polymer microstructure. Therein also lies the genesis of soft matter, and plastic industry for that matter. Controlling the microstructure of polyethylene determines the rigidity of the resulting material. We needed to introduce very little to underline this simple concept, a tip of the iceberg of the potential that has since proliferated under the umbrella of soft mater physics.

We can constrain out interest further. As previously stated, while chemical properties of monomers are locally relevant, on the scales of flexible chains, they are largely irrelevant, and fall under the umbrella of very general scaling laws. In the same sense, magnetic monomers in polymer-like conformation behave largely like typical polymers. The twist is that one can use external magnetic fields to leverage the magnetic nature of individual monomers and generate an overall magnetic response of the filament. Therefore, a MF as a representative member of highly magneto-responsive, smart micro- and nanomaterials, is a compelling system only as far as it has a flexible backbone and a highly tunable micro- and nanostructure.

principal conformations called trans (0°) and gauche (120°&−120°). Trans configuration is preferable because it has a lower energy.

3.2 IDEAL POLYMERS

Let us introduce some mathematical rigor to the intuitive notion of what a polymer is. We follow the approach of a pragmatic physicist that, as is known in contemporary culture, starts modelling the production of milk on a farm with a spherical cow in vacuum. Consider a mesh grid of equally spaced nodes. A random walk on a grid constitutes that each step is a move in a random direction, only one node at a time, a distance we denote as a. A random walk starting at node x_i and reaching node x_f after N steps, outlines a conformation of an ideal polymer with N monomers. The entropy of an ideal polymer increases proportionally to $\Omega(x_i \to x_f) = \sum_N \Omega(a) = n_a^N$, where n_a is the number of nearest neighbors each node has. On the other hand, for a N step random walk, along every grid dimension, the number of possible ways to have reached x_f is the coefficient of the binomial distribution $W(N, x_f)$. The probability to be at x_f after N steps is therefore given by $p(N, x_f) = W(N, x_f)/n_a^N$, which in the limit of $x_f << N$, can be approximated to a Gaussian distribution. It can be shown that the total length of a random walk is given by $< R_{ee}^2 >= N \cdot a^2$, or in other words end-to-end distance of an ideal polymer is proportional to the square of the steps.[3]

The distance between carbon atoms in an ethylene molecule is almost constant $d = 1.54 \cdot 10^{-10} m \pm 0.03\%$. *A C atom triplet forms a torsion angle of* $68°$.

The statement that individual steps are completely uncorrelated from each other, is equivalent to saying that monomers in an ideal polymer do not interact with each other. However, in the case of polyethylene for example, we know that a triplet of C atoms enclose an essentially fixed angle. Consequently, one should consider that monomers in an ideal polymer are not entirely uncorrelated. In fact, we take that correlations between steps of a random walk decay for every l_{corr} steps. R_{ee} of a random walk with a correlation length l_{corr} still respects $\propto \sqrt{N}$ scaling if we "zoom out" and consider every l_{corr} segment as a single uncorrelated step. If we understand each uncorrelated step of a random walk to correspond to a monomer in the conformation of an ideal polymer, we reformulated the length and time scale argumentation from the section above. In this case, a monomer corresponds to what is commonly called a Kuhn segment. One can always get a random walk if one takes enough Kuhn segment steps, which is also why such a simplistic treatment of a polymer is always useful.

So far, we have established that an ideal polymer obeys Gaussian statistics and that its end-to-end distance increases as the square of the number of monomers. The probability of finding a monomer of

3 The ensemble average of the end-to-end vector is $< \vec{R}_{ee} >= 0$ for an ideal polymer. When we talk about R_{ee} it is implied that we are talking about the root-mean-square end-to-end distance. With the assumption of constant step and Gaussian statistics, $R_{ee} \propto \sqrt{N} a$, where a is the uncorrelated step size end N is the length of a random walk. The proportionality involves the Flory characteristic ratio factor C which is asymptotically constant with length of walk.

an ideal polymer in a spherical volume with radius r around another monomer along the backbone, is expressed by the so-called pair-correlation function $g(r)$ and is given by:

$$g(r) = \frac{1}{\rho^2} \sum_{i,j \neq i} \delta(r - r_{ij}). \tag{3.1}$$

Integrating the pair-correlation function over all pairs and monomers must give the number of monomers. The Fourier transform of the pair-correlation function, called the Debye function, therefore respects that $\int g(r) e^{iqr} dr|^{q=0} = N$. The pair-correlation function scales like the number density of monomers in a sphere of radius r, where for a random walk with a Kuhn segment a, the Debye function becomes $g_D(r) \propto (a^2 r)^{-1}$, as long as the radius of the sphere is smaller than the size of our ideal polymer. In other words, it is likely to find monomers of an ideal polymer close together, in a coiled conformation.

Furthermore, if we look at the free energy of a 3D random walk, given by

$$\mathcal{F}(\vec{R}_{ee}) = \mathcal{F}(0) + \frac{3 k_b T \vec{R}_{ee}^2}{2 < R_{ee}^2 >}, \tag{3.2}$$

where $\mathcal{F}(0)$ is the free energy of a polymer with both ends at the same point and $\vec{R}_{ee}$ is the vector pointing from x_i to x_f, one can see that ideal polymers maximize entropy for a walk where x_i and x_f are at the same point. This outlines the characteristic trend of flexible polymers to coil up. Furthermore, the free energy of a free chain increases quadratically with R_{ee}. In other words, entropic elasticity of an ideal polymer can be described using Hooks law.[40]

In general, the pair-correlation function $g(r) \propto R^{D_H - 3}$.

This brings us to a discussion of dimensionality. We naturally think of crystalline lattices as 3D structures. From this point of view polymers are 1D objects. However, it is more appropriate to have this discussion in terms of the Hausdorff fractional dimensions D_H.[4] For a suspension of homogeneously distributed monomers, the number of monomers in a spherical volume grows as the third power of its radius. In other words, the fractal dimension of a homogeneous suspension of monomers is $D_H = 3$. If we take a spherical volume with a radius corresponding to the R_{ee} of a random walk, we know that the radius of this volume is proportional to the square root of the number of steps. Therefore, using the Hausdorff fractal dimension interpretation, ideal polymers have $D_H = 2$ Ideal polymers are 2D fractals. With this, we have outlined the definition of an ideal polymer in terms of scaling laws.

4 A fractal is an object that is self-similar, *i.e.*, a geometric shape reducible to smaller reduced copies of itself. We can calculate fractal dimension $D_H = \lim_{l \to 0} \frac{\log N(l)}{\log (1/l)}$, where $N(l)$ is the number of self-similar structures of linear size l required to cover the original object.

3.3 FLORY FREE ENERGY OF A REAL CHAIN

In Section 3.2, we outlined an idealized representation of a polymer that is only governed by entropy. Ideal polymers have non-interacting monomers, in analogy to non-correlated random walk steps. The most significant omission from the ideal polymer model is that no two monomers can occupy the same volume at the same time. Each monomer excludes volume and renders it inaccessible. If the simplifying assumptions of the ideal polymer model are given up, *i.e.*, if interactions between the monomers and excluded volume effects are allowed for, many-particle systems become much more difficult to represent. However, one can use the ideal polymer model as a reference system and use a type of perturbation theory around the ideal representation to get an approximation of a more realistic polymer. This chapters content is well within the range of applicability of such perturbation theories, which means that the monomer number density is low and inter-monomer interactions are weak. Given that we are interested in single polymer properties, this is a condition that is fulfilled trivially. Furthermore, we are going to always assume a good solvent, in which excluded volume interactions are small.[5] In other words, excluded volume interactions in this model are exclusively pair interactions. Here, we present the simplest real polymer model called a self-avoiding walk (*SAW*), that while flawed, has surprisingly wide applicability.

Consider an ideal polymer in a D-dimensional space. The excluded volume fraction of a polymer in a spherical volume of radius $R = a\sqrt{N}$ is defined as: $\Phi = a^D N/R^D$, where a is the Kuhn segment. The probability of any two monomers overlapping is proportional to Φ. The number or monomer-contacts is proportional to $N\Phi$. It can be seen that, as is also true for ideal polymers, if $2 \leqslant D \leqslant 4$, the probability of overlap is very small, but the number of monomer-contacts is large.

To understand the contribution of excluded volume interaction to the free energy in a general way, one only needs the assumption that the system is closed, and that the canonical coordinates $\vec{p}$ and $\vec{q}$ in a Hamiltonian $H(\vec{p}, \vec{q}, t)$ are therefore finite. The Virial of $H(\vec{p}, \vec{q}, t)$ is defined as $G = \sum_i^N \vec{p}_i \vec{q}_i$. Using the Hamilton equations, we know that:

$$\frac{\partial G}{\partial t} \propto \kappa(\vec{p}) + \sum_i^N \vec{q}_i (\partial_{\vec{q}_i} U(\vec{q}) + f_{ext}(\vec{q}_i)), \tag{3.3}$$

5 Throughout this work, unless central attraction is explicitly included, monomers make no energetic distinction between other monomers and solvent, which could correspond to an athermal fluid in high T limit. We are not interested in the high T limit, but interaction energy scales where the interactions are competitive. Therefore, it is implicit that polymers and filaments in this work are in a good solvent but are chemically stabilized.

where $\kappa(\vec{p})$ is the kinetic energy, $U(\vec{q})$ is the total potential energy, and $f_{ext}(\vec{q}_i)$ encompasses external forces acting on the system. We assume that $U(\vec{q})$ can be represented as a sum of exclusively pair interactions $U(\vec{q}) = \sum_{k=1}^{N} \sum_{j=1,j\neq k}^{N} U_{pair}(\vec{q}_k, \vec{q}_j)$. For an ideal gas in a closed container with volume V, molecular theory and the equipartition theorem state that, from Eq. (3.3), one can obtain an equation of state for pressure as a function of temperature T and density ρ, $P(T, \rho)$, in the following form:

$$P(T, \rho) \propto \rho k_b T - < \frac{1}{3V} \sum_{i}^{N} \vec{q}_i \partial_{\vec{q}_i} U(\vec{q}) > . \tag{3.4}$$

Equation (3.4) is an equation of state of an ideal gas with a correction, called the Virial correction, that accounts for the inter-particle interactions governed by the potential $U(\vec{q})$. In general, the Virial correction can be written using the pair correction function $g(r)$ given in Eq. (3.1).

The potential energy cost to bring two monomers from infinity to a distance r from each other is proportional to the Boltzmann factor. Furthermore, if the interaction potential is radially symmetric, under the assumption that the pair-correction function is a Boltzmann distribution of the interaction potential, one can reach the definition of excluded volume ν corresponding to the second order virial expansion coefficient:

$$\nu = \int \left(1 - \exp \frac{-U(r)}{k_b T}\right) d^3 r. \tag{3.5}$$

For example, if the excluded volume is governed by the hard sphere interaction potential, excluded volume $\nu \approx a^3$, where a is monomer size. In MD simulations however, the hard sphere potential is usually replaced a continuous, soft-core interaction because of numerical stability.

Interactions between monomers are restricted to excluded volume interactions is a *SAW* and the contribution of interacting monomers to the free energy is proportional to the probability of monomer pairs overlapping and the total number of monomers. Therefore, for a polymer with the size r_f, the free energy correction can be written as $\mathcal{F}_{int} \approx k_b T \nu N^2 / r_f^3$. Together with the purely entropic contributions we outlined for ideal polymers, the Flory theory free energy of a real polymer with length r_f, is given:

$$\mathcal{F} \approx k_b T \left(\frac{\nu N^2}{r_f^3} + \frac{r_f^2}{< R_{ee}^2 >} \right). \tag{3.6}$$

Real polymers are swollen compared to their ideal counterparts. The energy minimum of Flory free energy dictates that, while for an ideal polymer $R_{ee} \propto \sqrt{N}$, real polymers have $R_{ee} \propto N^{3/5}$. So real polymers are fractal objects with $D_H = 5/3$. The pair-correlation function

for real polymers must be modified to account for the fact that the monomers contained in a spherical volume or radius r have excluded volume and their number is, therefore, proportional to $n \propto (r/a)^{5/3}$, where a is the diameter of the excluded volume of a hard sphere monomer. As long the radius of the spherical volume is smaller than the polymer size, $g_D(r) \propto r^{-4/3}a^{-5/3}$. A *SAW* under tension does not satisfy Hooks law. Chain elongation is proportional to force with an exponent equal to 3/2. Finally, *SAW* does not obey Gaussian statistics, because excluded volume interactions are repulsive. This reduces the probability for two monomers to be near each other. The probability distribution of normalized end-to-end distances for real polymers is approximately:

$$P(x) \cong 0.278x^{0.28} \exp(-1.206x^{2.43}). \tag{3.7}$$

With this we can precisely define what we mean by a flexible backbone. Ideally, an MF design should be a $D_H = 5/3$ fractal object, respecting scaling laws of a real polymer as closely as possible, when not subjected to an external magnetic field. Designing the polymer backbone is only one aspect of MF design, and as we will see, needs to be done with the magnetic nature of MNPs in mind. In any case, with this, we have defined real polymers in terms of scaling laws.

3.4 RADIUS OF GYRATION

In Section 3.2, we introduced R_{ee}, denoting the distance traveled by a random walk, which is also the size of an ideal polymer. However, R_{ee} can be an ill-defined measure.[6] Instead, one should preferably use the normalized square radius of gyration R_g^{*2}, which is the average square distance between the monomers in a conformation, defined as:

$$R_g^{*2} = \frac{2}{d_{avg}^2 N^4} \sum_{i,j}^{N} (\vec{r}_i - \vec{r}_j)^2. \tag{3.8}$$

Here, $\vec{r}_i$ is the position vector of the i-th monomer in the lab coordinate frame and d_{avg} is the average inter-monomer distance. For polymers and fluctuating objects in general, one usually talks about ensemble averages, and it is implicit that R_g^{*2} stands for the mean-square radius of gyration.

It is illuminating to understand R_g^{*2} in terms of the gyration tensor:

$$G_{\mu\nu} = \frac{1}{N} \sum_{i=1}^{N} (r_{i,\mu} - r_{cm,\mu})(r_{i,\nu} - r_{cm,\nu}), \tag{3.9}$$

6 The beginning and the end of a polymer can be overlapping for example

where $r_{i,\mu}$ and $r_{cm,\mu}$ are the μ-th Cartesian components of the position of the i-th monomer and the center of mass, respectively.[7] The gyration tensor is a 3×3 symmetric matrix, which can always be diagonalized. The eigenvectors of $G_{\mu\nu}$ written in its eigenbasis are called principal moments of the gyration tensor. The sum of the squared eigenvalues corresponding to the principal moments is the squared radius of gyration $d_{avg}R_g^{*2}$. However, $G_{\mu\nu}$ is much more useful and descriptive of polymers and polymer-like structures than just the R_g^{*2}. In a basis chosen such that $G_{\mu\nu}$ is diagonal, and its eigenvalues are ordered in magnitude as $\lambda_x^2 < \lambda_y^2 < \lambda_z^2$, principal moments can be combined to give several descriptors of monomer distribution in a conformation. In no particular order, asphericity b is defined as:

$$b = \lambda_z^2 - \frac{1}{2}\left(\lambda_x^2 + \lambda_y^2\right). \tag{3.10}$$

b is a non-negative descriptor that quantifies how symmetrically are monomers distributed for along each coordinate axis. For example, for a spherical or cubic distribution of monomers $b = 0$.

Acylindricity c, is a non-negative descriptor defined as $\lambda_y^2 - \lambda_x^2$, describing the monomer distribution in the plane perpendicular to the longest principal axis. The relative shape anisotropy, κ^2, is defined as

$$\kappa^2 = \frac{3}{2}\frac{\lambda_x^4 + \lambda_y^4 + \lambda_z^4}{(\lambda_x^2 + \lambda_y^2 + \lambda_z^2)^2} - \frac{1}{2}. \tag{3.11}$$

κ^2 is bounded between zero and one. If $\kappa^2 = 0$, all points are spherically symmetric, while $\kappa^2 = 1$ signifies that all points lie on a line.

For an ideal polymer, R_g^{*2} is easily related with R_{ee} because the mean-squared distance of monomers i and j can be treated as a shorter i-to-j random walk, so $< (\vec{r}_i - \vec{r}_j)^2 >= (i-j)a^2$, where a is the length of uncorrelated steps. Therefore, for a flexible, ideal chain: $< d_{avg}R_g^{*2} >=< R_{ee}^2/6 >$. Despite the fact that this relation has been demonstrated for a particular model of polymers, R_g^{*2} and R_{ee}^* can largely be treated as analogous quantities in this work.

3.5 CENTRAL ATTRACTION AND POLYMERIC STABILIZATION

Colloidal suspensions were distinguished from other solutions by Thomas Graham. A colloidal suspension is, on face value, nothing more than chemicals immersed in a liquid. While simple to imagine, such a system is tremendously complex to describe. However, there are several levels of abstraction a soft matter physicist could engage in to obtain a more palatable, representative description of a colloidal suspension. One could manipulate the liquid to make it

7 In general, center-of-mass is defined as: $r_{cm} = \sum_i^N m_i\vec{r}_i / \sum_i^N m_i$, where r_i and m_i are the lab frame position and mass of i-th monomer.

chemically neutral with respect to the colloids. In this case, one can use very general models to treat the liquid and the description of the colloidal suspension becomes focused solely on the colloidal particles. For example, colloids tend to spontaneously clump together. In general, given a chemically inert fluid, this can be explained by the fact that colloids want to minimize their interfacial energy. A clump of colloids has a smaller area exposed to the fluid, and as such minimizes the interfacial energy. The forces that arise due to this tendency are known as van der Waals (νdW) forces, more frequently discussed in the context of atomic systems.[128] Electron density fluctuations in an atom generate a dipole moment which gives rise to a weak attractive force, known as London dispersion.[72] It is intuitive to imagine this effect in the context of colloidal suspensions. With decreasing inter-particle distance, the colloids begin to feel the νdW interaction between their respective atoms. In fact, since νdW forces are additive, at small inter-colloidal separations, they can be tremendous.[149]

Colloids usually have a relatively simple shape, certainly much more palatable compared to the variety in the molecular world. Even though νdW attraction can be attributed to the polarization of the particle surfaces and for MNPs, it has a dipolar nature, this interaction is short-ranged and effectively central. Therefore, given a simple enough shape, one can capture νdW interaction in a colloidal suspension with effective, spherically symmetric, short-range potentials between spherical particles. Commonly, and in this work, this is achieved using the Lennard-Jones (LJ) potential:

$$U_{LJ}(r) = 4\epsilon\left\{(\sigma/r)^{12} - (\sigma/r)^{6}\right\}, \tag{3.12}$$

and the value of the cut-off where r_{cut} is the interaction range and ϵ defines the strength of the interaction. We often use the terms νdW forces and central attraction interchangeably. It is important to underline that, even though one can, and usually does, take measures to render the background medium (fluid) in a suspension as chemically transparent as possible, one still needs to consider ramifications of νdW forces present in it. As colloids clump together, they necessarily displace the fluid molecules, which experience νdW force themselves. In practice this usually results in more coagulation than one might anticipate considering only inter-colloidal central attraction. Theoretically, this excess coagulation can be accounted for by exacerbating slightly the central attraction between the colloids.

For the purposes of engineering smart, highly magneto-responsive materials, coagulation is a very undesirable circumstance. Scaling laws we have outlined to define an ideal polymer are in fact not compatible with coagulation. In any case we have defined the scope of this thesis to revolve squarely around filament designs that, without an external magnetic field applied, should ideally behave like real

polymers. One of the techniques used to counteract coagulation due to νdW forces is to induce a repulsive interaction by covering the surface of colloidal particles with a protective coating. The choice of coating is paramount. For example, if the coating is molecularly similar to the colloid, it facilitates stronger νdW forces. However, if the coating chemically resembles the medium in a colloidal suspension (*i.e.*, similar dielectric properties), it can prevent coagulation. Suitable coatings consisting of polymeric molecules, typically surfactants, can be engineered to prevent aggregation and lead to a homogeneous dispersal of the colloids in a medium.[89, 149] Stabilization of colloids using a polymeric halo, forming metallopolymeric nanocomposites, works due to the conformational entropy of the extended chains. When coated colloids approach each other the polymeric halos start to overlap, causing a local decrease in entropy. The colloidal particles will repel due to the gain in entropy, hence the term entropic repulsion.

In this thesis, colloids of particular interest are MNPs that are more accurately described as metallopolymeric nanocomposites. Indeed, polymer mediated stabilization of MNPs is in fact the classical method of choice for stabilization MNPs in a non-aqueous carrier liquid, e.g., organic solvents like kerosene.[143] and has since been achieved in various ways. Here we highlight a strategy where MNPs are coated with single strained DNA.[8][168, 214]

8 Furthermore, as we will discuss in more detail in Part iii of the thesis, one can use DNA nanoobjects and encapsulate MNPs with them.[104] Given that DNA carries charge, static repulsion becomes an additional repulsion force working against νdW. However, electrostatics are outside the scope of this work, and are for all intents and purposes effectively composed in the steric and, if present, central attraction forces.

4

MAGNETISM

Magnetism is, presumably since the Maxwellian formulation of classical electromagnetism,[113] usually introduced as a part of electrodynamics. While it is in many ways analogous to electrostatics, magnetism comes with two important twists. The lack of a magnetic monopole, which would carry a hypothetical magnetic unit of charge, and the link between magnetic fields and motion tends to complicate the basic level analysis of the emerging phenomenology. As was suggested previously, working within the framework of magnetic nanoparticles offers some major simplifications. In fact, we will stick rigidly to those simplifications. While this limits how useful this work can be as a reference for magnetism, it is necessary to keep the work focused.

4.1 MAGNETIC NANOPARTICLES

> *Interstellar space, lunar samples, and meteorites have inclusive magnetic nanoparticles. The geomagnetic navigational aids in all migratory birds, fishes and other animals contain magnetic nanoparticles. The most common iron storage protein ferritin (*$[FeOOH]_n$ *containing magnetic nanoparticles) is present in almost every cell of plants and animals including humans. The human brain contains over 10⁸ magnetic nanoparticles of magnetite-maghemite per gram of tissue.[96]*
>
> — Sergey P. Gubin [71]

Magnetic nanoparticles are crucial for the research presented in this thesis. However, a comprehensive overview of magnetism, magnetic colloids and nanoparticles, or their types, synthesis and properties would be out of place. Instead, here we introduce only the necessary, in order to be able to digest the results with a similar overview as the author. Nanoparticle research is mainly concerned with preparation and characterization of "uniform" spherical forms of various sizes, which opened the doors to research of organized nanostructures, both fundamental and applied.[71] Nanoparticles are of great scientific interest because they form a bridge between bulk materials, molecules, and structures at an atomic level. Nanoobjects are physical objects with a diameter in the range of $1nm < d < 100nm$, whose properties differ appreciably from the corresponding bulk material. A nanoparticle is a quasi-zero-dimensional nanoobject in which all characteristic linear dimensions are of the same order of magnitude. When dealing with nanoparticles, magnetic properties are largely size dependent.

Typically, the term nanoparticle is somewhat interchangeably used with single-domain particles. However, it is possible to have particles, whose sizes are smaller than the domain size range

In general, they consist of a core, a shell, and often also external functional groups. Magnetic properties of nanoparticles are usually inherited from the core, typically sized between $2nm < d < 30nm$[1]

The magnetic core properties of nanoparticles are determined by factors such as the chemical composition, type, and degree of defectiveness of the crystal lattice, particle size and shape, morphology (for structurally inhomogeneous particles), the interaction of the particle with the surrounding matrix and the neighboring particles. By changing the nanoparticle size, shape, composition, and structure, one can control to an extent the magnetic characteristics of the structures based on them. Materials containing single-domain MNPs that are isolated in nonmagnetic matrices at distances comparable to their size, are most interesting for investigations in this work. Specifically, in the context of this thesis we are technically treating magnetic molecular clusters immersed in a dielectric nonmagnetic medium (*i.e.*, good solvent) as isolated MNPs. In other words, MNPs in this work are as identical, single-domain pseudo atoms with an overall magnetic moment.

We essentially use ferromagnetism as an umbrella term for ferri-, and anti-ferri and anti-ferromagnetic, while super-paramagnetism is an idealized representation of paramagnetic phenomenology.

The intrinsic magnetism of atoms arises from a combination of the spin and orbital angular momenta of the electrons within them. More precisely, it is the electron configuration (quantum numbers of the occupied atomic orbitals), which directly determines the magnetic properties of an atom. The ways in which these various momenta combine constructively and destructively, manifests in different forms of magnetic behavior in materials.[56] Magnetic nanoparticles fundamentally differ from classic magnetic materials because their single-domain structure can be described with a "collective spin". Therefore, when dealing with MNPs, we can lend ourselves a much-simplified treatment of magnetic properties. There is a multitude of different forms of magnetism that can be observed for MNPs. For the purposes of this work we distinguish only two edge cases of magnetism in nanoparticles, namely ferromagnetic nanoparticles with a large and permanent magnetic moment without the necessity for an external field, and perfectly polarizable, super-paramagnetic nanoparticles with no remanent magnetization outside external magnetic fields.[2]

Most of the currently known methods for synthesis yield nanoparticles with a broad size distribution (dispersion $> 10\%$). Control of reaction parameters does not always allow one to narrow down this distribution to the required range. Therefore, together with nanoparticle synthesis methods, separation techniques of nanoparticles into

1 For MNPs, this value coincides with the size of a magnetic domain in most bulk magnetic materials.

2 While these are reasonable assumptions for the purposes of our investigations, we are missing some key ideas introduced by Stoner-Wohlfarth[166] and Néel[118] that are very much in effect. We assume that dipole moments of individual nanoparticles are always aligned with the total magnetic field and that Néel relaxation is extremely long.

monodisperse fractions have proliferated. Nanoparticle synthesis methods cannot be considered separate from stabilization methods. On the nanoscale, particles have a huge surface energy. It is difficult to find an inert medium.[68] Furthermore, the surfaces of nanoparticles are usually chemically modified during synthesis, which appreciably affects the nanomaterial properties. Most magnetic materials used are either metals or metal oxides. Iron is a magnetically soft, ferromagnetic material with high magnetic moment density (about $220 emu/g$).[3] Iron nanoparticles in the size range below $20nm$ are super-paramagnetic. Among all iron oxides, magnetite is of most ubiquitous use and interest.[4] Throughout this thesis we use magnetite (Fe_3O_4) nanoparticles as a reference.

Polyethylene occupies a special place among the polymers that are used as the matrices for magnetic nanoparticle stabilization.

As previously established, MNPs of interest for this work are most accurately described as isolated magnetic molecular clusters forming metallopolymeric nanocomposites. As metallopolymeric nanocomposites, MNPs can have considerably improved physical, mechanical and magnetic properties (saturation magnetization, coercive force, etc.).[69, 70] This thesis leans on the fact that arrays of nanoscale magnetic particles have novel, exploitable, collective physical and magnetic properties, and broadly is about formalizing how and why exactly. The value of this work therefore lies in the fact that finely tunable assemblies of nanoparticles have substantially different properties from quasispherical nanoparticles and higher dimensional microstructures, which makes them unique class of nanomaterials and important object for nanotechnological developments.[78, 200]

However, the focus in this thesis is solely on nanoscopic magnetic filaments. These supramolecular systems are themselves organized 1D ensembles of metallopolymeric nanocomposites. In this sense one cannot distinguish effectively between magnetic filaments and a multitude of anisotropic, quasi-1D systems based on nanoparticles including high aspect-ratio nanoparticles (nanowires, nanorods, and nanotubes) and linear arrays of nanoparticles. However, this work revolves on our insistence that magnetic filaments are distinct. It is important to underline that while there is a breadth of designs of magneto-responsive micro- and nanoscopic systems that can be nominally considered as magnetic filaments,[8, 11–13, 15, 16, 21, 23, 24, 37, 47, 53, 60, 61, 64, 73, 77, 98, 109, 112, 156, 161, 162, 186, 194, 203, 204, 211, 217, 218] many of them are fundamentally incompatible with the idea of a polymer-like entity controllable with magnetic fields.

3 Iron and cobalt, are the basic metals for numerous magnetic compounds used in practice. Moreover, these bulk metals are characterized by high ferromagnetic transition temperatures (1043K, 1408K, and 650K, respectively) and rather high magnetic anisotropy ($4.72 \times 10^4 J/m^3$, $4.53 \times 10^5 J/m^3$, and $5.7 \times 10^3 J/m^3$, respectively).[35, 157]. Magnetic anisotropy is larger by 10 or 100 times for nanoparticle samples

4 In magnetite, iron cations are present in two valence states, Fe2+ and Fe3+, in an inverse spinel structure. The cubic spinel $Fe_3O_4$is ferrimagnetic at temperatures below 858K.

In conclusion of this section, we take a short digression to highlight the important role DNA molecules have in spatial organization of inorganic nanoparticles and for building up precisely controlled and reproducible nanoscopic structures such as magnetic filaments. There are numerous desirable properties that DNA has, such as recognition capability, highly selective binding, physicochemical and mechanical stability. This has not gone unnoticed. Iron oxide nanoparticle arrays and microstructures were formed via DNA templating and scaffolding already quite a while ago.[94, 119] Immobilized DNA complexes were used as templates or as iron-containing precursor material in the process of formation of organized iron oxide nanoparticulate structures.[63] We will come back to this point in Part iii, where we present research motivated by the relatively recent advancements in DNA-origami technology.

4.2 MAGNETIC INTERACTIONS

It is known that 1D structures of colloidal MNPs form under an applied magnetic field, predominately aligned along the field direction.[25, 95, 163, 199] This is a well known phenomenon in monodisperse, kerosene-based ferrofluids, where interesting patterns of Fe_3O_4 nanoparticles form in films, under applied parallel and perpendicular magnetic fields.[76, 97][5] Furthermore, it is known that colloidal MNPs depending on the particle size and magnetic properties can self-assemble into quasilinear chain structures without an external magnetic field applied.[39] The paragraph above summarizes some works and phenomenology observed for what is now considered to be the "classic" magneto-responsive system. It also underlines the key driving mechanisms that permeate the results in this thesis, namely dipole-dipole interactions, and Zeeman coupling.

The mathematical description of electromagnetism is quite robust, and we have fundamental understanding of such phenomenology on the level of quantum electrodynamics. However, we shall consider magnetic interactions only up to a level of description appropriate for understanding the results present. In classical electrodynamics, Maxwell introduced the vector potential $\Box\vec{A} = -\mu_0\vec{j}$, where $\vec{j}$ is the current density.[6] Current density in the context of magnetic colloids corresponds to the angular momentum of electrons.[7] We restrict our phenomenology to the electrostatic limit. For a localized current distribution of on atomic scales, $\vec{A}$ on inter-colloidal distances can clearly be approximated using the multipole expansion. We constrain our in-

5 This effect was for example used for the separation of large duplex DNA in a microchannel device prepared by soft lithography.[46]

6 We are using the Lorentz gauge and SI to white the second Maxwell equation, where μ_0 is the vacuum permeability

7 We do not make a distinction between orbital and spin angular momenta. By angular momentum we refer to the total angular momentum.

terest up to the dipolar approximation, because irrespective of the magnetic nanoparticle variant, in all but the most unusual of circumstances, the dominant contribution to the magnetic behavior is the dipolar term. Therefore, from $\vec{B} = \nabla \times \vec{A}$, we can obtain the standard form of the magnetic field of a magnetic dipole:

$$\vec{B}(\vec{\mu}, \vec{r}) = \nabla \times \vec{A}(\vec{r}) = \frac{\mu_0}{4\pi}[\frac{3(\vec{\mu} \cdot \vec{r})\vec{r} - \vec{\mu}|\vec{r}|^2}{|\vec{r}|^5}]. \tag{4.1}$$

The potential energy of a dipole moment in an external magnetic field, called Zeeman energy, is given by:

$$U_H(\vec{H}, \vec{\mu}) = -\mu_0 \vec{H} \cdot \vec{\mu}. \tag{4.2}$$

The dipole-dipole interaction potential due to dipole fields between two magnetic particles can be written by:

$$U_{dd}(\vec{r}_{ij}, \vec{\mu}_i, \vec{\mu}_j) = \frac{\mu_0}{4\pi}\left[\frac{\vec{\mu}_i \cdot \vec{\mu}_j}{r^3} - \frac{3(\vec{\mu}_i \cdot \vec{r}_{ij})(\vec{\mu}_j \cdot \vec{r}_{ij})}{r^5}\right], \tag{4.3}$$

where the inter-particle distance is $r = |\vec{r}_{ij}|$, and $\vec{r}_{ij} = \vec{r}_i - \vec{r}_j$ is the displacement vector connecting i and j particle, with dipole moments $\vec{\mu}_i$ and $\vec{\mu}_j$, respectively. A key signature of U_{dd} is that it has a global energy minimum for the so-called head-to-tail arrangement of dipole moments. The maximum of the interaction potential corresponds to an antiparallel collinear dipole arrangement. There are two inflection points, formed for side-by-side dipoles with antiparallel and parallel orientations, the former being energetically preferable.

4.3 MAGNETIZATION OF MNPS

To completely describe an electron in an atom, four quantum numbers are needed: energy (n), angular momentum (l), magnetic moment (m_l), and spin (m_s). Coincidentally, n, l and m_l denote the orbital.

Consider a system of N point dipoles, with a fixed volume at temperature T. As is, the system might as well be a kinetic gas or a colloidal suspension. In Chapter 4, intrinsic magnetism of atoms was described as a quantum mechanical effect. Atoms and molecules have atomic nuclei and electron clouds surrounding them. In fact, these electron clouds have structure, shells subshells and orbitals. Electrons within each orbital have specific energies and quantum states denoted by no less than 4 quantum numbers. No two electrons in an atom can occupy the same quantum state. Fully populated orbitals carry no net spin and therefore cannot cause a magnetic moment. For the sake of simplicity, the particles in the hypothetical system scrutinized in this section, have a lone, unpaired electron, that is responsible for a tiny magnetic moment in each of the particles. Outside an external magnetic field, these magnetic moments are subject to thermal fluctuations and as such on average, the system is not exhibiting any remanent magnetization. Once a magnetic field is applied, however, magnetic moments orient themselves along the external field $\vec{H}$ direction, due to Zeeman coupling. Therefore, with an external magnetic

field applied, the system is magnetized. In other words, magnetization is a measure of how aligned dipole moments are, with $\vec{H}$. A state in which all the dipole moments in a system are aligned with $\vec{H}$ is called saturation magnetization.

We outlined the two driving mechanisms in the system to be thermal fluctuation and Zeeman coupling. At equilibrium, given a temperature T and a magnetic field $\vec{H}$, the probability that a dipole moment $\vec{\mu}$ is at an angle θ with respect to $\vec{H}$, is given by:

$$p(E) = A \exp \frac{-E}{k_b T} = A \exp \frac{|\vec{\mu}||\vec{H}| \cos\theta}{k_b T}. \tag{4.4}$$

Clearly, the number of particles whose magnetic moment is at angle θ with respect to $\vec{H}$ is proportional to Eq. (4.4). The average magnetic moment of the system is the projection of the magnetic moments on the direction of the external magnetic field:

$$< \mu >= \frac{\int_0^\pi |\vec{\mu}| \cos\theta \exp \frac{|\vec{\mu}||\vec{H}| \cos\theta}{k_b T} \sin\theta d\theta}{\int_0^\pi \exp \frac{|\vec{\mu}||\vec{H}| \cos\theta}{k_b T} \sin\theta d\theta}. \tag{4.5}$$

Integration of Eq. (4.5) reveals that magnetization in proportional to the so-called Langevin magnetization function:

$$L(\alpha) = \coth(\alpha) - \frac{1}{\alpha};\ \alpha = (|\vec{\mu}||\vec{H}|)/(k_b T). \tag{4.6}$$

The obtained expression tells us that a system of magnetic particles is only as magnetic as much as the dipole moments of the particles in it are oriented along $\vec{H}$. Alignment of dipole moment with $\vec{H}$ is determined by the competition between thermal fluctuations and Zeeman coupling. So, the Langevin function essentially measures how remote a magnetic system is from saturation magnetization, given a T and $\vec{H}$.[8] Therefore, magnetization is determined as

$$\mu = L\left(\frac{|\vec{\mu}||\vec{H}|}{k_b T}\right) \mu_{sat}. \tag{4.7}$$

But why stop here. We can imagine this system to be even more hypothetical. Firstly, we refer to a somewhat arbitrary "system", the choice of which is of little consequence for the derivation above. Translational degrees of freedom have no relevance in the calculation we outlined. So, one could have just as well an Ising model-style grid of magnetic moments, inside a spherical volume for example. Each section on our grid corresponds to a magnetic domain. In fact, this is exactly the classical limit of the ideal multi-domain paramagnetic

8 The Langevin function also relates the average chain elongation and extension force (normalized by thermal energy) for an ideal polymer.

material model. On the nanoscale however, one can operate under the assumption that particles are single-domain. In this case we arrive at the interpretation of the Langevin magnetization law relevant for this thesis. Magnetization of a single, mono-domain nanoparticle, immersed in a homogeneous magnetic field, is given by the Langevin function. Clearly, there are advantages to the nanoscale beyond being able to write the entire 24 volumes of the Encyclopedia Britannica on the head of a pin, as famously suggested in a lecture by the brilliant Richard Feynman.[55]

Magnetic susceptibility χ is a measure of how magnetizable a material is in magnetic fields. It is calculated as the ratio between the saturation magnetization and strength of the magnetic field applied.

As far as dilute ferrofluids are concerned, their magnetic response is well represented by the Langevin magnetization law, in the limit of infinite dilution, where the magnetic colloids can be considered non-interacting.[159] In this case, we treat ferrofluids as an ideal paramagnetic gas of particles, suspended in a liquid carrier. However, with increasing density, this description falls apart.[9] The Langevin model completely neglects the fact that dipoles cause dipolar fields, and that dipole moments interact with each other. A number of theoretical models can evaluate magnetic properties taking into account the dipole-dipole interactions, but none more successfully than the Modified Mean Field Theory (MMFT2), as firstly presented in Ivanov and Kuznetsova.[10] Dipole-dipole interactions are reflected in inter-particle correlations. As such, MMFT2 is based on reinterpreting dipole-dipole interactions in terms of pair-correlation functions. MMFT2 is known to describe static magnetic properties of relatively concentrated ferrofluids well, if dipolar forces do not lead to cluster formation.[83] In the framework of MMFT2, the magnetization of a monodisperse system has the form:

$$\mu = \rho^* \mu_{max} L\left(\mu_{max} H_e\right), \tag{4.8}$$

$$H_e = H + \frac{1}{3}\zeta L(\gamma) + \frac{1}{48}\left(\zeta\right)^2 L(\gamma)\frac{dL(\gamma)}{dH}. \tag{4.9}$$

Here, μ_{max} is the saturation magnetization, $H \equiv |\vec{H}|$, $\gamma = \mu_{max} H$, $\zeta = \mu_{max}\rho^*$ and ρ^* is the magnetic particle number density. The derivation of Eq. (4.8) and Eq. (4.9) is quite involving. Instead, here we provide the outline of how one obtains them. In the derivation of the Langevin magnetization law, particles motion is only subject to thermal fluctuations and Zeeman coupling. This we know is a reasonable description of idealized paramagnetic materials and dilute ferrofluids. However, with that, one assumes implicitly that excluded

9 Initial magnetic susceptibility does not scale linearly with particle concentration, as is predicted by the Langevin magnetization law.

10 There for example are different variants of the mean-field models,[41, 122, 133, 179], mean-spherical models[114, 115, 196] and the thermodynamic perturbation model.[81]. All of them are only valid if the strength of dipole-dipole interactions is less than $k_b T$

volume, steric, van der Waals interactions are all irrelevant. All of them, together with electrostatic forces are very much present in a real ferrofluid. So firstly, one needs to introduce all the spherically symmetric steric interactions into the Hamiltonian governing the system. Furthermore, one needs to supplement Zeeman coupling with dipole-dipole interactions. The magnetization of a more realistic system, can be related to the partition function Q:

$$\mu = \frac{-1}{V}\frac{\partial}{\partial H}\left(-k_b T \ln Q\right), \tag{4.10}$$

where V is the volume of the system, and the Hamiltonian contains all relevant interactions. One can use perturbation theory to expand the dipole-dipole interaction potential in terms of $|\vec{\mu}|H/k_b T$. Equating this expression with an approach like in Eq. (4.5), we can obtain the explicit form of the probability for a single particle to be placed at a point in a volume V and to be oriented in a particular direction, which is the pair-correlation function of order k for k-th order perturbation theory expansion of the dipole-dipole interaction potential.

The elegance of mean field approaches is that they reinterpret the effects of inter-particle correlations arising from dipole-dipole interactions in terms of an effective magnetic field H_e. In particular, the model presented in Pshenichnikov, Mekhonoshin, and Lebedev [133] defines H_e by introducing a correction proportional to the Langevin magnetization of the magnetic particles in the system. Expansion of the expression for magnetization, obtained in this approach coincides with the results from the perturbation theory approach from Ivanov and Kuznetsova [82].[11] Equating the results of the two approaches gives the elegant form of MMFT2 magnetization, as given in Eq. (4.8) and (4.9).

11 Ivanov and Kuznetsova [82] used 2nd order perturbation theory dipole-dipole interaction corrections, and they match with the mean field approach in Pshenichnikov, Mekhonoshin, and Lebedev [133] up to $O(2)$ expansion terms.

Part II

SHAPING THE MAGNETIC RESPONSE OF NANOSCOPIC MAGNETIC FILAMENTS

The following chapters are dedicated to the study of the relationship between filament microstructure and monomer properties on one side, and structural and magnetic properties of MFs on the other, at equilibrium. As summarized in the Prologue, advantages in terms of magentoresponsiveness, of anisotropic and/or crosslinked structures compared to conventional magnetic fluids have been noted and sparked a great deal of research. However, in order to be able to unlock the full potential of MFs, it is necessary to understand, in a fundamental way, how all the elements that constitute a magnetic filament affect its properties. In this way, we establish general guidelines applicable to any magnetic filament design.

5

INTRODUCTION

A comprehensive description of the link between microstructure and monomer properties in a magnetic filament, and its structural and magnetic properties, at equilibrium, demands an exploration of filament phenomenology within broad, generalizable classes. The preceding discussion is constructed with generality in mind. Microstructure of a magnetic filament is defined by the arrangement of magnetic colloids crosslinked together to form the filament backbone. Therefore, understanding how microstructure relates to equilibrium properties of MFs, means encompassing MFs with a different number and arrangement of monomers, crosslinked together in various ways. When talking about monomer arrangement, instead of exploring a binomial distribution coefficient worth of possibilities for every length, we recognize that a filament backbone can have a uniform, a periodically non-uniform or aperiodically non-uniform arrangement of magnetic colloids. In this way, length scaling is redundant, and conclusions we draw from specific monomer arrangements are systematically generalizable. Crosslinking introduces correlations between monomers and restricts their degrees of freedom relative to each other. The following discussion focuses on two broad classes of MFs, that encompass most crosslinking approaches by considering what monomer degrees of freedom are coupled, and how rigid is the backbone. Therefore, the discussion of the relationship between filament properties and crosslinking consists of considering flexible vs rigid crosslinking and/or only translational vs both translational and rotational degrees of freedom coupling.

On the level of a single monomer, one can consider the size, shape, type of magnetic relaxation of MNPs, as well as central attraction due to the presence of electrostatic interactions for example. As discussed in Chapter 4, considering MFs with two types of magnetic colloids, namely ferromagnetic and super-paramagnetic ones, implicitly considers monomer size. These two types of MNPs, allow us to paint a high contrast picture of the complex interplay between the magnetic nature of monomers and filament microstructure, and their impact on the overall magnetic response of a magnetic filament. Here, electrostatic interactions and the possibility that the solvent is not chemically inert with respect to the colloids, are considered only in terms of a central attraction between the monomers.

5.1 CROSSLINKING

In this section, we present the crosslinking approaches we use, to scrutinize the relationship between filament microstructure and magnetoresponsiveness. We realize filament models, distinct in terms of stiffness and inter-monomer correlations, both for ferro- and superparamagnetic MNPs. These models are shown in Fig. 1.

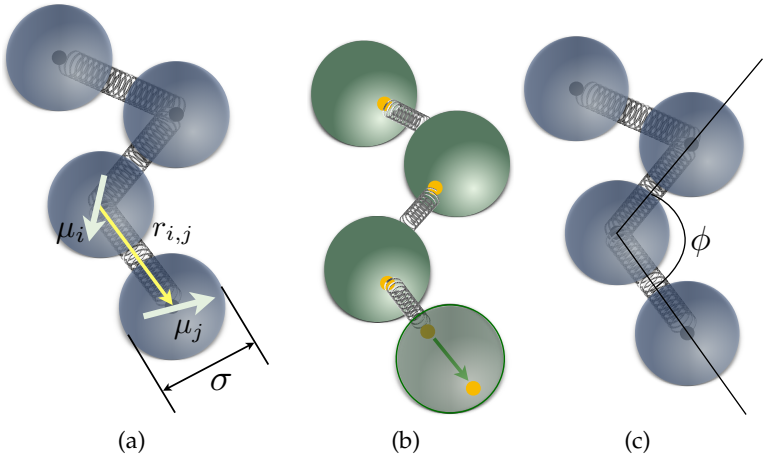

Figure 1: Schematic depictions of different bead-spring models of MFs. Dipole moments are shown as white arrows. The crosslinking is depicted as springs attached to either filament centers (black dots) or to anchoring sites with permanently fixed positions on the surface of MNPs (yellow dots).(a) CTC crosslinking; (b) Constrained crosslinking for MFs with ferromagnetic MNPs; (c) Constrained crosslinking for MFs with super-paramagnetic MNPs.

The crosslinking depicted in Fig. 1a is designed to represent MFs that have a very flexible backbone, with restrictions on only the translational motion of monomers. The filament backbone is implemented by linking monomers pairwise, center-to-center, with finitely extensible nonlinear elastic potential bonds (FENE). When defined as a function of the center-to-center distance r, the FENE potential takes the form:

$$U_{FENE}(r) = \frac{-K_f r_f^2}{2} \ln\left\{1 - \left(\frac{r}{r_f}\right)^2\right\}, \tag{5.1}$$

where r_f and K_f are the maximum extension and bond rigidity, respectively. Having all monomers in a line, connected pairwise, center-to-center, with FENE bonds, ensures close contact between adjacent monomers, without introducing any energetic penalty on their rotation. Therefore, the characteristic and energetically advantageous head-to-tail dipole moment configuration is achieved purely through the cooperative influence of dipolar fields generated by neighboring magnetic monomers and the external magnetic field (if applied). This

crosslinking approach is referred to throughout the thesis as CTC crosslinking, regardless of the magnetic nature of monomers.

The constrained crosslinking model, for both ferromagnetic and super-paramagnetic monomers, is designed to allow us to investigate the effects of increased (relative to CTC crosslinking) stiffness and inter-monomer correlations on the equilibrium properties of MFs. To achieve this for MFs with ferromagnetic monomers, we couple the relative orientations of the monomers and the filament backbone, by introducing anchoring sites for the FENE bonds (5.1) (see Fig. 1b). These anchoring sites have fixed positions corresponding to the projection of the head and the tail of the magnetic moments on the surface of the MNPs, similarly to works [152, 154, 155]. If we are dealing with isotopic shapes, relative orientation of super-paramagnetic monomers is meaningless. Super-paramagnetic MNPs have no remanent magnetization in the absence of an applied magnetic field. Given that dipole moments are the only "anisotropy" for perfectly spherical monomers, we can only introduce additional inter-monomer correlations and stiffness against bending, by adding an isotropic bending pair potential between first-nearest neighbors (see Fig 1c):

$$U_{bend}(\phi) = \frac{K_b}{2}(\phi - \phi_0)^2, \tag{5.2}$$

where ϕ is the angle between the vectors spanning from particle i to its nearest neighbor particle pair $(i-1, i+1)$, $i \in [2, N-1]$. K_b is the bending constant, while $\phi_0 = \pi$ is the equilibrium bond angle. The expression in Eq. (5.2) is a harmonic, angle dependent potential, included in the sketch shown in Fig. 1c. These crosslinking approaches are referred to throughout the thesis as **constrained** crosslinking, where it is implicit that for MFs with ferromagnetic MNPs we are referring to the model with anchoring sites, while for MFs with super-paramagnetic MNPs we are talking about direct crosslinking via the FENE potential with an additional bending potential.

5.2 THE MAGNETIC RESPONSE OF SUPER-PARAMAGNETIC MNPS

To model super-paramagnetic MNPs, one needs to accurately calculate the total magnetic field $\vec{H}_{tot}$ in each point of the system. The total magnetic field is the sum of $\vec{H}$ and the dipolar field $\vec{H}_d$. The latter field, created by particle j, at position $\vec{r}_0$ is given by:

$$\vec{H}_d = \frac{3\vec{r}_{0j} \cdot \vec{\mu}_j}{r_{0j}^5}\vec{r}_{0j} - \frac{\vec{\mu}_j}{r_{0j}^3}. \tag{5.3}$$

The study of the response of MFs to external magnetic fields of arbitrary strength requires one to define the dipole moment, $\vec{\mu}_i^s$, of an i-th super-paramagnetic particle at a given temperature T, as:

$$\vec{\mu}_i^s = \mu_{max} L\left(\frac{\mu_{max}|\vec{H}_{tot}|}{k_B T}\right)\frac{\vec{H}_{tot}}{H_{tot}}, \tag{5.4}$$

where $\mu_{max} = |\vec{\mu}_{max}|$ denotes the modulus of the maximal magnetic moment of the particle, $\vec{\mu}_{max}$. Here, k_B is the Boltzmann constant and $L(\alpha)$ is the Langevin function, given in Eq. (4.6) This approach allows us to consider nonlinear effects, in contrast to work Wei, Song, and Dobnikar [192] In fact, expression (5.4) is a generalization of mean-field approaches, such as the modified mean field approach,[82] with the difference that no assumptions were made when calculating $\vec{H}_{tot}$. This approach is also verified by analytical calculations of the magnetization of super-paramagnetic particles.[49]

In simulations, this calculation is not trivial to implement. One needs to freeze the system and calculate $\vec{H}_{tot}$ at the position of every particle in the system. For single filament simulations this is a calculation that scales as the square of the monomer number and cannot be efficiently parallelized. Furthermore, one needs to reset the dipole moment of every particle according to Eq.5.4. The fact that for every MD timestep one reassigns dipole moments means that we must recalculate forces for every half step of the Verlet algorithm (see. Section 2.2), which adds some overhead. One also needs to handle the fact that the orientation of a dipole moment is defined with respect to the particle director. Defining one, necessary defines the other. Therefore, reassigning a dipole moment will change the orientation of the particle. This is fatal for filament models where relative orientation of monomers is coupled. To avoid this issue, we instead placed a virtual site in the center of every monomer, that carries the monomer dipole moment instead, and has no quaternion.

5.3 UNITS AND IMPLEMENTATION NOTES

Results that follow, are obtained from simulations where the length scale was set to be in units of σ (introduced earlier as the monomer diameter). We set the reduced temperature of the Langevin thermostat to be $k_B T = 1$, corresponding to room temperature. For excluded volume (steric) interactions we use the Weeks-Chandler-Andersen pair potential (WCA),[191]:

$$U^{WCA}(i,j) = \begin{cases} 4\epsilon\left[\left(\frac{\sigma}{r_{ij}}\right)^{12} - \left(\frac{\sigma}{r_{ij}}\right)^{6}\right] + \epsilon & \text{if } r_{ij} < r_{cut} \\ 0 & \text{otherwise} \end{cases} \tag{5.5}$$

where σ is the characteristic diameter of the sphere, r_{ij} is the center-to-center distance between monomers i and j, and the cut-off value

is $r_{cut} = 2^{1/6}\sigma$. Parameter ϵ defines the energy scale of the repulsion. Since we set $\epsilon = 1$, this means that the energy in our simulations is measured in units of k_BT. We consider two values of the reduced, saturated magnetic moment $\mu^2_{max} = |\vec{\mu}_{max}|^2 = 1$ and $\mu^2_{max} = 3$, for a range of reduced external magnetic fields $H \leqslant 6$. Given a choice of a particular magnetic nanoparticle, such as using magnetite nanoparticles coated with a thin layer of stabilizing agent (*i.e.* oleic acid coating, 2nm thick), in the case of $\mu^2_{max} = 1$, σ corresponds (not uniquely) to a colloid with a magnetic core of 11nm with a dipole moment of $3.35x10^{-19}Am^2$,whereas for $\mu^2_{max} = 3$, σ corresponds (not uniquely) to a colloid with a magnetic core of 15nm with a dipole moment of $8.5x10^{-19}Am^2$. This also means that the maximum of the applied magnetic field range we explored represents moderate fields of only 0.05 T, for MNPs with $\mu^2_{max} = 1$ and 0.072 T, for MNPs with $\mu^2_{max} = 3$. The chosen range of magnetic field strength spans from an initially weak magnetic response to the saturation magnetization of MNPs. The factor K_f of the potential given in Eq. (5.1) is set to $K_f = 10$. The maximum extension of the FENE bond r_f, is set to $r_f = 2\sigma$. The bending constant K_b of the harmonic angle dependent potential given in Eq. (5.2), is set to $K_b = 3.2$.

Experimentally, CTC crosslinking could represent ferromagnetic or super-paramagnetic monomers enclosed into semi-flexible steric cages within a multiple-cage chain structure.[173] This would correspond to an effective crosslinking scenario, since the MNPs would not be physically bonded to the cages, rather trapped inside. This crosslinking mechanism, is however, more appropriate for representing crosslinking of super-paramagnetic MNPs. One can consider the free rotation of MNPs as equivalent to free dipole moment rotation within the colloid. We will elaborate more on why it is a more appropriate model for MFs with super-paramagnetic MNPs in Chapter 7.

The bending constant K_b of the harmonic angle dependent potential given in Eq. (5.2), is set to $K_b = 3.2$. Note that these parameters have been chosen so that the end-to-end distance of MFs with constrained crosslinking and ferromagnetic monomers is equal to their counterparts with super-paramagnetic monomers, at $H = 0$. Experimentally, our constrained crosslinking models should be representative of ferromagnetic and/or super-paramagnetic MNPs, bonded directly with semi-flexible polymer crosslinkers. This model should also generalize quite well to MFs realized with DNA origami techniques, where orientations of functionalized MNPs are rendered permanent with respect to the filament backbone, by attaching the MNPs to DNA patches inside steric DNA origami cages. The cages subsequently assemble and bond among themselves into linear conformations, by means of complementary binding vertices.[104, 173, 201].

6

FILAMENT MICROSTRUCTURE AS INTER-MONOMER CORRELATIONS

The main appeal of MFs lies in their responsiveness to external magnetic fields and their ability to maintain structural integrity. Investigating MFs with different crosslinking is interesting because soft matter systems with a microstructure defined via crosslinking have been shown to have much improved responsiveness to external magnetic fields compared to conventional ferrofluids.[153] The preceding discussion uses ferrofluids as a reference extensively, which is why in this chapter we focus solely on MFs with ferromagnetic monomers.

We start the discussion with Fig. 2, looking at the difference between normalized filament magnetization $\overline{m}^* = \overline{m}/(N\mu_{max})$, and the Langevin function, $L(H)$, as a function of the dimensionless applied magnetic field strength, $H = |\vec{H}|$. Filament magnetization m is calculated as the average value of the projection of filament magnetic moment, $\vec{\mu}_{tot} = \sum_{i=1}^{N} \vec{\mu}_i$, where $\vec{\mu}_i$ is the dipole moment of the i-th monomer and N is the monomer number, on to the direction of $\vec{H}$. The maximum dipole moment of a monomer is denoted with μ_{max}. Fig. 2 features a comparison between different arrangements of magnetic and non-magnetic monomers in a filament with 20 monomers. We address filament a configuration where all monomers are MNPs, referring to conventional filament; a configuration with an arbitrarily selected aperiodic sequence; a configuration with alternating, magnetic and nonmagnetic monomers. For the arbitrarily chosen filament configuration, denoted in Fig. 2 simply as "sequence", the number of MNPs is $N_{mag} = 12$. For filaments with an alternating configuration, the number of MNPs is $N_{mag} = 10$.

Along with $\overline{m}^* - L(H)$ profiles for different MNP arrangements and crosslinking models, each figure shows the difference between the Langevin magnetization given by Eq. (4.6) and the magnetization based on MMFT2, given in Eq. (4.8). To calculate the effective field in the framework of the MMFT2, we use the following approach. The total volume of the system is estimated as a sphere with a radius equal to the radius of gyration of a filament (see. Eq. (3.8)). Within this volume, we calculate the local volume fraction of magnetic particles. In Fig. 2, we always use the same volume fraction of magnetic particles obtained for the smallest radius of gyration observed in simulations, as MMFT2 is used to underline the impact of crosslinking.

Looking at Fig. 2a, one can see that MFs with weakly magnetic MNPs ($\mu_{max}^2 = 1$), and CTC crosslinking, are magnetically similar to ferrofluids. Magnetization deviation from the Langevin magneti-

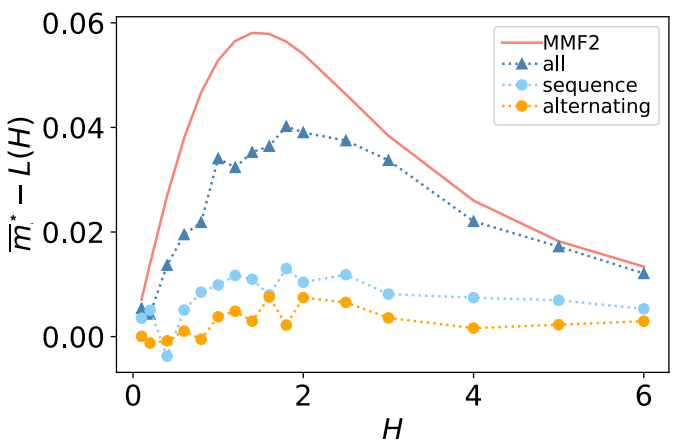

(a)

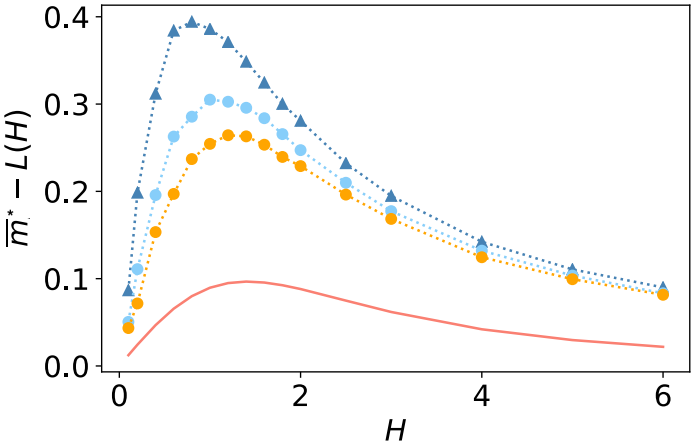

(b)

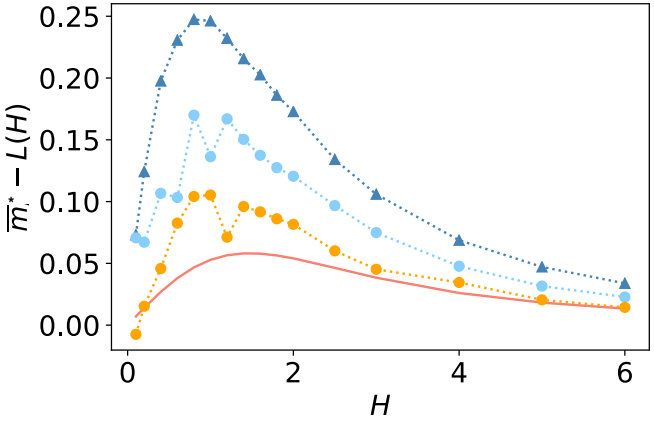

(c)

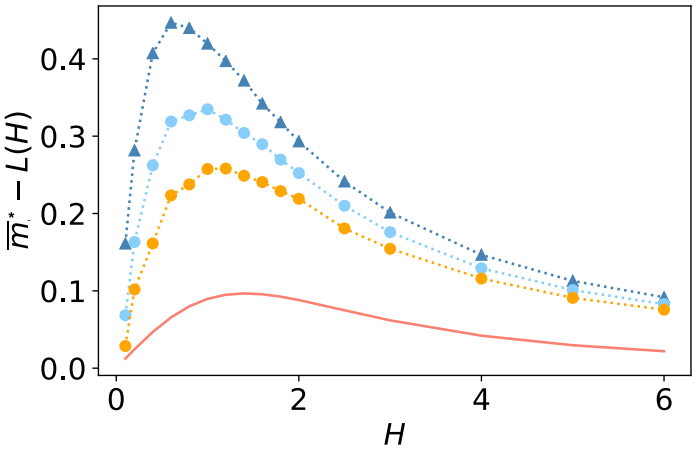

(d)

Figure 2: The difference between the normalized total magnetic moment of the filament, $\overline{m}^*$ and the Langevin function, L(H), for different crosslinking and μ^2_{max}. In all subfigures, MMFT2 is plotted with a full, salmon color line. The sequencing is annotated in the legend. In (a) and (b) we are showing results is for MFs with CTC crosslinking; (c) and (d) for MFs with constrained crosslinking; (a) and (c) for $\mu^2_{max} = 1$; (b) and (d) for $\mu^2_{max} = 3$.

zation law is at most 6%. The fact that Langevin and MMFT2 predictions agree so closely means that in this case dipole-dipole interaction potential corrections are small. Furthermore, crosslinking does not really contribute to the monomer pair-correlation function. However, for MNPs with $\mu^2_{max} = 3$ and/or constrained crosslinking, MFs exhibit an enhanced magnetic response to external magnetic fields compared to ferrofluids. For highly magnetic MNPs, dipole-dipole interactions are expected to impact inter-monomer correlations, and MMFT2 predictions differ significantly from the Langevin magnetization law. However, as can be seen in Fig. 2d, they are off by up to a factor of four in predicting the magnetization of MFs, for a moderately strong magnetic field ($H = 1.5$). This can only be attributed to crosslinking. Additional inter-monomer correlations that arise because of crosslinking are not considered in MMFT2. They, however, clearly make a difference. If we compare Fig. 2b and 2d, we can see that dipole-dipole interactions for $\mu^2_{max} = 3$ tend to dominate inter-monomer correlations, and differences based on crosslinking, while notable, are slight. Interestingly, constrained crosslinking increases the difference between magnetization curves corresponding to filament configurations where not all monomers are magnetic, independent of μ^2_{max}.

Comparing MFs with all magnetic monomers to MFs with alternating magnetic and nonmagnetic monomers, we see that roughly, double the number of MNPs leads to twice the magnetization. Essentially, we are increasing the average distance between the MNPs in MFs with alternating magnetic and nonmagnetic monomers. However, MFs with an irregular sequence have only 10% more MNPs yet can have up to double the magnetization that MFs with alternating magnetic and nonmagnetic monomers have. This can be rationalized if one imagines that the alternating configuration has homogeneously distributed correlations that are mild, while irregular sequence has an inhomogeneous distribution of very weak and very strong inter-monomer correlations. The latter, tend to percolate more than their immediate neighborhood and as such lead to a higher magnetization than expected. In other words, the alignment of a dipole moment with $\vec{H}$ in a filament with an irregular sequence of MNPs, depends on its position in the backbone, due to differences in the local dipolar fields.

This can be seen nicely by looking at per-particle magnetization $\overline{m}_{\#}$ along $\vec{H}$, shown in Fig. 3. In line with Fig. 2, for CTC crosslinking the overall magnetization is low in a weak magnetic field. We do not see an appreciable difference in per-particle magnetization in this case based on the arrangement of MNPs in a filament. Overall, inter-monomer correlations are low. With increasing μ^2_{max}, inter-monomer correlations increase and $\overline{m}_{\#}$ profiles for MFs with different arrangements of MNPs start to have features that we can distinguish. Inter-

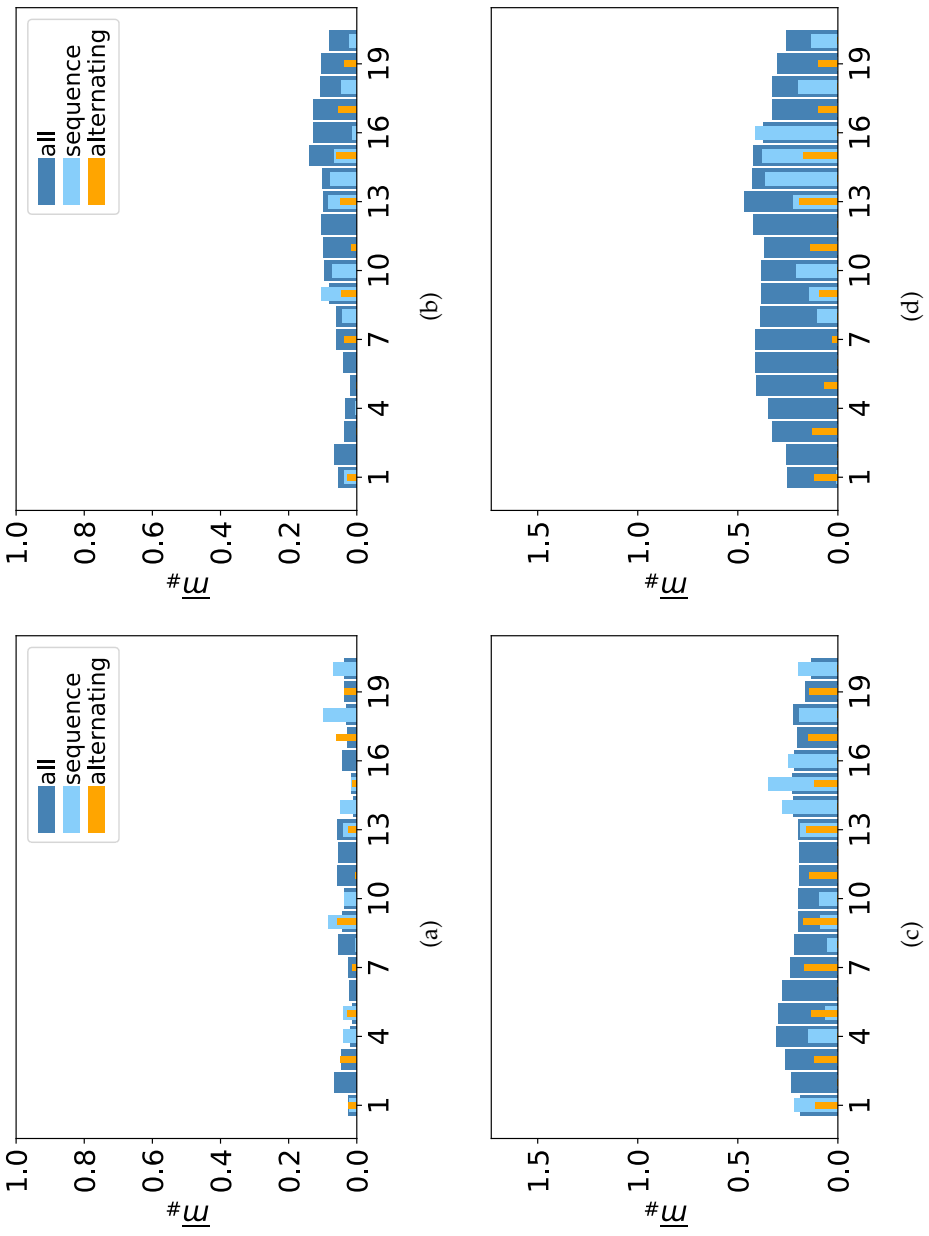

Figure 3: Showing per-particle magnetization $\overline{m}_\#$ along $\vec{H}$, in a weak H = 0.2 applied magnetic field. Particle positions are denoted on the x-axis. The sequencing is annotated in the legend. In (a) and (b) $\mu^2_{max} = 1$; in (c) and (d) $\mu^2_{max} = 3$. In (a) and (c) MFs are realized with CTC crosslinking; In (b) and (d) MFs are realized with constrained crosslinking.

monomer correlations seem to percolate less uniformly along the chain for CTC compared to constrained crosslinking. This can be seen if we compare Fig. 3c, corresponding to MFs where all monomers are magnetic, with their counterparts in either Fig. 3b or 3d, where in both cases, magnetic moments of neighboring monomers are more correlated and overall flatter profiles can be seen. Furthermore, with constrained crosslinking, one can see that MFs with an irregular sequence of MNPs have asymmetrical per-particle magnetization profiles, with the highest $\overline{m}_{\#}$ value around the position along the backbone with the most consequent magnetic monomers. From there, inter-monomer correlations percolate and diminish further down the chain, resembling the per-particle magnetization of MFs with the alternating MNP sequence.

7

MAGNETIC RESPONSE OF MFS

In Chapter 6 we rationalized filament microstructure in terms of inter-monomer correlations. To maximize the magnetic response of MFs with ferromagnetic monomers, regardless of the arrangement of MNPs, crosslinking that constrains both translational and rotational degrees of freedom is desirable. In general, inducing inter-monomer correlations that support synergetic orientation of individual dipole moments in a filament, increase its magnetic responsiveness. Furthermore, constrained crosslinking leads to larger differences in the magnetization between filaments with different MNP arrangement. Inter-monomer correlations also enhance local alignment of dipole moments with $\vec{H}$, depending on the particle position within filament conformation with a non-uniform arrangement of magnetic monomers. Regardless, filament designs where all monomers are magnetic are preferable. In this chapter we expand our investigation to consider the interplay between crosslinking and the magnetic nature of monomers, in MFs with exclusively magnetic monomers.

We start the discussion using measures adapted for polymer physics [148] to communicate how the magnetic nature of monomers in filaments, backbone rigidity and inter-monomer correlations, translate to experimentally measurable quantities, representative of structural properties of MFs. We calculate the normalized end-to-end distance, R^*_{ee}, as the distance between the centers of mass of the first and the N-th monomer:

$$R^*_{ee} = (|\vec{r}_1 - \vec{r}_N|)/d_{avg}, \tag{7.1}$$

where $N = 20$ and d_{avg} denotes the mean inter-monomer distance between neighboring monomers along the backbone. The value of d_{avg} is calculated separately for each crosslinking approach and H. Let us firstly consider results for MFs with CTC crosslinking. As it can be seen in Fig. 4a, for CTC crosslinking and $\mu^2_{max} = 1$, R^*_{ee} remains mostly flat as H increases, regardless of the magnetic nature of the monomers. Clearly, in this case magnetic interactions are weak and are dominated by entropy. For $\mu^2_{max} = 3$ we can observe an increase in R^*_{ee} with H. In fact, this increase is particularly pronounced for MFs with super-paramagnetic monomers (plotted with triangles), in the low field region ($H < 1$). For $H > 1$, we see largely flat profiles with similar R^*_{ee} values for MFs with ferro- (plotted with circles) and super-paramagnetic monomers. Observing a higher degree of stretching for MFs with super-paramagnetic monomers can be explained by the local orientation of dipole moments along $\vec{H}$. Such a local orientation is supported by dipolar interactions and leads to a head-to-tail

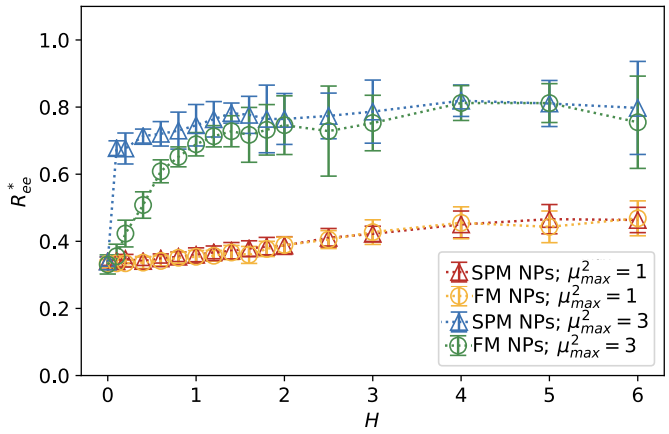

(a)

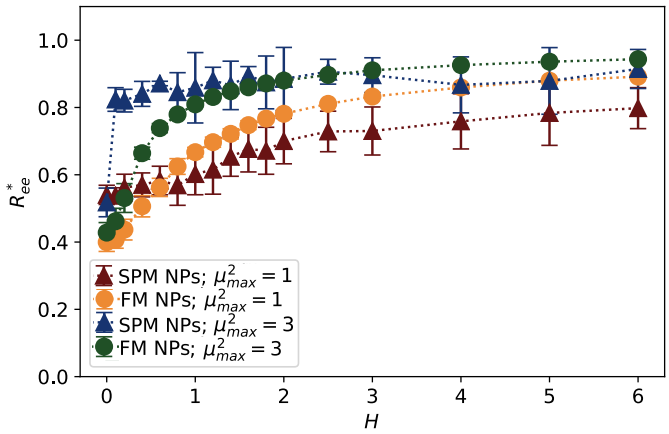

(b)

Figure 4: Normalized end-to-end distance, R^*_{ee}, as a function of H. (a) MFs with CTC crosslinking; (b) MFs with constrained crosslinking. Color coding for different μ^2_{max} is explained in the legends. SMP stands for super-paramagnetic monomers; FM – for ferromagnetic ones. Error bars are calculated as the standard deviation across 20 independent simulations.

alignment of the dipole moments and therefore, stretching of the filament backbone. In the case of MFs with ferromagnetic monomers and $\mu^2_{max} = 3$, the dipolar fields are not necessarily aligned with $\vec{H}$. Thus, for low-fields, MNPs are distributed to optimize dipolar forces. For global reorientation and stretching of a filament with ferromagnetic monomers to take place, high H is needed. For high values of H, magnetic nature of monomers becomes unimportant, and MFs reach a state where R^*_{ee} is approximately 20% lower than that of a straight rod.

Looking at R^*_{ee} profiles for MFs with constrained crosslinking, plotted in Fig. 4b, one can note that MFs are overall more stretched out compared to their counterparts with CTC crosslinking, regardless of μ^2_{max} and the magnetic nature of the monomers. We observe substan-

tial differences in R^*_{ee} based on the magnetic nature of monomers for MFs with constrained crosslinking, particularly for $\mu^2_{max} = 1$. In the low field region, similar to Fig. 4a, local stretching of MFs with super-paramagnetic monomers, with $\mu^2_{max} = 1$, is still more pronounced than that of their counterparts with ferromagnetic monomers. However, at $H \approx 0.8$ or greater, MFs with ferromagnetic monomers are notably straighter. Qualitatively, for $\mu^2_{max} = 3$ and constrained crosslinking, the behavior of R^*_{ee} is the same as for MFs with CTC crosslinking, discussed above: MFs with super-paramagnetic monomers stretch more in low fields than their counterparts with ferromagnetic ones. This difference disappears, however, as H increases. The analysis of R^*_{ee} curves reveals an important fact. Structural properties of MFs with CTC crosslinking, at equilibrium, are indistinguishable regardless of the magnetic nature of monomers.

In summary, based on the analysis of R^*_{ee}, if one had to recognize a singular distinguishing factor between MFs, the most appropriate one would not be the magnetic nature of the monomers, but rather the crosslinking approach. Constrained crosslinking not only increases the overall value of R^*_{ee} but is necessary to be able to obtain a significant difference in field-induced stretching between MFs with ferromagnetic and super-paramagnetic monomers. The dipolar strength has a larger impact on R^*_{ee} for MFs with CTC crosslinking: the value of R^*_{ee} for $\mu^2_{max} = 1$ is almost two times smaller than for $\mu^2_{max} = 3$ at high H. The same measure differs at most 15% for MFs with constrained crosslinking. Finally, none of the MFs studied here stretch to their full length under the influence of an applied magnetic field.

To obtain a better understanding of the local structure for different MFs, we measured the angle θ between segments within a filament with $\mu^2_{max} = 3$, separated by a given amount of bonds, l, as shown in Fig. 5a. A segment is defined as a pair of neighboring monomers together with the bond between them. Here, if the segments are touching, like in the case of segments between monomers $1-2$ and $2-3$, which are sharing a common monomer, $l = 0$ and the measured angle is addressed as θ_0. If the segments are immediately next to each other, but do not share a common monomer, in other words, if they are separated by a single bond, as is the case between segments formed by monomers $1-2$ and $3-4$, $l = 1$ and correspondingly define an angle θ_1. Analogously, θ_2 is the angle between segments $1-2$ and $4-5$, which are separated by two bond lengths. We measure the inter-segment correlations by calculating the cosine of the angle θ_l, $\langle \cos\theta_l \rangle$. The averaging is done first over all segments separated by l bonds, then over all snapshots for a particular simulation, and, finally, over all runs. Regardless of crosslinking and magnetic nature of the monomers, the more separated the segments are, the less they are correlated. However, segments in MFs with constrained crosslink-

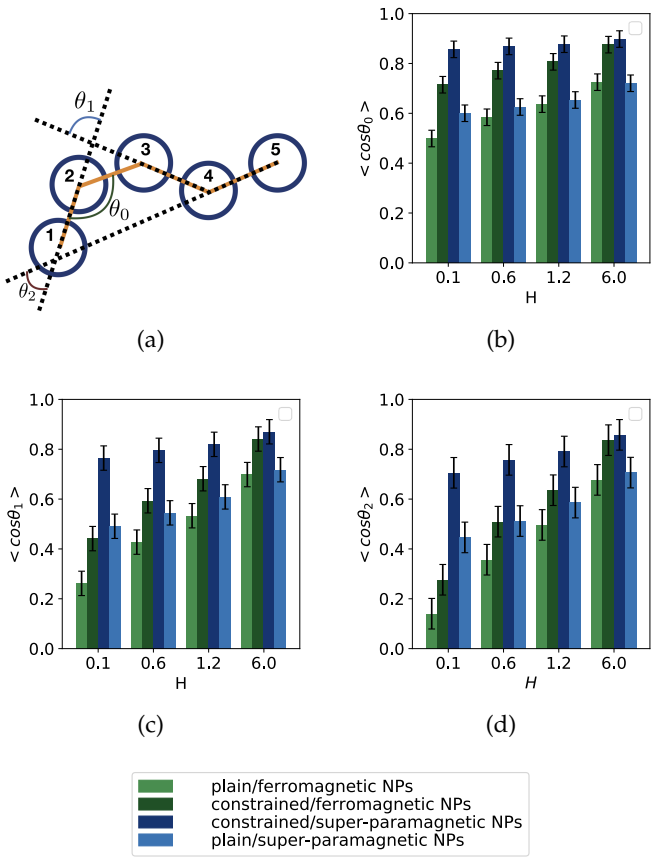

Figure 5: Inter-segment correlations $\langle \cos\theta_l \rangle$, for four different values of H. (a) $\langle \cos\theta_0 \rangle$; (b) $\langle \cos\theta_1 \rangle$; (c) $\langle \cos\theta_2 \rangle$. Each bar shows a particular combination of magnetic nature of monomers and crosslinking approach, as explained in the legend provided in (e). Results are shown for $\mu^2_{max} = 3$. Error bars are calculated as the standard deviation of the measure in question ($\langle \cos\theta_0 \rangle$, $\langle \cos\theta_1 \rangle$, $\langle \cos\theta_2 \rangle$, respectively), across 20 independent simulations.

ing (middle two columns in each bar plot) are more correlated than their counterparts with CTC crosslinking, and the value of $\langle \cos\theta_l \rangle$ decays weakly with increasing l. Inter-segment correlations strengthen with growing H. Comparing the left most and the right most columns in each bar plot for $\langle \cos\theta_0 \rangle$ shown in Fig. 5b, one can notice that for weak fields, neighboring segments in MFs with CTC crosslinking and super-paramagnetic monomers (right most columns) are more correlated than they are in MFs with ferromagnetic monomers (left most columns). The difference decreases and basically vanishes with growing H. This behavior explains why R^*_{ee} for MFs with CTC crosslinking, is found to be higher for super-paramagnetic monomers than for ferromagnetic ones, only in low H (see Figs. 4a).

Spatial correlations in MFs with super-paramagnetic monomers and constrained crosslinking (right middle column in each bar plot),

coincide with those of MFs with ferromagnetic monomers (left middle column in each bar plot) only for the highest value of H we explored. For lower H, segments in MFs with constrained crosslinking and super-paramagnetic monomers turn out to be more correlated than their counterparts with ferromagnetic monomers. The difference in correlations grows with l. So, MFs with super-paramagnetic monomers and constrained crosslinking exhibit spatial correlations that percolate further along the filament backbone. This observation explains why, in Fig. 4b, MFs with constrained crosslinking have significantly higher R^*_{ee} if they have super-paramagnetic monomers rather than ferromagnetic ones, especially for $H < 2$. The intricate relationship between the magnetic nature of monomers within a filament and crosslinking can result in notably different structural properties and responsiveness of MFs to external magnetic fields. We continue the analysis of the magnetic response of MFs by looking at how the interplay between crosslinking and magnetic nature of monomers reflects in the magnetization of MFs and compare it to the magnetic response of non-crosslinked magnetic soft matter systems, such as conventional ferrofluids.[82, 148]

In order to understand, how spatial correlations between filament segments are related to the overall magnetic response of MFs, we analyze the normalized filament magnetization $\overline{m}^*$ as a function H, shown in Fig. 6. For MFs with non-interacting monomers, corresponding field dependence of $\overline{m}^*$ would follow the Langevin function of $\alpha = \mu_{max} H$, given in Eq. (4.6), that is plotted in each subfigure of Fig. 6 with a black, solid line. Even for $\mu^2_{max} = 1$ and CTC crosslinking, shown in Fig. 6a, filament inter-monomer correlations manifest themselves, as the actual magnetization is above the Langevin curve. As we saw above, structural properties of MFs with CTC crosslinking and $\mu^2_{max} = 1$, are almost independent of H. To confirm that the magnetic response of a filament in this case is equivalent to the response that non-crosslinked monomers would have, we consider $\overline{m}^*$ calculated via MMFT2.[82]

As we did in Chapter 6, we assume that for a given value of H, all MNPs are constrained to a volume $V = 4\pi R_g^3/3$, so $\rho^* = N/V$. The results of Eq. (4.8) are plotted in all subfigures of Fig. 6 with a solid gray line. It can be seen in Fig. 6a that for $\mu^2_{max} = 1$ and CTC crosslinking, MMFT2 describes the magnetization of MFs well. Clearly, in this case the crosslinking does not affect the magnetic response of the individual monomers. For all other parameter sets however, the crosslinking enhances $\overline{m}^*$, especially in the low-H region: simulation data is well above the MMFT2 curve. Looking at $\overline{m}^*$ of MFs with $\mu^2_{max} = 1$ and constrained crosslinking, shown in Fig. 6c, one can see that $\overline{m}^*$ is lower for MFs with super-paramagnetic monomers. This fact agrees with the field-dependence of R^*_{ee}, plotted in Fig. 4a, showing that MFs with $\mu^2_{max} = 1$ and constrained crosslinking can

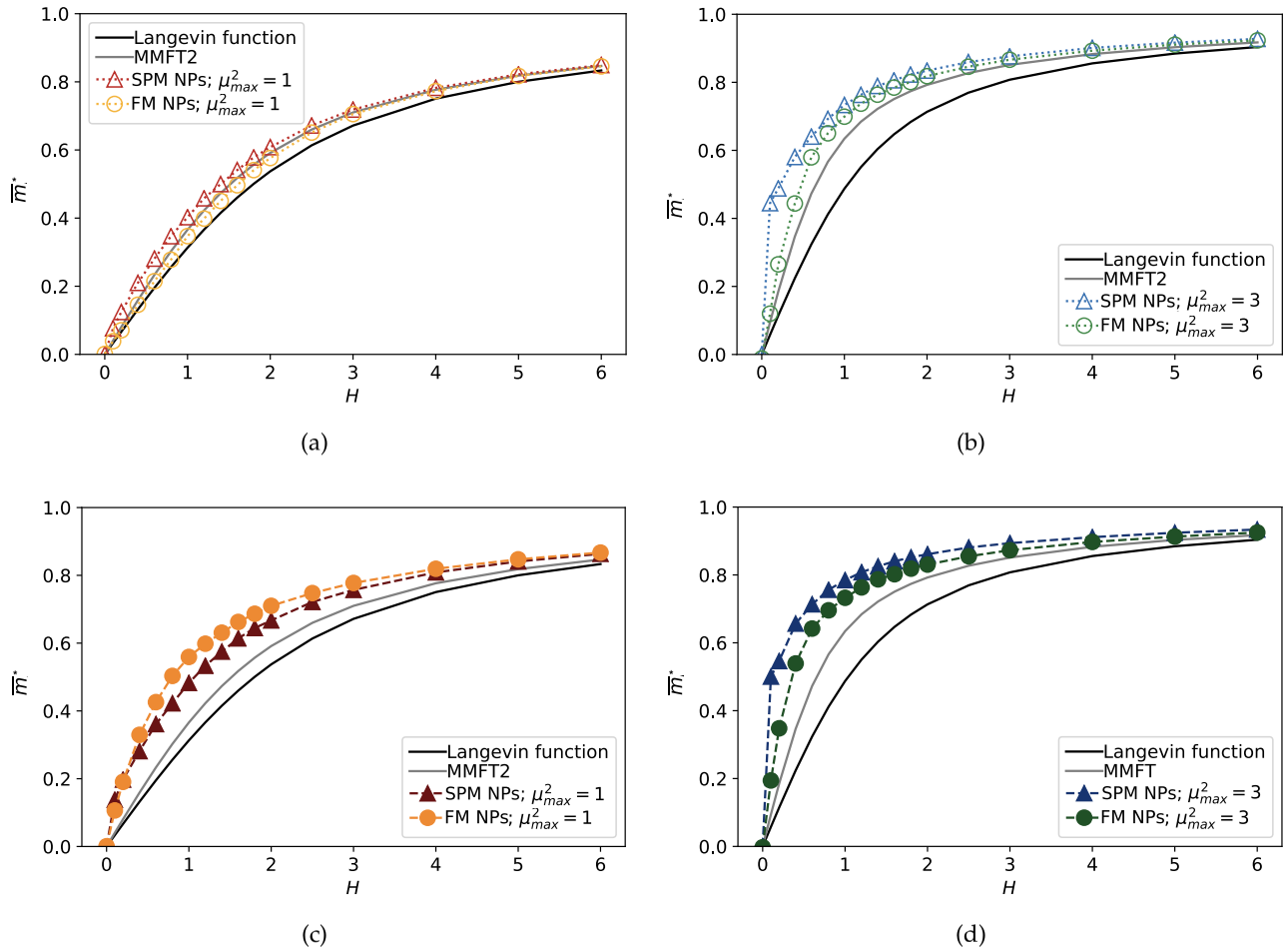

Figure 6: Normalized filament magnetization $\overline{m}^*$ as a function of the dimensionless magnetic field strength H. (a) and (b) MFs with CTC crosslinking; (c) and (d) correspond to MFs with constrained crosslinking. In (a) and (c) $\mu^2_{max} = 1$; in (b) and (d) $\mu^2_{max} = 3$. Each subplot shows four curves, representing results for MFs with either ferro- or super-paramagnetic NPs, Langevin magnetization law from Eq. (4.6) and MMFT2 from Eq. (4.8) (see the legend). Error bars are comparable to symbol size and are as such not shown.

be stretched and magnetized more easily if the monomers are ferromagnetic. This changes, however, if $\mu^2_{max} = 3$, as it can be seen in Figs. 6b and 6d. Independent of crosslinking, $\overline{m}^*$ for a filament with super-paramagnetic monomers is higher than for a filament with ferromagnetic ones, as is shown above in Fig. 4. This is rather similar to what we previously discussed for R^*_{ee}. Comparing the results from Figs. 6b and 6d to correlation plots in Fig. 5, one can notice that for constrained crosslinking models, MFs with super-paramagnetic monomers, that are comparatively more correlated, exhibit higher magnetization.

In summary, one can say that for $\mu^2_{max} = 1$, the highest $\overline{m}^*$ is observed for MFs with ferromagnetic monomers and constrained crosslinking. Furthermore, such MFs stretch more in applied magnetic fields and their $\overline{m}^*$ grows faster with H, than for MFs with super-paramagnetic monomers. The end-to-end distance of such MFs in the region of magnetic saturation is comparable to that of filaments with $\mu^2_{max} = 3$. In general, for $\mu^2_{max} = 3$, we observe the highest $\overline{m}^*$, R^*_{ee} and spatial correlations in high H fields for MFs with constrained crosslinking and super-paramagnetic monomers. This is in contrast to what we have seen for $\mu^2_{max} = 1$.

8

FREE ENERGY OF MFS IN A STRONG MAGNETIC FIELD

In Chapter 6 and 7 we obtained a broad understanding of how filament microstructure, and the interplay between the magnetic nature of monomers and crosslinking affect properties of MFs at equilibrium. It is necessarily to point out that while the aforementioned properties can be very similar between MFs with ferromagnetic and superparamagnetic properties, the way they reach equilibrium is quite different. With strong magnetic fields applied, one expects that minimization of dipolar (Eq. (4.3)) and Zeeman (Eq. (5.3)) energies should necessarily lead to the elongated filament conformations. However, independent of crosslinking, MFs with super-paramagnetic monomers can persist in conformations with a bent backbone, as schematically depicted in Fig. 7.

This kind of bending is visually similar to the behavior of polymers in nematic fields, observed in Tkachenko and Rabin [175], or the bending of ferromagnetic micron-sized filaments reported in Ērglis, Livanovičs, and Cēbers [51]. However, none of the two scenarios can be realized in our systems: instead of a quadrupolar nematic field,[175] MFs with magnetic nanoparticles experience Zeeman linear coupling and the interaction between monomers is quadratic. As a result, instead of stretching, at high fields, we observe chain bending; instead of dynamic bending found in Ērglis, Livanovičs, and Cēbers [51], here, we find equilibrium conformations of MFs with super-paramagnetic monomers in a strong static homogeneous magnetic field. In this chapter, to shed light on the mechanism leading to bending in MFs with super-paramagnetic monomers, we introduce an idealized theoretical approach that encompasses the competition between entropy and magnetic interactions, based on the combination of Flory approach and direct calculation of dipolar interactions, for a folded magnetic filament.

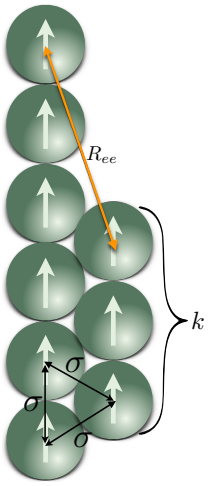

Figure 7: Schematic depiction of a folded filament. The legs of the folded chain are at σ distance one from another. All dipole moments are aligned with $\vec{H}$ and at μ_{max}. Length of the shorter leg k.

Let us assume that the Zeeman coupling is strong enough, so that all dipoles in a filament consisting of N monomers, are pointing in the same direction, as shown in Fig. 7. We also assume that all MNPs are at saturation magnetization $\mu = |\vec{\mu}_{max}|$, independent of the magnetic nature of the monomers. We expect a competition between three contributions to the free energy of a filament: entropy, that favors a coiled configuration, Zeeman energy, which is constant under our assumptions, and dipolar interactions, that favor a head-to-tail orientation of dipoles. We calculate the contribution of dipole-dipole interactions to the free energy, by splitting U_{dip} into a head-to-tail term, U_{htt}, and

a diagonal term, U_{dia}: $U_{dip} = U_{htt} + U_{dia}$. Both terms depend on the folding, characterized in our model by the number of monomers in the shorter leg of the folded filament, $k \leqslant \lfloor N/2 \rfloor$, as shown in Fig. 7. To simplify the calculations, we assume that the two legs of a folded filament are touching and the separation between all touching monomers is σ. U_{htt} and U_{dia} are the sums of pair dipole-dipole interactions $U_{dd}(\vec{r}_{ij}; \vec{\mu}_i; \vec{\mu}_j)$, given by Eq. (4.3), where the distances between monomers do not fluctuate and can be calculated exactly. In the approximation where monomer positions and dipolar orientations are fixed to $\vec{r_0}$ and $\vec{\Omega_0}$ respectively, we can get rid of the integration in the partition function over coordinates, $\vec{r}$ and orientations, $\vec{\Omega}$, using the delta-function property

$$\frac{F_{htt}}{k_B T} = \ln \frac{1}{A} \int d\vec{r} d\vec{\Omega} e^{\frac{U_{htt}(\vec{r},\vec{\Omega})}{k_B T}} \delta(\vec{r} = \vec{r_0}, \vec{\Omega} = \vec{\Omega_0}). \tag{8.1}$$

Up to a normalization constant A, this brings us to an estimate of $F_{htt}/(k_B T) = U_{htt}/(k_B T)$:

$$\frac{F_{htt}(k, \mu, \sigma, N)}{k_B T} = \frac{-2\mu_{max}^2}{\sigma^3 k_B T} \left(\sum_{i=1}^{N-k} \frac{N-k-i}{i^3} + \sum_{j=1}^{k} \frac{k-j}{j^3} \right). \tag{8.2}$$

This expression is identical to the chain ground state energy,[132] and was successfully used to estimate chain free energies at low temperature.[91] Following the same approach and using the same set of approximations as in Eq. (8.1), U_{dia} that contains the sum of all monomer interactions not belonging to the same fold, contributes to the free energy of a filament as $F_{dia}/(k_B T) = U_{dia}/(k_B T)$:

$$\frac{F_{dia}(k, \mu, \sigma, N)}{k_B T} = -\begin{cases} \frac{\mu_{max}^2}{\sigma^3 k_B T} \sum_{i=0}^{N_1(k,N)} \frac{I(i,k,N)}{r_i^3} \left(\frac{9}{4r_i^2} - 2 \right) & K_{cr} \geqslant k \\ \frac{\mu_{max}^2}{\sigma^3 k_B T} \sum_{i=0}^{N_2(k,N)} \frac{I(i,k,N)}{r_i^3} \left(\frac{9}{4r_i^2} - 2 \right) & \text{otherwise.} \end{cases} \tag{8.3}$$

Here, $r_i = \sqrt{1 + i + i^2}$. The upper limits of the summation are defined as

$$N_1(k, N) = k + (N - 2k - 1 + |N - 2k - 1|)/2;$$
$$N_2(k, N) = N - k - 2.$$

The factor $I(i, k, N)$ gives the number of monomer pairs with the same interaction energy. The calculation of $I(i, k, N)$ for arbitrary values of

k and N is a non-trivial task which results in the following expression:

$$I(i,k,N) = \begin{cases} \begin{cases} k & k \leqslant i \leqslant N-2k-1 \\ 2k-i & i < k \\ N-k-i-1 & \text{otherwise} \end{cases} & K_{cr}(N) \geqslant k \\ \begin{cases} 2k-i & i \leqslant N-2k-1 \\ N-2i-1 & N-2k-1 \leqslant i \leqslant k \\ N-k-i-1 & \text{otherwise} \end{cases} & \text{otherwise,} \end{cases} \tag{8.4}$$

where K_{cr} depends only on filament length, N:

$$K_{cr}(N) = \begin{cases} \frac{N}{3} & N \bmod 3 \neq 0 \\ \frac{N}{3} - 1 & \text{otherwise.} \end{cases} \tag{8.5}$$

The total dipolar contribution to the free energy of a folded filament can be written as:

$$\frac{F_D(k,\mu,\sigma,N)}{k_B T} = \frac{F_{htt}(k,N,\sigma,\mu) + F_{dia}(k,N,\sigma,\mu)}{k_B T}. \tag{8.6}$$

The total Zeeman energy of a filament, U_H, does not depend on k. Therefore, its contribution to the free energy of a filament, after getting rid of the integral and logarithm, simplifies to $F_H/(k_B T) = -U_H/(k_B T)$. Finally, following the Flory approximation of the free energy of a polymer in a good solvent without magnetic interactions,[148] F_{NM}, with an entropic and a steric term, F_{ent} and F_s respectively, can be written as:

$$\begin{aligned} \frac{F_{NM}(k,\sigma,N)}{k_B T} &= \frac{F_{ent}(k,\sigma,N) + F_s(k,\sigma,N)}{k_B T} \\ &= \frac{R_{ee}^2(k,\sigma,N)}{N\sigma^2} + \frac{\pi}{6}\sigma^3 \frac{N^2}{R_{ee}^3(k,\sigma,N)}. \end{aligned} \tag{8.7}$$

Here, we use end-to-end distance R_{ee}, as a function of k, σ and N, which, by using the cosine theorem, can be obtained in the following form:

$$R_{ee} = \sigma\sqrt{(N-2k)(N-2k-1)+1}.$$

Summing all terms up, assuming $\sigma = 1$, one can obtain the free energy of an "ideally" folded filament, as a function of k, N and μ:

$$F(k,\mu,N) = F_{NM}(k,N) + F_D(k,\mu,N) + F_H(\mu,N). \tag{8.8}$$

We want to depict the dependence of F_D on k, for different values of monomer number in a filament N. To compare F_D values corresponding to a straight filament $F_D(0,\mu,N)$, to the one a folded filament would have, in Fig. 8, we plot the μ-independent dimensionless ratio:

$$\Delta F_D = \frac{F_D(k,\mu,N) - F_D(0,\mu,N)}{N|F_D(0,\mu,N)|}. \tag{8.9}$$

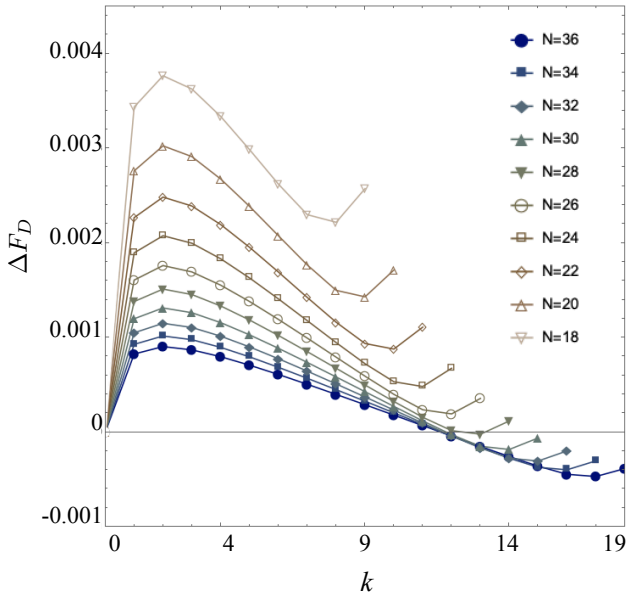

Figure 8: ΔF_D from Eq. (8.9) as a function of k, for different values of MF length N as indicated in the legend.

In this way, all curves collapse to zero at $k = 0$, and the positive values of ΔF_D correspond to a parameter region where the free energy of a folded filament is higher than that of a straight one. One can see, that for MFs with less than $N = 28$ monomers, it is magnetically more advantageous to assume a straight conformation. However, along with the minimum at $k = 0$, an increase of N leads to the development of a second minimum at $k \sim N/2 - 1$, separated from the first one by a barrier. In fact, for $N > 28$, we see that ΔF_D becomes negative for $k > 12$, revealing that the folded state becomes more advantageous than the straight one.

In this chapter, however, we discussed and noted folding for MFs with $N = 20$: Eq. (8.9) shows that considering only dipolar contribution, such MFs should have remained unfolded. Thus, in Fig. 9, we plot the total free energy difference between a straight filament and a folded one ΔF_T, for $N = 20$ and different values of μ and k:

$$\Delta F_T(k, \mu) = \frac{F(k, \mu, 20) - F(0, \mu, 20)}{20}. \tag{8.10}$$

Lighter color shades in the color map of ΔF_T, correspond to higher values of $\Delta F_T(k, \mu)$. The total free energy difference can be positive, only if the straight conformation is more advantageous than the bent one. Correspondingly, ΔF_T will be negative if a bent conformation is more advantageous than a straight one. Vertical lines correspond to a given k, contour lines show regions of constant ΔF_T. One can see that for small values of μ (bottom part of Fig. 9), the minimum of ΔF_T is around $k = 6 - 7$, and basically any folding is leading to a free energy decrease compared to the $k = 0$ case. The picture changes

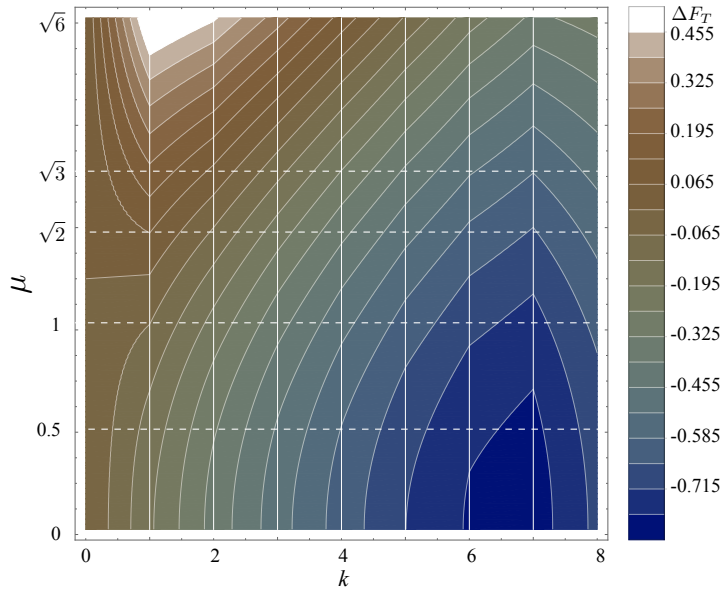

Figure 9: Color map of ΔF_T for MFs with 20 monomers, in simulation units from Eq. (8.10) for different values of k and μ. Contour lines indicate constant values of ΔF_T; vertical white lines show $k = const$ cuts, whereas dashed horizontal lines show $\mu = const$ sections. Color coding is provided in the legend on the right.

dramatically with increasing μ: a maximum of ΔF_T starts developing at $k \sim 1-2$, whereas the minimum corresponding to a folded state abates, but never disappears. In other words, a filament needs to overcome a barrier introduced by the dipole-dipole interaction, in order to bend. Once folded, however, it reaches its global minimum of the free energy. Note that R^*_{ee} corresponding to the values of $k \sim 6-7$, for which ΔF_T is minimized, is in a good agreement with R^*_{ee} presented in Fig. 4a, where for MFs with super-paramagnetic monomers and CTC crosslinking $R^*_{ee} \sim 0.4-0.5$.

To summarize this section, one should underline that bending has not only entropic but also energetic advantages, especially for long magnetic filaments ($N \geqslant 30$). At the filament length considered in this chapter, however, bending corresponds to local energy minima, but is favored by entropy at finite temperature.

9

CENTRAL ATTRACTION IN MFS WITH SUPER-PARAMAGNETIC MONOMERS

In Section 3.5 we introduced the concept of *vdW* forces. To avoid aggregation, one would try to render the background medium in a suspension as chemically transparent as possible and stabilize magnetic colloids. Regardless, it remains a matter of fact that vdW forces will be present to some degree in real suspensions of MFs. Here, we focus on a magnetic filament that has a slight affinity towards its own species rather than the solvent. We want to understand in a general way, how the presence of *vdW* forces affects the magnetic response of MFs. In particular, the focus in this chapter is on MFs with super-paramagnetic monomers. Given their tendency to bend the backbone, resulting in a very diverse and rich conformational spectrum, it stands to reason to expect *vdW* forces affecting the observed phenomenology greatly.

We have seen in Fig. 4, that MFs with weakly magnetic monomers and CTC crosslinking are essentially coiled up, and remain so across the range of H we explored. In this case magnetic interactions are weak and are dominated by entropy. With central attraction between monomers, one can reach even more compact conformations of MFs, as the system attempts to maximize the average number of neighbors for each monomer. MFs with weakly magnetic ($\mu^2_{max} = 1$) monomers and CTC crosslinking, shown in Figs.10a-10c, have largely flat R^{*2}_g profiles that differ at most 10%, regardless of filament length.

However, for MFs with strongly magnetic monomers ($\mu^2_{max} = 3$), shown in Figs.10d-10f, entropy cannot compete with dipole-dipole interactions. In the $\epsilon \leqslant 0.5$ central attraction region, for $N = 20$, R^{*2}_g suggests that MFs unravel into conformations characteristic for a head-to-tail dipole arrangement, even for $H < 1$. With increasing L, we see the joined action of *vdW* forces, and bent backbone conformations becoming more favorable and persistent. In Chapter 8, we rationalized how MFs with super-paramagnetic monomers can bend in an applied magnetic field to obtain a significant gain in entropy, and depending on filament length, do so without a loss in magnetic energy. Consequently, for $\epsilon \leqslant 0.5$, MFs with $N = 100$ at equilibrium have less than half the R^{*2}_g of MFs with $N = 20$. Furthermore, such bent conformations collapse due to central attraction. For $\epsilon \geqslant 1$, central attraction is strong enough to compete with dipole-dipole interactions. Therefore, for CTC crosslinking, the differences between the profiles for $\mu^2_{max} = 1$ and $\mu^2_{max} = 3$ are small and mostly constrained to the low field region, where the bending tendencies of MFs

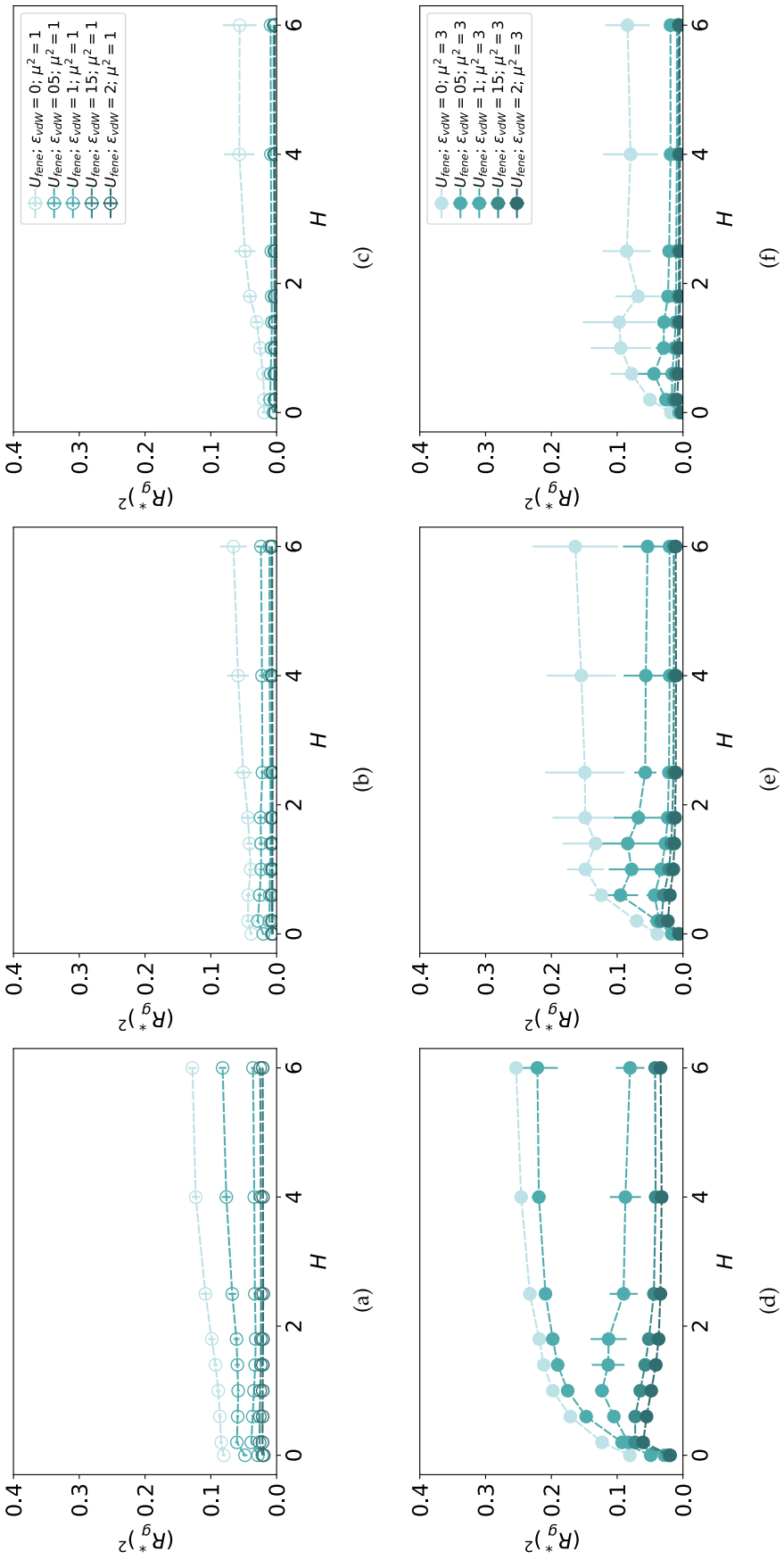

Figure 10: Normalized radius of gyration squared, $(R_g^*)^2$, plotted as a function of H. Each subplot is showing results for MFs with super-paramagnetic monomers and CTC crosslinking, with various strength of central attraction ϵ. In Subplots (a) - (c), $\mu^2_{max} = 1$ (hollow symbols); (d)-(f), $\mu^2_{max} = 3$ (filled symbols). In Subplots (a) and (d), N = 20; (b) and (e) are showing N = 50; (c) and (f) are showing N = 100. Color coding for different ϵ_{vdW} is explained in the legends. Error bars are calculated as the standard deviation of $(R_g^*)^2$ across 40 independent simulations.

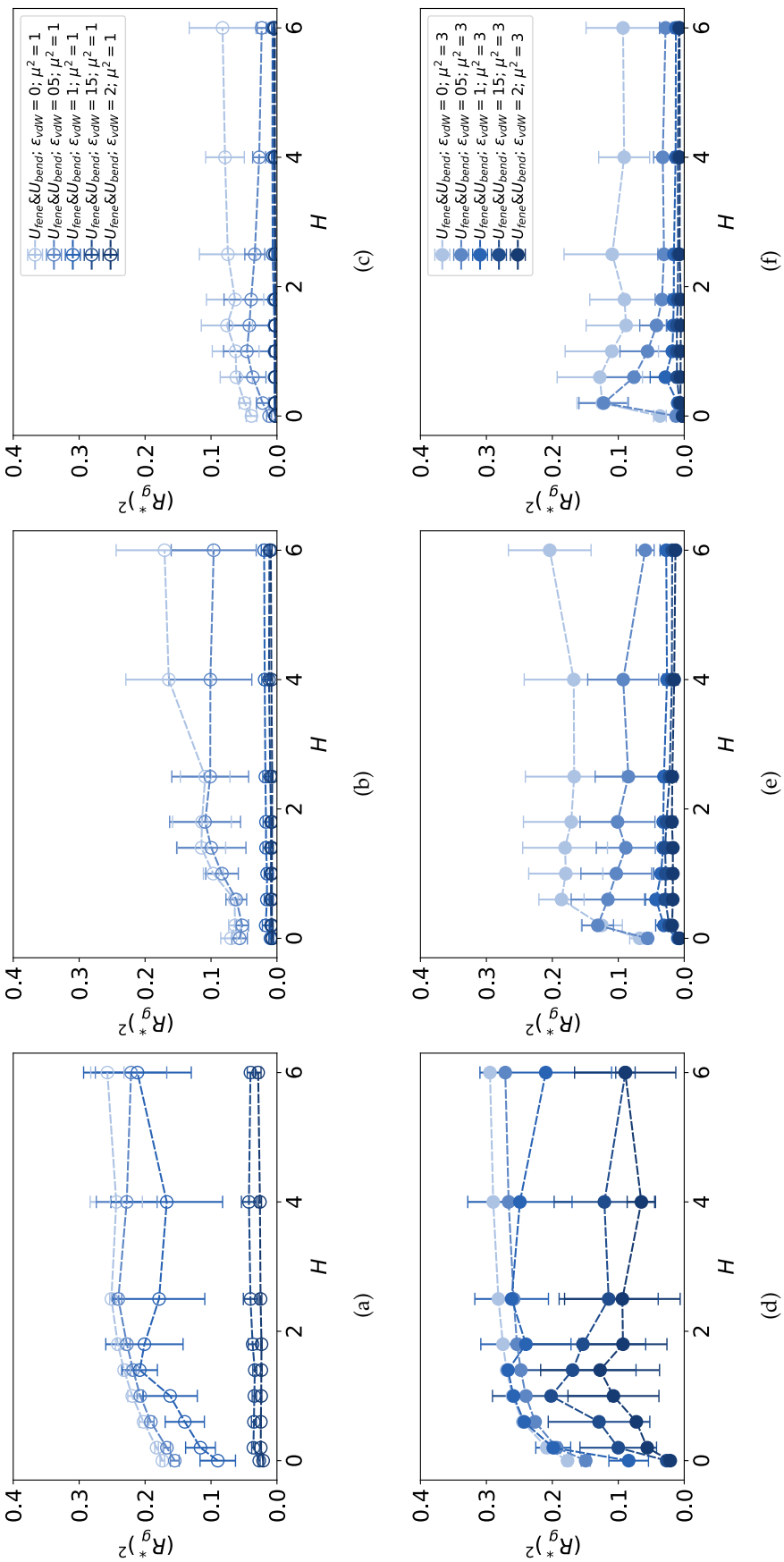

Figure 11: Normalized radius of gyration squared, $(R_g^*)^2$, plotted as a function of H. Each subplot is showing results for MFs with super-paramagnetic monomers and constrained crosslinking, with various strength of central attraction ϵ. In Subplots (a) - (c), $\mu^2_{max} = 1$ (hollow symbols); (d)-(f), $\mu^2_{max} = 3$ (filled symbols). In Subplots (a) and (d), N = 20; (b) and (e) are showing N = 50; (c) and (f) are showing N = 100. Color coding for different ϵ_{vdW} is explained in the legends. Error bars are calculated as the standard deviation of $(R_g^*)^2$ across 40 independent simulations.

with super-paramagnetic monomers are less pronounced. Furthermore, for $H \geqslant 2$, it can be seen that R_g^{*2} profiles are indistinguishable for a given L, regardless of the value of μ^2_{max}. We attribute the overall shape of these profiles to the local orientation of dipole moments along the field direction. For high values of H, MFs with $\epsilon \leqslant 0.5$ reach R_g^{*2} that is approximately 20% lower than that of a straight rod. Otherwise, they remain below 30% of the R_g^{*2} of a straight rod. It is interesting to note the particularly wide error bars in the Fig.10e. This is an energetically contentious region for MFs. Based on the deliberations in Chapter 8, for MFs with $N = 50$ magnetic monomers, we expect that there are bend backbone conformations that are magnetically favorable. At this length, MFs tend to spend significant time in such conformations and therefore exhibit a lot of variance in R_g^{*2}. Central attraction favors bent and collapsed conformations which is why increasing ϵ and/or L decreases the variance of R_g^{*2}.

Increase in inter-monomer correlations exacerbates the variance in R_g^{*2}, as can be seen for constrained crosslinking in Fig.11. Constrained crosslinking leads to a backbone that is overall stiffer and resists bending. A new player enters the competition, where on the one side, favoring elongation of the backbone along $\vec{H}$ are the head-to-tail dipole arrangement and resistance to bending induced by the constrained crosslinking, and on the other are the magnetically and entropically favorable bent backbone conformations and νdW interactions. Just like we saw for CTC crosslinking, R_g^{*2} profiles for MFs with constrained crosslinking and strongly magnetic monomers ($\mu^2_{max} = 3$) in the $H \leqslant 2$ region, shown in Fig.13d, for $\epsilon \geqslant 1.5$, correspond to completely clumped up filament conformations, with the noted exception for short $N = 20$ MFs. This outlines the importance of chemically stabilized colloids. For monomers that have a slight to moderate preference for their own species, the conformational landscape is diverse, judging by the variance in R_g^{*2}. Once again this is particularly pronounced for MFs with $N = 50$, shown in Fig.13b and 13e. Filaments with constrained crosslinking are, in line with Fig.4, more elongated than their counterparts with CTC crosslinking. Furthermore, they follow broadly similar trends as their CTC counterparts. Longer filaments favor collapsed conformations. Differences in R_g^{*2} based on μ^2_{max}, for a given L, are small and mostly constrained to the low field region. For constrained crosslinking, this is true even for weaker $\epsilon \leqslant 0.5$ central attraction. Additional inter-monomer correlations introduced by constrained crosslinking enhance the magnetic response of MFs and therefore, make R_g^{*2} corresponding to MFs with weakly magnetic monomers much closer to their counterparts with highly magnetic ones.

Looking at Figs. 12 and 13 we can see how the structural collapse of the filament backbone, facilitated by central attraction, affects the magnetic response of MFs, quantified by $\overline{m}^*$ as a function of H. Gen-

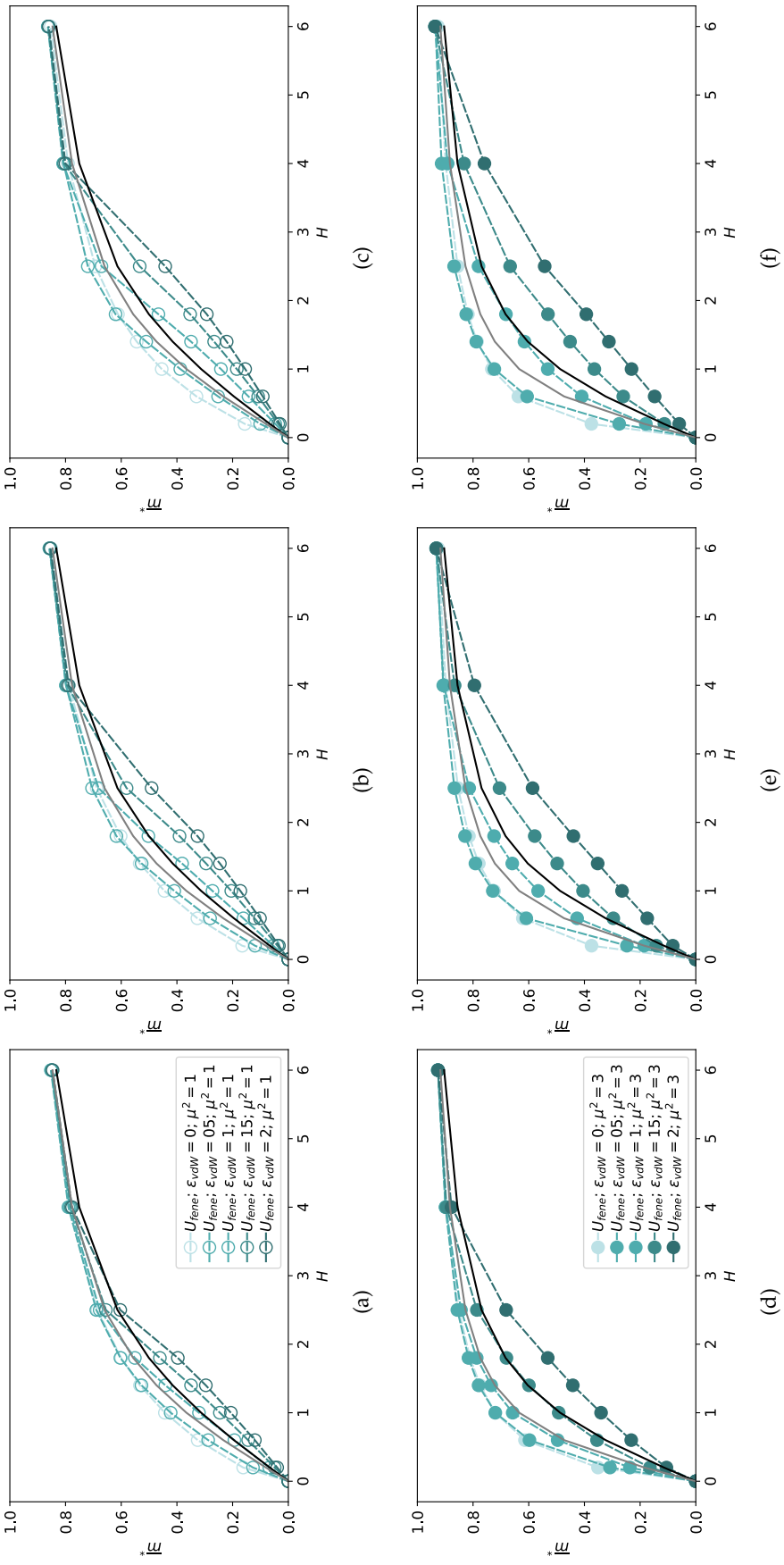

Figure 12: Normalized filament magnetization $\overline{m}^*$ as a function of the dimensionless magnetic field strength H. Each subplot is showing results for MFs with super-paramagnetic monomers and CTC crosslinking, with various strength of central attraction ϵ. In Subplots (a) - (c), $\mu^2_{max} = 1$ (hollow symbols); (d)-(f), $\mu^2_{max} = 3$ (filled symbols). In Subplots (a) and (d), N = 20; (b) and (e) are showing N = 50; (c) and (f) are showing N = 100. Color coding for different ϵ_{vdW} is explained in the legends. Langevin magnetization law from Eq. (4.6) and MMFT2 from Eq. (4.8) are shown in black and gray, respectively. Error bars are comparable to symbol size and are as such not shown.

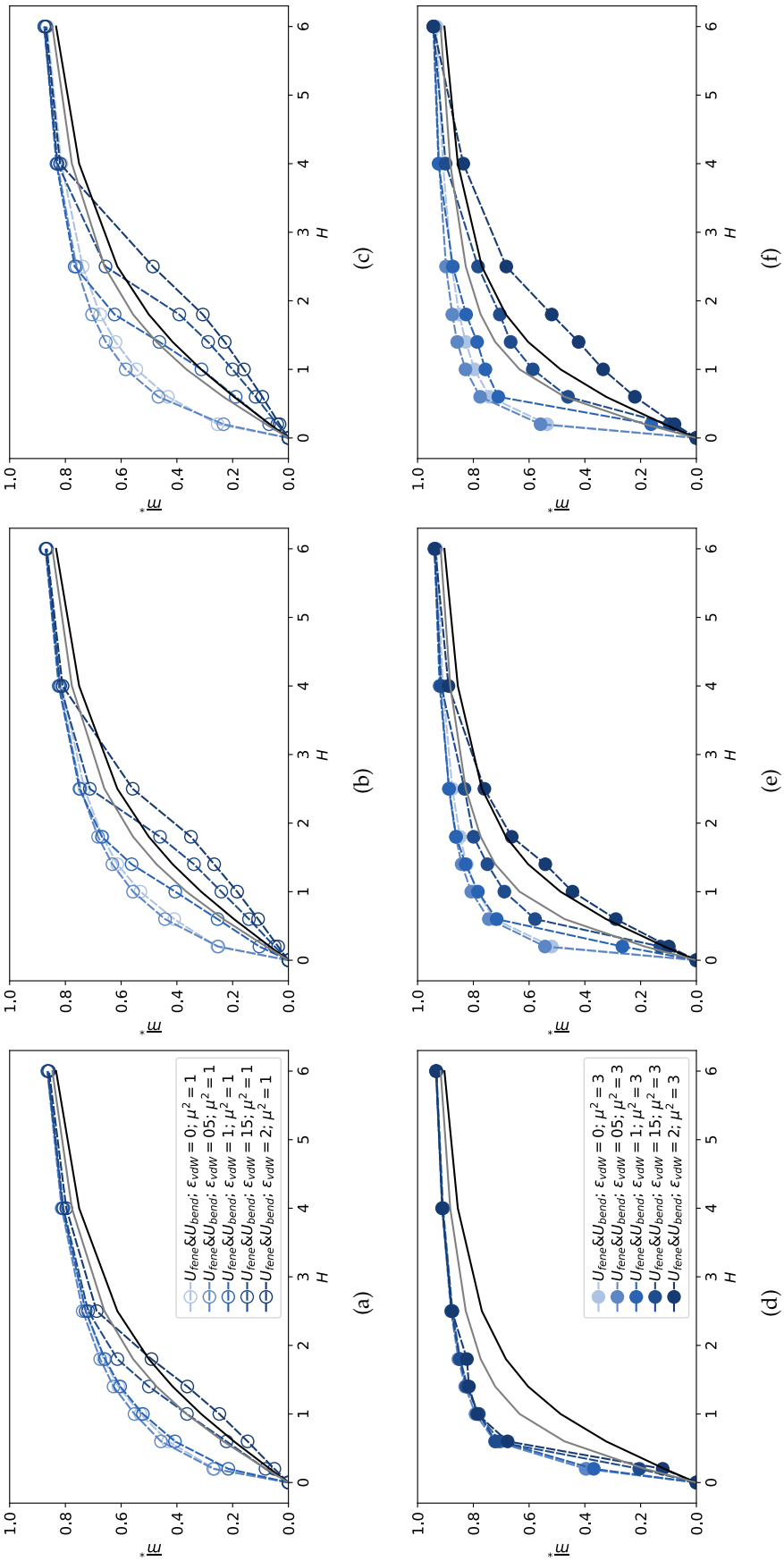

Figure 13: Normalized filament magnetization $\overline{m}^*$ as a function of the dimensionless magnetic field strength H. Each subplot is showing results for MFs with super-paramagnetic monomers and constrained crosslinking, with various strength of central attraction ϵ. In Subplots (a) - (c), $\mu^2_{max} = 1$ (hollow symbols); (d)-(f), $\mu^2_{max} = 3$ (filled symbols). In Subplots (a) and (d), N = 20; (b) and (e) are showing N = 50; (c) and (f) are showing N = 100. Color coding for different ϵ_{vdW} is explained in the legends. Langevin magnetization law from Eq. (4.6) and MMFT2 from Eq. (4.8) are shown in black and gray, respectively. Error bars are comparable to symbol size and are as such not shown.

erally, $\overline{m}^*$ should be independent of filament length, and profiles in Figs. 12 and 13 for MFs without central attraction reflect that. However, νdW forces scale with filament length and therefore make it interesting to consider $\overline{m}^*$ in that context also. Central attraction tends to push dipole moments in rather frustrating arrangements. This can be most clearly seen if we focus on MFs with CTC crosslinking and weakly magnetic monomers, whose magnetic response is similar to a semi-dilute ferrofluid. Central attraction decreases the magnetic response of MFs tremendously. They manage to reach predictions of MMFT2 only for relatively strong magnetic fields. Once again, we see why it is necessarily to avoid agglomeration of magnetic colloids. Moreover, we can see that the loss in magnetic response is worse for longer filaments. It can be seen in Fig.12d-12f, showing $\overline{m}^*$ for MFs with strongly magnetic monomers and CTC crosslinking, that having strongly magnetic monomers alleviates the issue somewhat. It should be clear by this point, that CTC crosslinking severely limits the magnetic response of MFs when νdW forces are present, where one can expect a system with a magnetic response to a semi-dilute ferrofluid at best. However, looking at Figs.13a-13f, one can see that MFs with constrained crosslinking fare much better. In fact, if νdW forces are not too strong ($\epsilon \leqslant 1$), $\overline{m}^*$ profiles corresponding to MFs with constrained crosslinking are representative of systems that are substantially more magneto-responsive than conventional magnetic fluids, even for rather long $N = 100$ filaments with weakly magnetic monomers. The additional inter-monomer correlations and resistance against bending complement and favor the head-to-tail dipole moment configuration. In effect, for strongly magnetic $\mu^2_{max} = 3$ monomers, constrained crosslinking suffices to almost completely offset the reduction in magnetic responsiveness of shorter MFs ($N = 20$) due to νdW forces, while for long chains $N = 100$ this is the case if $\epsilon \leqslant 1.5$.

Taking what we learned from Figs. 11 and 13 together, it is interesting to see how MFs with constrained crosslinking and superparamagnetic monomers manage to maintain an amicable magnetic response to external magnetic fields while persisting in very compact, collapsed structures. This implies that they manage to maintain an ordered internal structure and a favorable dipole moment configuration. We investigate whether our insinuations are justified by looking at the number of magnetically favorable neighboring monomers in a filament, as a function of H, for different crosslinking, μ^2_{max} and L. Neighbors of a monomer i are all monomers $j/neqi$ whose center is within the volume of a sphere of radius 1.3σ centered at the monomer i. Among the neighboring monomers, we count only the ones whose dipole moment is favorably orientated with respect to the dipole moment of the i-th monomer ($U_{dd} > 0$).

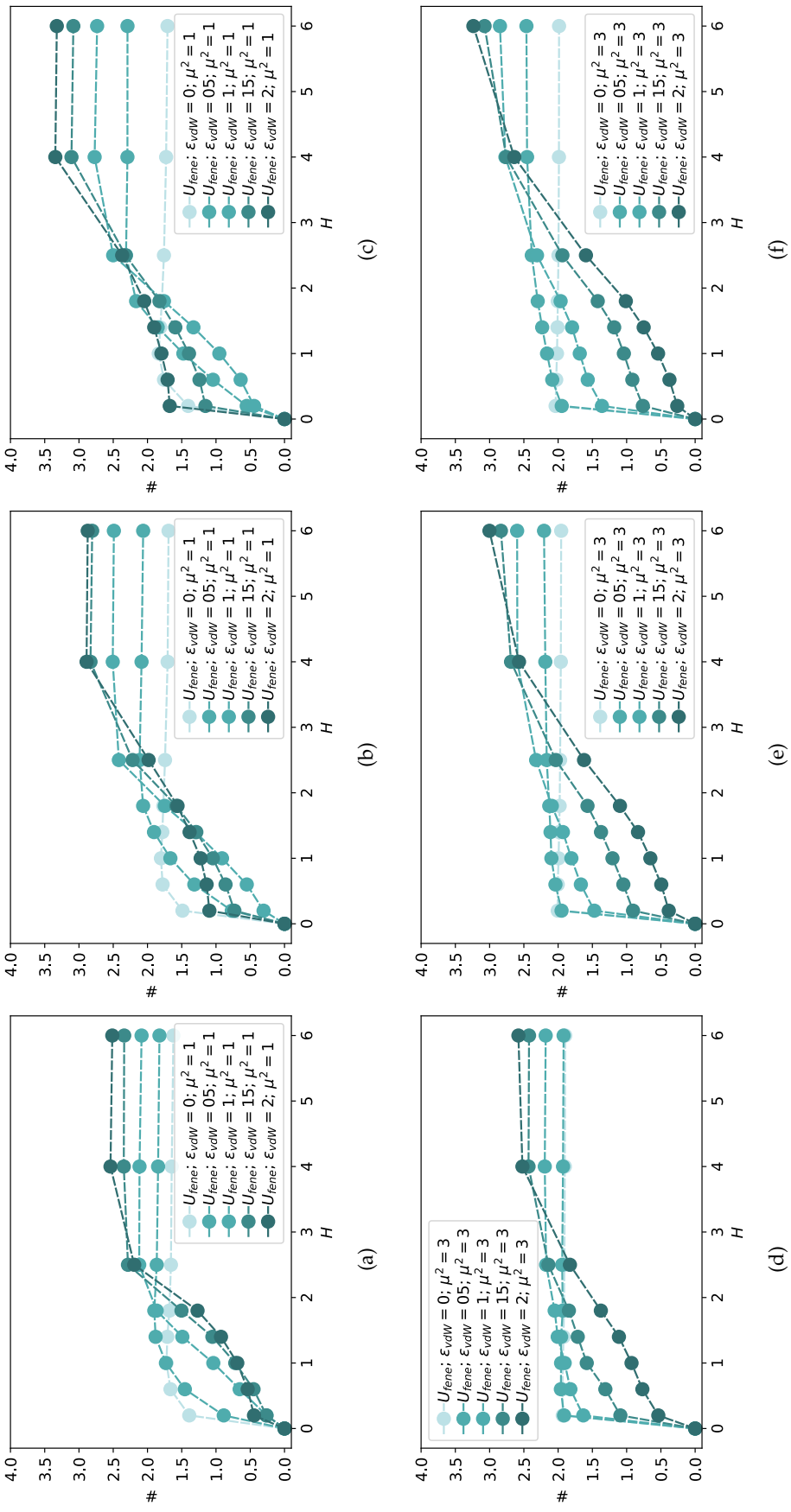

Figure 14: Number of magnetically favorable neighbors each monomer in a filament has versus magnetic field strength H. Each subplot is showing results for MFs with super-paramagnetic monomers and CTC crosslinking, with various strength of central attraction ϵ. In Subplots (a) - (c), $\mu^2_{max} = 1$ (hollow symbols); (d)-(f), $\mu^2_{max} = 3$ (filled symbols). In Subplots (a) and (d), N = 20; (b) and (e) are showing N = 50; (c) and (f) are showing N = 100. Color coding for different ϵ_{vdW} is explained in the legends.

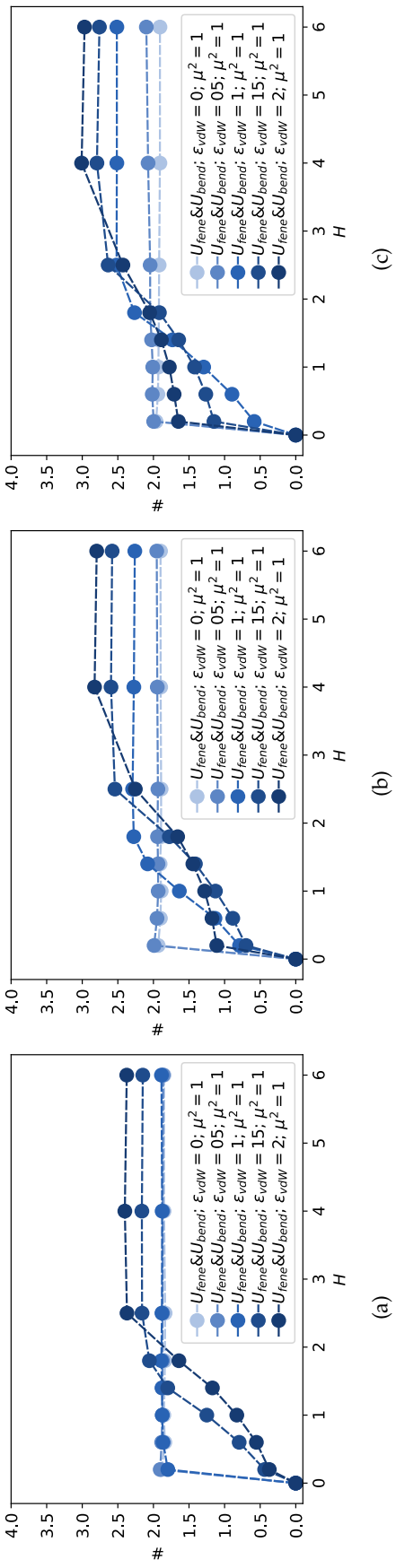

Figure 15: Number of magnetically favorable neighbors each monomer in a filament has versus magnetic field strength H. Each subplot is showing results for MFs with super-paramagnetic monomers and constrained crosslinking, with various strength of central attraction ϵ. In Subplots (a) - (c), $\mu^2_{max} = 1$ (hollow symbols); (d)-(f), $\mu^2_{max} = 3$ (filled symbols). In Subplots (a) and (d), N = 20; (b) and (e) are showing N = 50; (c) and (f) are showing N = 100. Color coding for different ϵ_{vdW} is explained in the legends.

Looking at Fig.14, we can see that without *v*d*W* forces, a weak magnetic field is enough for a filament to establish an overall head-to-tail dipole moment configuration. For MFs with weakly magnetic monomers $\mu^2_{max} = 1$, since the scale of dipole-dipole interactions and thermal fluctuations is the same, we see the number of magnetically favorable neighbors to be less than two, while for $\mu^2_{max} = 3$ we see exactly two magnetically favorable neighbors independent of filament crosslinking and L. Once *v*d*W* forces are present in the system we see that in the low H region, central attraction pushes dipole moments in a filament into magnetically unfavorable configurations. We also know from the analysis of Figs. 10 and 11 that these are compact configurations. With increasing H, Zeeman coupling helps counteract central attraction and dipole moments manage to arrange into ever more favorable configurations. The number of magnetically favorable neighbors is overall higher for larger ϵ, where we saw that increase in H does not increase R^{*2}_g. Here it is important to note that, non-collapsed filament conformations with a bent backbone are discriminated against by the distance criterion in Fig.14, because the legs of bent MFs rarely approach close enough to be counted as neighbors. Overall, MFs with CTC crosslinking manage to collapse into structures that, in the high H region, have a more favorable local arrangement of dipole moments compared to their counterparts with constrained crosslinking. This is understandable, as constrained crosslinking restricts how dipole moments can rearrange due to Zeeman coupling. Regardless, magnetic response of MFs with constrained crosslinking remains considerably higher. While the structure might be locally more frustrated, additional intermonomer correlations enforce an overall more organized structure where the configuration is dictated by the external magnetic field, as can be seen in Fig.16.

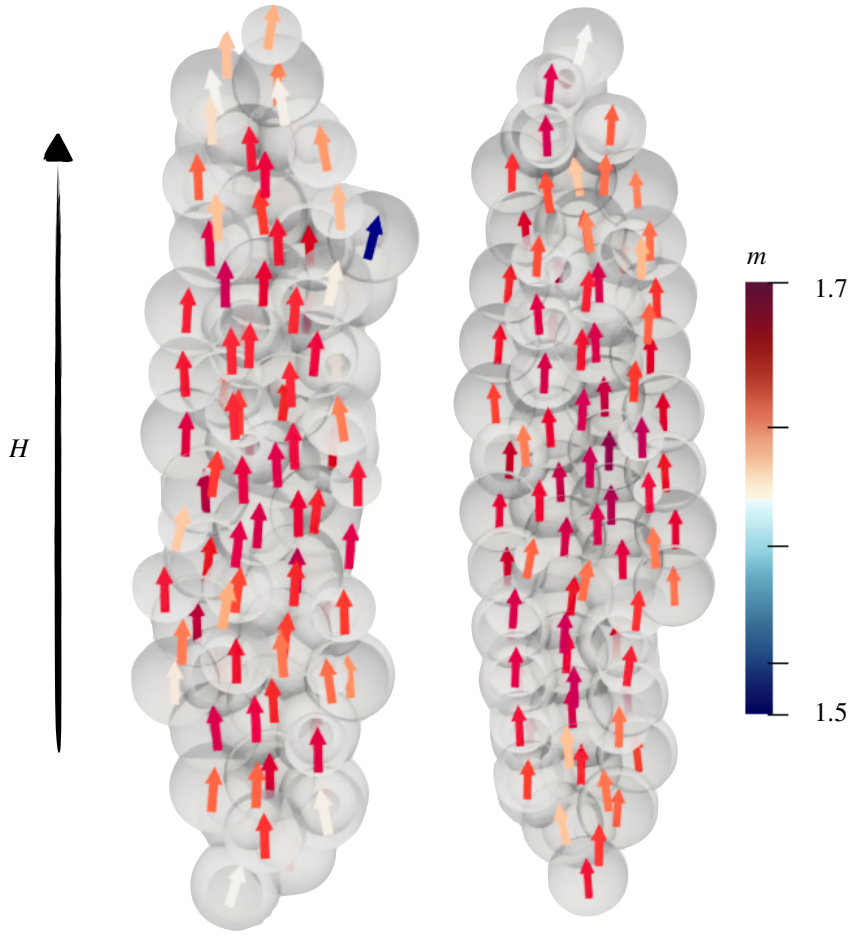

Figure 16: Simulation visualization of N = 50 MFs with CTC (left) and constrained crosslinking (right), with highly magnetic monomers ($\mu^2_{max} = 3$),in a strong magnetic field (H = 6), where monomers have a strong affinity toward agglomeration ($\epsilon = 2$). Color bar denotes the m span of monomers in the configuration shown.

Part III

DIRECTIONAL ASSEMBLY OF DNA NANOCHAMBERS AS A PLATFORM FOR SYNTHESIS OF MFS

In the following chapters we present:

- a theoretical investigation of the relationship between DNA Nanochamber reactivity and the morphologies arising from their self-assembly, presented in Chapter 11;
- a comparative analysis of nanopolymer designs with a focus on polymer-like structures made out of DNA Nanochambers, elucidating the impact of monomer shape, magnetic characteristics (if monomers are magnetic) and crosslinking on their equilibrium properties, presented in Chapter 12 and 13.

10 INTRODUCTION

In the Prologue, we emphasized that flexible, nanoscopic MFs with a finely controllable nanostructure, as this thesis is being written, have not yet been synthesized. We brought forward in the Prologue that in order to be able to do so, it is necessary to instill selective, anisotropic interactions between nanoobjects that are otherwise entirely isotropic. To this end, DNA nanoobjects have emerged as one of the most prominent candidates, due to their structural programmability and selectivity of sequence-specific interactions. [54, 88, 104, 106, 110, 120, 127, 139, 145, 169, 172, 178, 185, 189, 202, 207, 216] Assembly of DNA nanoobjects is a powerful way to form polymer-like morphologies – nanopolymers. [1, 4, 14, 22, 67, 101, 104–106, 167, 170, 188, 208, 212] Here, we present polymer-like systems, based on nanoobjects called divalent cuboid DNA nanochambers (DNC), that can also be used as templates for targeted assembly of nanoparticles. [104, 201] Piece by piece, we build the case that these nanoobjects and the nanopolymers they assemble into, are an excellent, finely tunable platform for construction of MFs, when functionalized with MNPs. A schematic depiction of DNC with complimentary bonding sites on their surface, forming nanopolymers, as well as incorporating MNPs in to DNC to form DNC-MNP complexes, resulting in MFs, are shown in Fig. 17. Resulting filaments are not conventional polymer-like structures but are distinct in both crosslinking and monomer shape. DNC-MNP complexes are connected to each other via multiple bonds holding their adjacent faces together. There is a complex interplay between bonding and monomer shape that affects mechanical and magnetic properties of MFs. Moreover, the MNPs used to form DNC-MNP complexes can be both ferro- and super-paramagnetic, depending on the magnetic material. The type of magnetic relaxation will have a profound impact on magnetic and mechanical properties of MFs, especially in conjunction with the interplay between monomer shape and inter-monomer connectivity.

It is worth noting that, while the author participated in the design and synthesis efforts that resulted in morphologies presented and broadly discussed here, experimental results are not presented. This work is focused solely on theoretical investigations. Therefore, except for presenting a phase diagram of the morphologies experimentally accessible with DNC, for further detail on the experimental aspects of these systems, the reader is encouraged to refer to Xiong et al. [201].

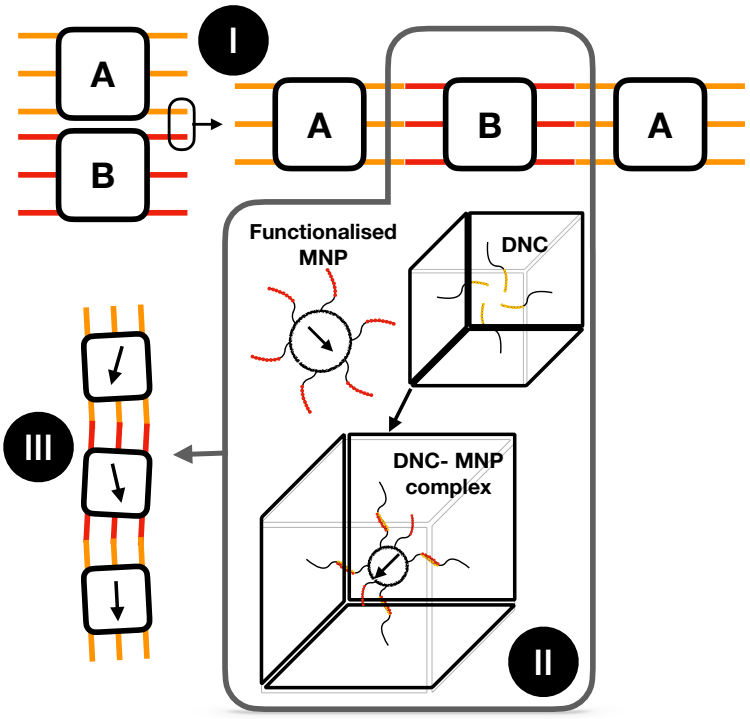

Figure 17: Schematic depiction relating assembly of DNC nanoobjects (top left) into a magnetic filament (bottom left); (I) Linkers between DNC type A and B hybridize to form longitudinal bonds. (II) Illustration of the growth of nanopolymers by connecting two complementary types of DNC, A and B. (III) DNC can form DNC-MNP complexes. Nanoparticles functionalized with single-stranded DNA (ssDNA) linkers can hybridize with complementary overhangs inside a DNC. (IV) Illustration of the growth of MFs by connecting complementary types DNC-MNP complexes.

10.1 MORPHOLOGICAL PHASE DIAGRAM OF DNA NANOCHAMBERS

In this section we present and discuss the morphological phase diagram of DNC in terms of bond design. Cuboid geometry facilitates the formation of ordered arrays. Here, we present the morphologies obtainable form DNC self-assembly, with a focus on polymerization. DNC nanoobjects are created by DNA origami technology. They consist of four double-layer DNA helix walls (outer layer: 12×12 double helices, inner layer: 10×10 double helices) that enclose a cavity ($25\text{nm} \times 25\text{nm} \times 28\text{nm}$). Furthermore, ssDNA linkers with sequence-based specificity are placed at a pair of opposite faces of the cubic surface (meaning front and back face), facilitating directional (lateral) inter-object interactions.

Specifically, a ssDNA linker is composed of an inert "spacer" and a so-called “sticky end” overhang, capable of hybridization with its

complement on another linker. These linkers can be extended from one of the two terminations of the DNA helices making out the walls of a DNC. Complementary linkers form inter-object bonds. In order to minimize undesired random bonding between linkers and to define a relative orientation between DNC nanoobjects, all sticky ends on a face of a DNC are distinct.[1]. Reactivity of DNC is determined by two parameters: the number of thymine nucleobases (poly-T) in the spacer of a linker, l, and the number of linkers per DNC, k. A DNC nanoobject with k linkers, each with spacer length l is denoted with M_l^k and schematically depicted in Fig. 18. Through adjustment of l and k, one can tune reactivity and control the assembly behavior.

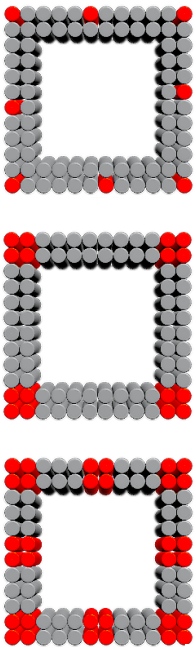

Figure 18: Top-view illustration of M_{16}^l , M_{32}^l , and M_{64}^l designs; red-colored helices are decorated with ssDNA

Looking at Fig. 19, let us examine the influence of k on the morphologies arising from DNC self-assembly. We sampled the morphological phase diagram along the k dimension using three DNC designs; M_{16}^l stands for a DNC design with eight linkers, positioned separately on the corners of the front and back faces (one linker per corner), while the remaining eight linkers are positioned in the middle of each edge (one linker per edge); M_{32}^l stands for a DNC design where four linkers are placed at each corner of the front and back faces of a DNC; M_{64}^l stands for a DNC design with the same linker arrangement as for M_{16}^l design, but with four linkers at each position. The number of monomers in resulting nanopolymers increases with k, as it is most easily seen for $l = 20$. Overall hybridization energy is proportional to k, resulting in longer nanopolymers for larger k. Furthermore, increased number of linkers also contributes to a higher binding probability of DNC with larger k, due to increased probability that linkers with run into each other while exploring the phase space.

The influence of l on the morphologies arising from DNC self-assembly can be seen by fixing k and varying the length of poly-T spacers in a range of 10 to 40.[2] The effects of l, apparent in Fig. 19, can be rationalized with two entropic factors. With increasing linker length, conformational entropy increases. Furthermore, the effective cross-section for inter-object binding increases with l. Together, these effects contribute to DNC reactivity, resulting in a higher probability of polymerization with larger l. However, beyond the longitudinal growth of DNC, we also observed lateral growth in to ordered bundles of nanopolymers, most frequently occurring for DNC M_{64}^{40}, as depicted in Fig. 19. The probability of encountering such bundles drops precipitously for shorter linkers. For the purposes of this thesis, however, such morphologies are not relevant and as such will not be further explored.

1 We dubbed such encoding as "differentiated poly-chromatic bonds, as can be found in Lin et al. [104] and Xiong et al. [201]

2 The number of thymine nucleobases corresponds to an effective spacer length. However, the actual length is a complex function of many experimental factors. Therefore, values of l are not to be taken literally.

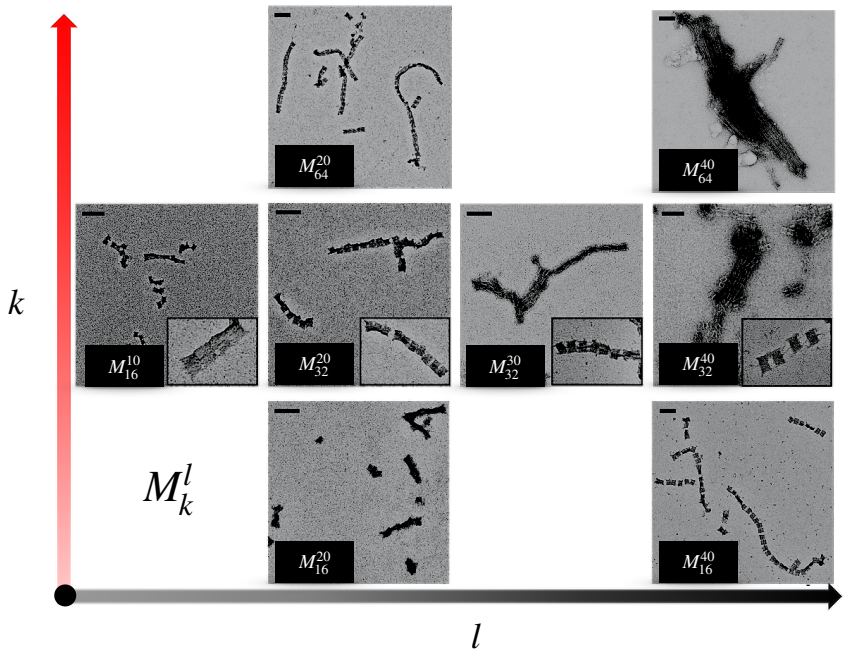

Figure 19: Morphological phase diagram for M_k^l DNC self-assembly, as a function of k and l. Images obtained by negatively stained transmission electron microscopy (TEM).

10.2 RASPBERRY MODEL OF COMPLEX SHAPES

In Section 5.3, we brought forth that in MD simulations, a typical approach to address the excluded volume in an ensemble of spherical monomers is to use the WCA pair potential given by Eq. (5.5). For non-spherical monomers however, or spherical monomers whose surface properties need to be considered, there are two general ways of modelling steric interactions. One could solve an algebraic system of equations on each MD integration step to check for the overlap of complex shapes; Alternatively, one can construct complex shapes out of rigid arrangements of WCA spheres. Here, we use the latter method which, albeit less accurate, is very flexible, can be applied to arbitrary shapes and is computationally efficient. Realizations of monomers using this method are usually called (affectionately and literally) raspberries.[107] Therefore, we refer to simulation representations of DNC as raspberry cubes. The raspberry model was used successfully for investigations of magnetic and charged cubes.[43, 44, 142]

Positions and radii for the WCA spheres that make out a raspberry are calculated using the superball model, developed by Donaldson, Linse, and Kantorovich [44]. Here we roughly outline how does one construct a raspberry cube in the framework of the superball model.

The surface of a raspberry is outlined with a (x, y, z) set of points in the center-of-mass reference frame by the superball equation:

$$f(\rho) = \left|\frac{x}{r}\right|^{2\rho} + \left|\frac{y}{r}\right|^{2\rho} + \left|\frac{z}{r}\right|^{2\rho} = 1, \tag{10.1}$$

where ρ is the shape parameter. At $\lim_{\rho\to\infty} f(\rho)$, Eq. (10.1) is describing a cube with perfectly sharp edges. With $\rho = 1$, Eq. (10.1) describes a sphere with radius r centered at $r = 0$. To approximate a surface of the true geometry, given by Eq. (10.1), using WCA spheres, one can consider two sets of characteristic positions within the true geometry. Specifically, one can take cross-sections at the vertex and the mid-edge position of the true geometry, calculating the ρ dependent radius of curvature at both. From there radii of WCA spheres can be determined, by parametrizing the equations describing the cross-sections for a given ρ, in the form $\mathbb{X}(q, \rho), \mathbb{Y}(q, \rho)$. The radius of curvature is determined using:

$$\mathcal{R} = \frac{(\mathbb{X}'^2 - \mathbb{Y}'^2)^{3/2}}{|\mathbb{X}'\mathbb{Y}'' - \mathbb{Y}'\mathbb{X}''|}, \tag{10.2}$$

where the primes denote derivatives with respect to q. The magnitude of the position vector for each WCA sphere is the displacement from the true surface, reduced by the appropriate radius of curvature. Consequently, the WCA spheres and the analytical surface of a superball coincide at this position. For computational efficiency, all WCA spheres in a raspberry except for the center-of-mass particle are subsequently converted to virtual sites (see. Section 2.3)

10.3 IMPLEMENTATION NOTES AND UNITS

Here, we use raspberry cubes introduced in Section 10.2, or spherical monomers realized like standard WCA spheres. We refrain from using explicit representations of ssDNA, such as the freely jointed chain representation, used in works like Vargas-Lara, Starr, and Douglas [182], or tools for simulating ssDNA, such as in oxDNA.[123] Such models are rather costly in terms of computational resources, and unnecessary to qualitatively reproduce the experimental findings.

In thermal annealing simulations, presented in Chapter 11, we represent the ssDNA linkers as attractive LJ spheres (Eq. (3.12)) connected to the raspberry surface via FENE bonds (Eq. (5.1)), in arrangements as shown in Fig. 18. Attractive LJ spheres are realized with the

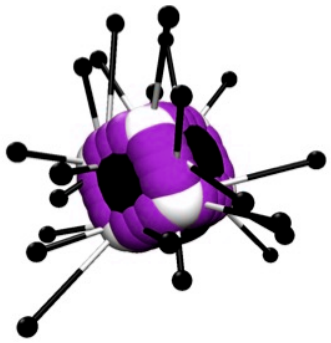

Figure 20: Raspberry model representation of M_{32}^{l} DNC (linkers shown as small black spheres). Central reference particle is shown as large black sphere. Virtual sites outlining the DNC vertices shown in purple. Virtual sites populating the DNC edges shown in white.

following parameters: $\sigma_{sticky} = 0.05$, $\epsilon = 10$ and $r_{cut} = 2.5\sigma_{sticky}$, where σ_{sticky} is the diameter of the attractive LJ sphere. FENE bonds connecting them to the raspberry surface are realized with $r_0 = \alpha\sigma$, where $\alpha \in \{0.6, 0.8, 0, 9, 1.0\}$ and σ is raspberry diameter. The parameter α corresponds to l for given k arrangement of an M_k^l DNC. Maximal extension of each FENE bond, r_f, was set to be three times the equilibrium linker length r_0. In Fig. 20, one can find a visualization of a raspberry cube employed in this study. When simulating nanopolymers in Chapter 12 and 13, monomers are directly linked with FENE bonds in arrangements as shown in Fig. 18, with the parameters as stated above. The diameter of the center-of-mass particle of a raspberry cube is set to $\sigma = 1$. With this choice, according to the superball model, for shape parameter $q = 2$, corner virtual sites have $\sigma = 0.41$ while vertex virtual sites have $\sigma = 0.49$. All particles outlining the raspberry surface have the excluded volume interaction strength $\epsilon = 1$.

Computational models used for the comparative study in Chapter 12 and 13 are depicted in Fig. 21. These models are designed to en-

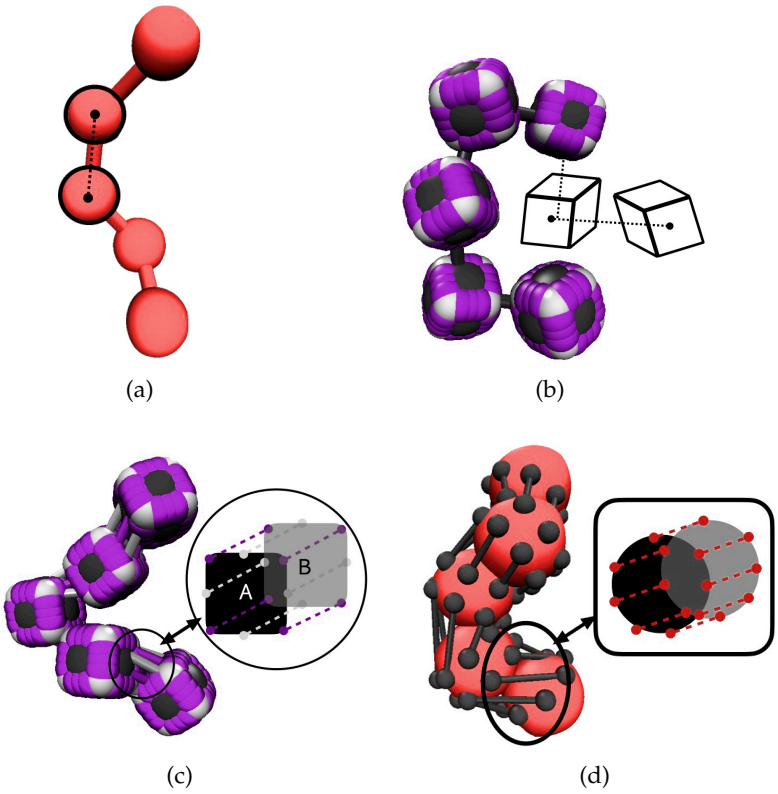

Figure 21: (a) CTC crosslinking for spherical monomers; (b) CTC crosslinking for cubic monomers; (c) FTF crosslinking of cubic monomers; (d) FTF crosslinking of spherical monomers.

compass a range of nanopolymeric systems with different monomer shape and crosslinking. Figs. 21a and 21b show representations of polymer-like systems, with spherical and cubic monomer shape, respectively, with center-to-center (CTC) crosslinking. Only the translational degrees of freedom of monomers are restricted. Combination of CTC crosslinking and spherical monomer shape corresponds to a self-avoiding walk.[148] DNC nanopolymer model shown in Fig. 21c captures the distinctive cubic monomer shape using raspberry cubes, together with the specific inter-object connectivity of DNC, we refer to here as face-to-face crosslinking (FTF). The arrangement of FENE bonds corresponds to M^{l}_{16} DNC, as depicted in Fig. 18. By varying the equilibrium linker length r_0, we vary the equilibrium distance between monomers in a nanopolymer. This corresponds to varying the l of M^{l}_{k} DNC as presented in the introduction. One can account for the added rigidity of M^{l}_{64} nanopolymers, compared to their M^{l}_{16} counterparts, by increasing the FENE potential prefactor K_f. Therefore, from the point of view of our coarse-grained model, the results presented in this section could be representative of both M^{l}_{16} and M^{l}_{64} DNC nanopolymers. Model depicted in Fig. 21d, is designed to reproduce the characteristics of FTF crosslinking, in conjunction with spherical monomers. We achieve this by creating two crowns of virtual sites on

opposite sides of spherical monomers, that serve as anchoring points for FENE bonds. Positions of virtual sites that make the crowns are determined by finding the cross-section of a sphere with diameter σ and a plane, whose normal vector is pointing in the direction along which the backbone is initially spanning. We are looking for circles of points that solve this problem, whose centers are located at $r_i + \sigma/4$ and $r_i - \sigma/4$, respectively, where r_i is the position of the center of the i-th monomer. We create eight equidistant virtual sites on each of the resulting circles on the surface of the spherical monomer. For each pair of monomers, adjacent virtual sites are linked by FENE bonds. Important to note is that FTF crosslinking leads to a stiffer polymer backbone as it couples not only the translational but also rotational degrees of freedom of monomers, in analogy to constrained crosslinking introduced in Section 5.1. In other words, monomers can still rotate, but cannot do so freely with respect to their neighbors along the backbone.

To be able to compare nanopolymer designs with different monomer shape and crosslinking with different linker number, we need to tune the overall pair-interaction potential. Interaction potential between a pair of bonded monomers is determined by the interplay between the steric interaction and FENE bonds between them. We match the parameters so that the magnitude of the interactions between nearest neighbors in different crosslinking scenarios is nearly the same for a given value of r_0 in Eq. (5.1), regardless of monomer shape. This is achieved by adjusting monomer diameter σ, the strength of the excluded volume interaction ϵ in Eq. (5.5) and the FENE potential prefactor K_f. Based on interaction potential matching, for spherical monomers we set: $\sigma = 0.91$ and $\epsilon = 100$. Furthermore, FENE bonds in CTC crosslinking should be nine times as rigid as the ones in FTF crosslinking. Therefore, for FTF crosslinking, $K_f = 10$, while for CTC crosslinking $K_f = 90$. The reduced characteristic mass of all massive particles in our simulations is taken to be $m = 1$. This value does not affect the results, rather the speed of the convergence to equilibrium. However, the tensor of inertia of the center-of-mass particle in each raspberry cube must be set to represent the fact that it carries a shell of virtual sites that make out the cubic shape. The overall energy scale in our simulations is determined by the choice of the reduced temperature $k_B T = 1$. Finally, for MFs, we consider reduced saturated magnetic moment of $\mu^2_{max} = 3$, for a range of reduced external magnetic fields $H \leqslant 6$. Given a choice of a particular magnetic nanoparticle, such as using magnetite nanoparticles coated with a thin layer of stabilizing agent (*i.e.*, oleic acid coating, $2nm$ thick), σ corresponds (not uniquely) to a colloid with a magnetic core of $15nm$ with a dipole moment of $8.5 \times 10^{-19} Am^2$. This also means that the maximum of the applied magnetic field range we explored represents moderate fields of only 0.072 T.

11

THERMAL ANNEALING OF DNC NANOOBJECTS

In this chapter we use MD simulations to qualitatively reproduce the assembly behavior of DNC. The focus here is directional assembly of DNC into nanopolymers. Even though polymerization is the dominant assembly mode[1], additional bonding modes arise with increasing k and l, that result in bundles of nanopolymers, as shown in for DNC M_{64}^{40} in Fig. 19. We propose that the unique binding characteristics of DNC are the main factor responsible for the formation of bundles with a 3D lattice structure.

We simulate self-assembly between two complementary types of DNC, akin to $-A-B-A-$ assembly schematically depicted in Fig. 17, by making attractive LJ spheres on DNC A attractive exclusively to the ones on DNC B. This is very much a patchy-particle inspired representation of a DNC, where we coarse-grain the ssDNA linkers to lose all specificity except from linker length and overall interaction strength. Furthermore, the relative orientation between DNC is not restricted as opposed to the experimental system. Inside a fully periodic simulation box ($12\sigma \times 12\sigma \times 12\sigma$), we place 40 randomly placed DNC. We firstly make sure that system settles into a configuration, where there are no overlapping particles. We simulate thermal annealing by incrementally decreasing the thermostat temperature from $T = 1$ to $T = 0$ in 10 steps separated by 5000 timesteps. Simultaneously, we run a collision detection procedure. Once the attractive LJ spheres touch, they remain permanently bonded. Furthermore, they become inert with respect to the rest of the system in all ways except from the excluded volume interaction. We run twelve parallel simulations for each M_k^l design.

Visual inspection of Fig. 22 qualitatively confirms the trends seen in Fig. 19: higher values of k and l lead to longer structures and more branching that could lead to bundling. We analyze the clusters formed during thermal annealing of raspberry cubes. The topology of clusters is characterized by the coordination number $N_{neighbor}$, namely the number of close neighbors to which each DNC binds. Note that for linear structures, $N_{neighbor}$ is between 1 and 2; a value above 2 suggests bundling or branching. In Fig. 22b and 22c, we compare the probability of finding a DNC bound with $N_{neighbor}$ neighboring DNC, and the number average of $N_{neighbor}$, $\bar{N}$. Looking at Fig. 22c, for M_{16}^{40} DNC, $\bar{N} = 1.71$ corresponds to linear polymerization; M_{32}^{40}, $\bar{N} = 2.28$ suggests partial branching or bundling of chains; M_{64}^{40}, $\bar{N} = 2.61$ strongly indicates a more significant crosslinking be-

1 The ssDNA linkers have been designed to facilitate this mode of assembly

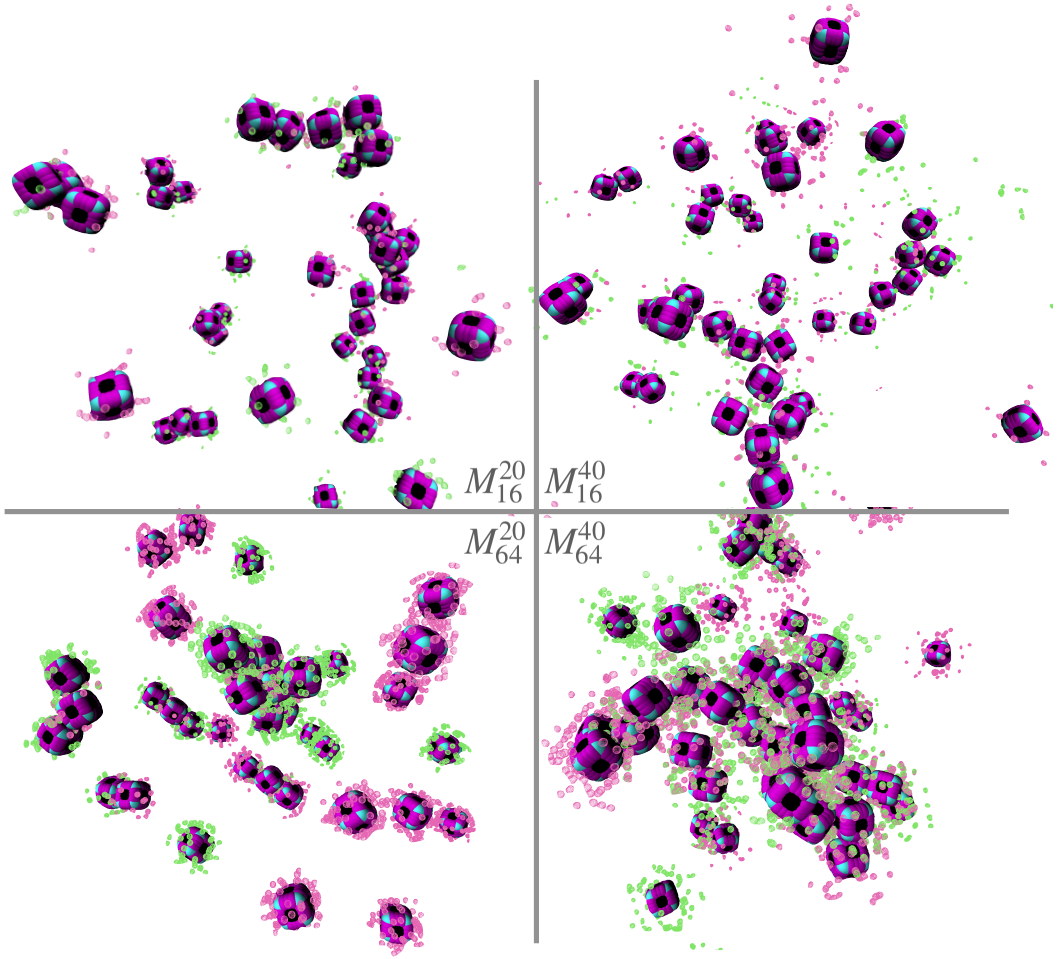

(a)

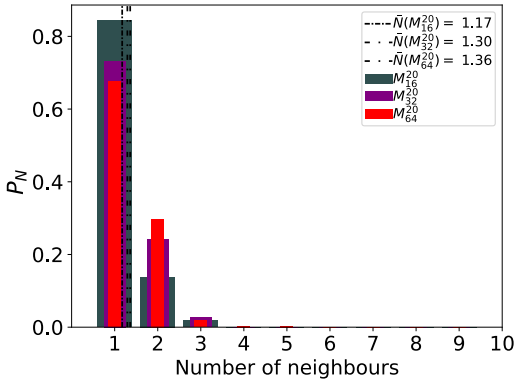

(b)

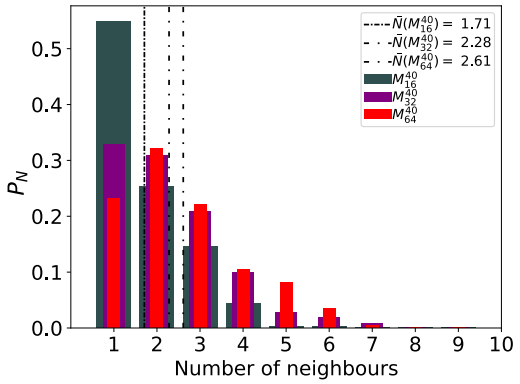

(c)

Figure 22: Showing the probability of finding a DNC bound with $N_{neighbor}$ neighboring DNC, for the final configurations of simulated annealing of DNC. Results for raspberry cubes that correspond to M_{16}^{l}, M_{32}^{l} and M_{64}^{l} DNC, are given in green, purple and red, respectively, where in (b) $l = 20$ ($r_0 = 0.6\sigma$); (c) $l = 40$ ($r_0 = \sigma$). For $l = 20$ we use distance criterion, dcut = 2.13; For $l = 40$ we use distance criterion 2.42. Black dotted-dashed lines represent mean values for each equilibrium patchy linker length, respectively. Instances of non-bonded DNC are filtered out from the data.

tween DNC leading to nanopolymer bundles. Furthermore, comparing models based on linker length, across Fig. 22b and 22c respectively, we see that for M_{16}^{l}, increasing l leads to longer nanopolymers, without significant bundling. However, for M_{32}^{l} and M_{64}^{l}, we see that longer linkers also contribute to bonding modes that result in nanopolymer bundles.

12

DNC NANOPOLYMERS

For the comparative analysis of the polymeric properties of various nanopolymer designs, we create chains of L monomers, $L \in [2, 50]$ and place each of them in a separate non-periodic ($500\sigma \times 500\sigma \times 500\sigma$) simulation box, initially fully straight and stretched (length of all bonds is their equilibrium length $r_0 = \alpha\sigma$), with the backbone orientated randomly. We run 40 parallel, model/length specific simulations, for different values of r_0 at constant $T = 1$. We firstly make sure that system relaxes into an equilibrium configuration, by running an integration cycle for 2.1×10^6 integration steps. After the relaxation cycle, we start recording simulation snapshots every 7000 integrations, to minimize correlations between observed conformations. The total length of the measurement cycle is 1.05×10^7 integrations.

In Fig. 23, we scrutinize how monomer shape, crosslinking and r_0, manifest themselves in R^*_{ee}, given by Eq. (7.1) and plotted as a function of H. The value of d_{avg} in Eq. (7.1) is calculated separately for each crosslinking approach, monomer shape, L and r_0. Our aim here is to underline DNC features, that is, cubic monomer shape and specific inter-monomer connectivity, and how they lead to unique properties. Independently of value of r_0, presented as increasing from Fig. 23a to 23b, the most rigid nanoscopic polymer model is the one with FTF crosslinking with cubic monomers, whereas conformations with most coiling are assumed by the nanopolymers with spherical monomers and CTC crosslinking. Differences between models are exacerbated for smaller r_0.

It is interesting to underline that the shape of the monomers manifests itself only for relatively large values of L. Thus, below $L = 15$ the behavior of the R^*_{ee} is defined exclusively by the type of crosslinking. The way R^*_{ee} grows with L depends predominantly on monomer shape. The R^*_{ee} gradient decreases, with increasing L, especially for nanopolymers with spherical monomers. To quantify the differences between the growth rates, for each of the models, we fit the simulation data with a power-law, bL^a, starting from $L \geqslant 15$. These fits are shown in Fig. 23 with solid lines. The fit parameters are collected in Table 1. Nanopolymers with spherical monomers and CTC crosslinking exhibit the scaling of a self-avoiding walk. The situation changes drastically for MFs with FTF crosslinking and spherical monomers: the exponent a decreases with α and never corresponds to a self-avoiding walk. For cubic monomers, R^*_{ee} grows almost linearly with L independently of the type of crosslinking. The latter affects the prefactor b. Nanopolymers with FTF crosslinking are in general straighter

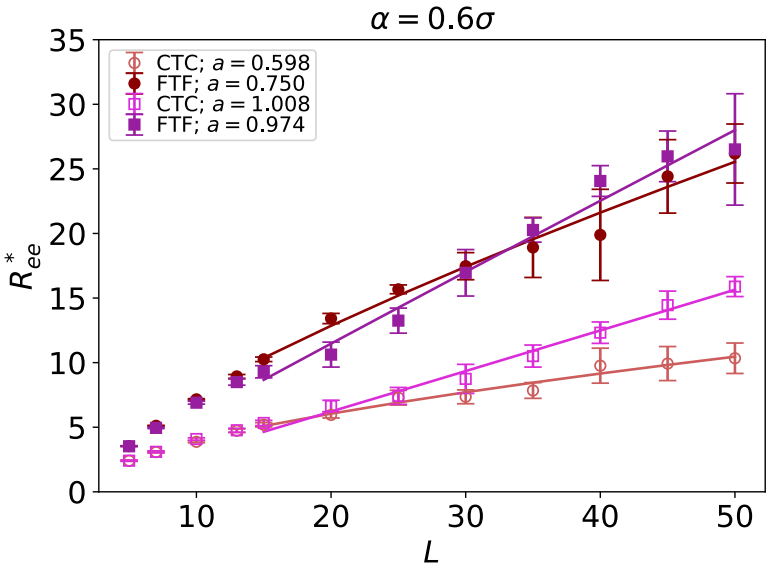

(a)

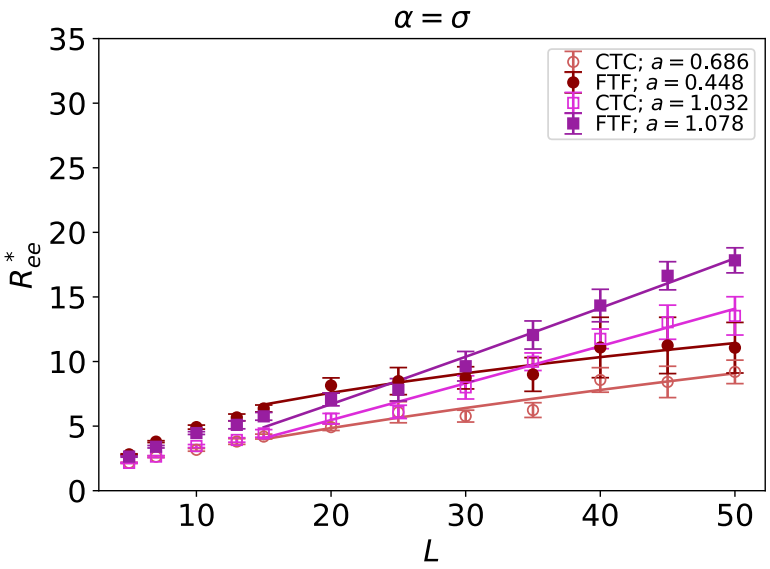

(b)

Figure 23: Normalized end-to-end distance, R^*_{ee} as a function of monomer number L. (a) and (b) show results for different $r_0 = \alpha\sigma$, where $\alpha \in \{0.6, 1\}$, and σ is particle size. Datapoints for nanopolymers with spherical monomers are represented with spherical symbols (red); Datapoints for nanopolymers with cubic monomers are represented with square symbols (purple). Filled symbols, shown in a darker color shade, represent models with FTF crosslinking; non-filed symbols, shown in a lighter color shade, are for CTC crosslinking. Error bars are calculated as the standard deviation of R^*_{ee} across 40 independent simulations. Solid lines represent the power-law fits, explained in the text. Values of the fit exponents are shown in the legend. All fit parameters are shown in Table 1.

Table 1: Parameters obtained by fitting R^*_{ee} with a power law $y(L) = bL^a$ for different value of r_0.

Linker length	Shape	Fit, CTC	Fit, FTF
$r_0 = 0.6\sigma$	○	a=0.598, b=1.008	a=0.750, b=1.361
	□	a=1.008, b=0.303	a=0.974, b=0.620
$r_0 = 0.8\sigma$	○	a=0.665, b=0.740	a=0.523, b=2.228
	□	a=1.071, b=0.230	a=1.018, b=0.412
$r_0 = 0.9\sigma$	○	a=0.676, b=0.676	a=0.485, b=2.051
	□	a=1.052, b=0.237	a=1.076, b=0.295
$r_0 = \sigma$	○	a=0.686, b=0.622	a=0.448, b=1.981
	□	a=1.032, b=0.248	a=1.078, b=0.265

than their CTC counterparts. The closest to unity exponent a can be found for a nanopolymer with cubic monomers and CTC crosslinking, with r_0 corresponding to monomer close contact.

For nanopolymers with CTC crosslinking, increase of α leads to an expected increase of the scaling exponent a, regardless of monomer shape. The growth of the equilibrium inter-particle distance can be regarded as an increase of an effective monomer diameter or swelling of the nanopolymers. However, the shape of monomers manifests itself in a nontrivial way when their rotational degrees of freedom are coupled to the backbone. Nanopolymers with FTF crosslinking have difficulties to coil for short bonds ($\alpha = 0.6$). An increase of α leads to coiling, where for filaments with spherical monomers, conformations become more compact, and we see a decrease in a. However, there is an additional, purely steric coupling between the relative orientation of cubic monomers. In fact, relative orientation coupling between cubic monomers is mostly steric, which is why a is so similar for nanopolymers with cubic monomers, regardless of crosslinking. These points are also depicted by in Fig. 24, which is showing representative simulation snapshots of the conformations our models take, across the combinations of monomer shape, crosslinking approach and r_0 we explored.

One can conclude that shape effects, albeit less pronounced compared to crosslinking effects, are still present. We attribute this to the fact that at $r_0 = 0.6\sigma$, where σ is monomer size, crosslinking ensures that monomers are essentially touching. Most intuitive way to imagine monomer shape affecting R^*_{ee}, is the way it restricts monomers sliding past one another or rolling over each other's surface. Spherical monomers can easily do both of those things. Cubic monomers instead are limited in either of the motions when crosslinked. If, however, crosslinking is restrictive enough to minimize such behavior regardless the monomer shape, R^*_{ee} profiles are grouping, like we see

in Fig. 23a. This explanation is corroborated by persistence length L_p values, shown in Table 2, which is to be read together with Fig. 24, where we show representative simulation snapshots corresponding to the L_p entries in Table 2. We extract L_p from the decay of the autocorrelation function:

$$C(n) =< cos\theta_{i,i+n} >=< \vec{a}_i \cdot \vec{a}_{i+n} >\approx \exp\left(-\frac{n d_{avg}}{L_p}\right), \quad (12.1)$$

between vectors $\vec{a}_i$ connecting each pair i of neighboring monomers along the backbone, separated by n monomers. We see that models with FTF crosslinking can have several times higher L_p than their counterparts with CTC crosslinking. We achieve the highest difference between CTC crosslinked nanopolymers with spherical monomers, and FTF crosslinked nanopolymers with cubic monomers.

Linker length	Shape	L_p, CTC	L_p, FTF
$r_0 = 0.6\sigma$	○	1.08	8.41
	□	1.37	8.73
$r_0 = \sigma$	○	1.06	2.09
	□	1.31	2.24

Table 2: Persistence length L_p of nanopolymers, with different equilibrium length of linkers and monomer shape, shown in Fig.24, in units of σ. Fits performed on datasets for nanopolymer models with $L = 50$.

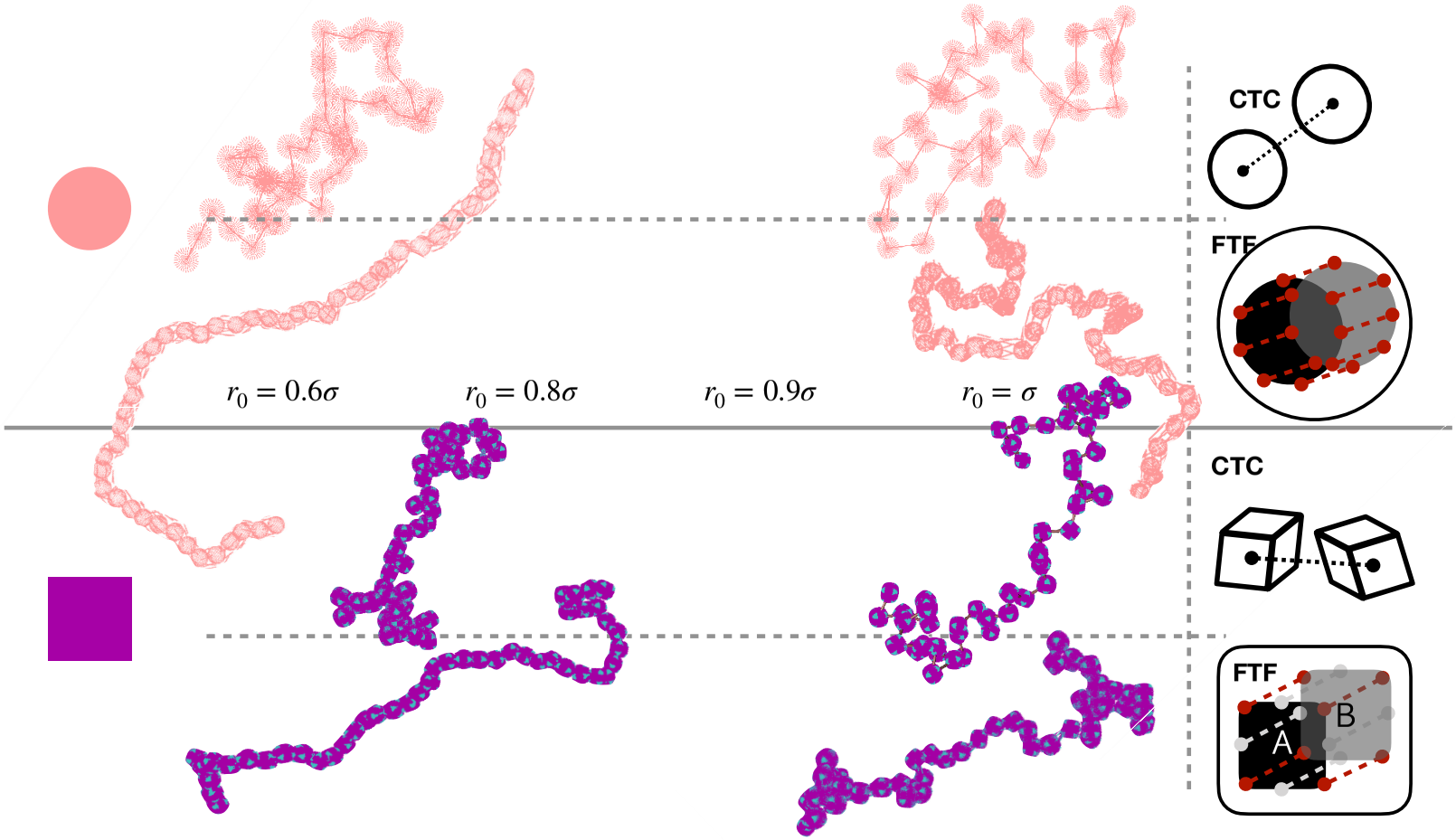

Figure 24: Representative simulation snapshots of the conformations our models take, across the combinations of monomer shape, crosslinking approach and r_0 we explored.

13

DNC NANOPOLYMER BASED MFs

Most existing procedures for synthesis of MFs are based on the functionalization of MNP surface.

As was discussed at in Chapter 10, DNC are nanoobjects that can self-assemble into nanopolymers, due to their shape anisotropy and selective inter-object interactions. The latter generalizes to what we refer to as a finely tunable nanostructure. DNC can form DNC-MNP complexes, with MNPs functionalized with ssDNA.[213] Magnetic properties on the level of a DNC-MNP complex are defined by the choice of material, diameter of the MNP and its coating, while structural properties are defined by the choice of k and l of M^l_k DNC. Therefore, DNC nanopolymers carrying MNPs, DNC MFs, fulfil the criteria brought forth in the Prologue for a compelling, representative member of highly magneto-responsive, smart nanomaterials.

The intricate relationship between the magnetic nature of monomers and crosslinking can result in notably different structural properties and responsiveness of MFs to external magnetic fields, underlining that the crosslinking mechanism strongly affects both magnetic and structural properties.[116] Considering the peculiarities of DNC nanopolymer crosslinking and the fact that monomer shape affects magnetic properties even in non-crosslinked systems,[44, 93] we expect an interesting shape/crosslinking interplay once MNPs are incorporated in DNC. This chapter is dedicated to exploring how does this interplay affect the magnetic response of DNC MFs.

13.1 POLYMERIC AND MAGNETIC PROPERTIES

In this section, we present how the magnetic nature and shape of FTF crosslinked monomers, relate to the response of MFs, to external magnetic fields. We compare these results to the magnetic response of a reference filament design, with ferromagnetic MNPs and constrained crosslinking (see Section. 5.1), extensively scrutinized in Part ii. We create filaments with 20 monomers and place each of them in a separate non-periodic ($500\sigma \times 500\sigma \times 500\sigma$) simulation box, at constant $T = 1$, initially fully straight and stretched (length of all bonds is their equilibrium length $r_0 = \alpha\sigma$), with the backbone orientated randomly. We run fifteen parallel, model/H/r_0 specific simulations, with $\vec{H}$ always directed along the z-axis. The simulation protocol here is identical to the one outlined in Chapter 12. Note that, independent of monomer shape, the magnetic core is assumed to be spherical in all models. However, considering the actual size of the DNC, we allow for the possibility of a spherical MNP to be ferro- or superparamagnetic, abbreviated below to SPM and FM correspondingly. In

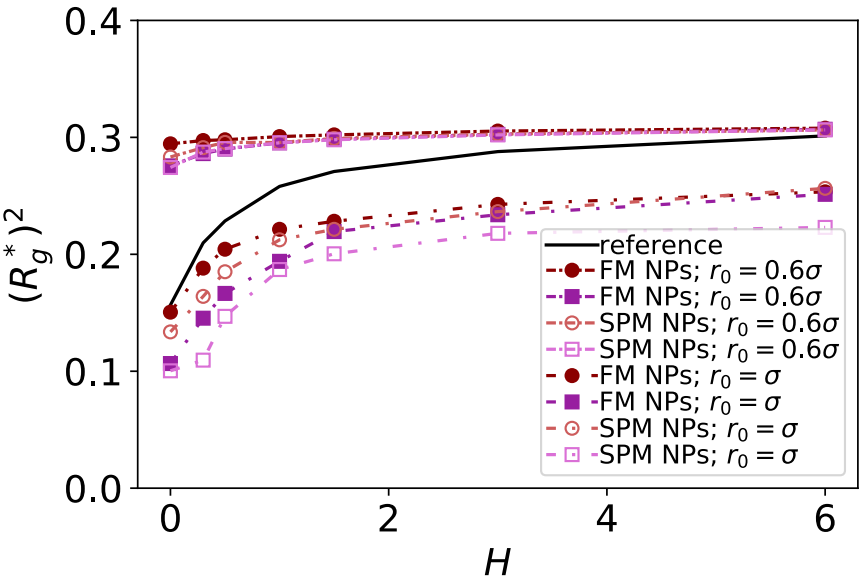

Figure 25: Comparison between models with FTF crosslinking: $(R_g^*)^2$ versus H. Data for filaments with spherical monomers are represented with spherical symbols (can); data for filaments with cubic monomers are represented with square symbols (purple). Filled symbols, shown in a darker color shade, represent filaments with ferromagnetic monomers; non-filed symbols, shown in a lighter color shade, represent filaments with super-paramagnetic monomers. Reference system of filament with ferromagnetic monomers and constrained crosslinking [116] is shown with a black, full line. Error bars are comparable to symbol size.

this way, we allow for the possibilities that without a magnetic field applied, MFs can be non-magnetic or have a remanent magnetization.

In Fig. 25, we plot the square of the normalized gyration radius R_g^{*2} given in Eq. (3.8), as a function of external magnetic field strength, $H = |\vec{H}|$. Here, $\vec{r}_i$ is the position vector of the i-th filament monomer in the lab coordinate frame and d_{avg} is the average inter-monomer distance. Comparing qualitatively across Fig. 25, the difference between overall R_g^{*2} profiles for different r_0 is stark. For $r_0 = 0.6\sigma$ the profiles are basically flat, regardless of monomer shape and the values of R_g^{*2} are higher than for the reference system. Results for $r_0 = \sigma$, reveal a rapid, field induced increase. Longer linkers make the shape effects visible. MFs with cubic monomers, due to lower inter-monomer correlations inherent to monomer shape anisotropy, have lower R_g^{*2} profiles overall, compared to their counterparts with spherical monomers. Interestingly, having super-paramagnetic monomers further diminishes inter-monomer correlations, compared to their ferromagnetic counterparts.

Further insight into filament response to external magnetic fields, comes from analyzing the filament magnetization $\overline{m}^*$, as introduced

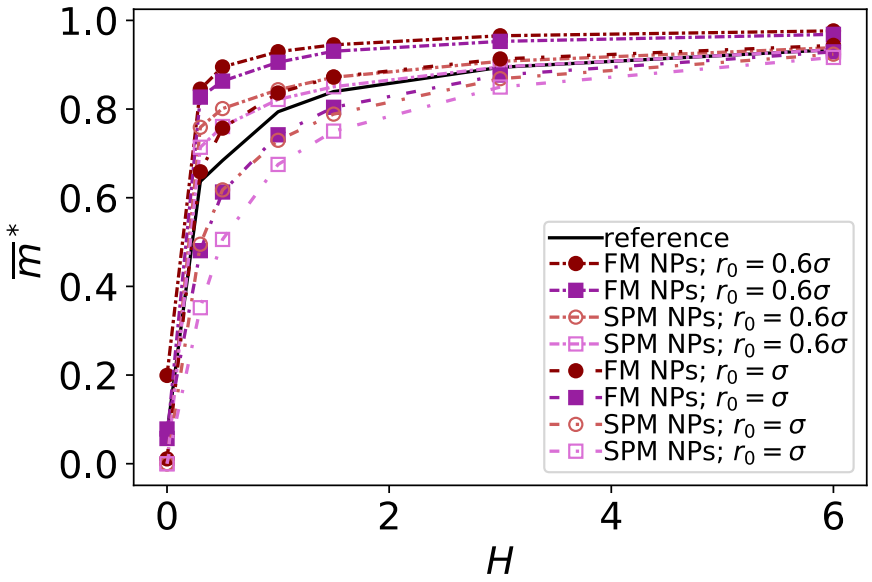

Figure 26: Comparison between models with FTF crosslinking: $\overline{m}^*$ versus H. Data for filaments with spherical monomers are represented with spherical symbols (can); data for filaments with cubic monomers are represented with square symbols (purple). Filled symbols, shown in a darker color shade, represent filaments with ferromagnetic monomers; non-filed symbols, shown in a lighter color shade, represent filaments with super-paramagnetic monomers. Reference system of filament with ferromagnetic monomers and constrained crosslinking [116] is shown with a black, full line. Error bars are comparable to symbol size.

in Chapter 6. In accordance with Fig. 25, Fig. 26 reveals that larger values of r_0 result in a lower magnetization. Still, as is apparent in the magnetization profiles, relatively low to moderate external magnetic fields are sufficient for MFs to be magnetized to saturation. For lower $r_0 = 0.6\sigma$, FTF crosslinking is restrictive enough to keep the monomers and dipole moments well oriented along $\vec{H}$, regardless of monomer shape, or magnetic nature of MNPs. MFs with super-paramagnetic monomers have an overall lower magnetization. Local dipole fields between neighboring monomers, introduce fluctuations of the direction of individual dipole moments within the filament. Filaments with ferromagnetic monomers, as can be seen in Fig. 26, are basically rod-like compared to the rest of the models presented. As r_0 increases, monomers can move more freely and dipole moment orientations can fluctuate more, which leads to an overall decrease in magnetization profiles. The shape anisotropy of cubes, on average, further inhibits the ability of dipole moments to predominately align with $\vec{H}$. This in turn means that cubic monomers crosslinked with FTF crosslinking, DNC MFs, while generally more elongated, have monomer dipole moments that fluctuate more than their coun-

terparts with spherical monomers. Therefore, an increase in r_0, leads to a more pronounced magnetization decrease for MFs with cubic monomers than for those made with spherical monomers. In fact, magnetization profiles for MFs with spherical, super-paramagnetic monomers and MFs with cubic, ferromagnetic monomers are basically indistinguishable.

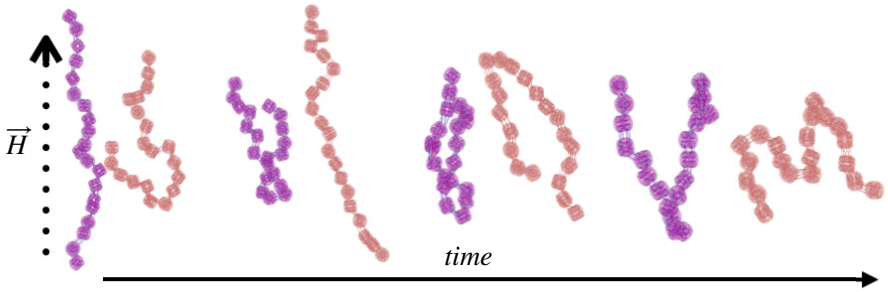

Figure 27: Typical conformations occurring during the runtime of two separate simulations (red and purple are meant to distinguish conformations found in independent simulation runs performed for the same system), revealing bend backbone conformations of DNC MFs with super-paramagnetic monomers and $r_0 = \sigma$.

In summary, Figs. 25 and 26 underline an effect that permeates the results here, namely the decorrelation of dipole monomer orientation in MFs with cubic monomers. DNC MFs have monomer dipole moments that locally fluctuate more. Zeeman coupling can compensate for this effect for all models, except for DNC MFs with super-paramagnetic MNPs, that do not fully stretch for high H. Instead, as it is shown in Fig. 27, we captured several instances of persisting conformation of DNC MFs with a bent backbone. This bending is a signature of MFs with super-paramagnetic spherical monomers [116] that is clearly intensified by the cubic shape.

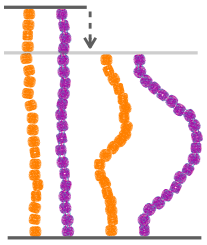

Figure 28: Simulation snapshots of conformations of DNC MFs with a bent backbone.

13.2 IN-FIELD COMPRESSION OF DNC MFS

In this section, we analyze whether the relative drawbacks of DNC MFs – less magnetically correlated monomers and more persistent bent backbone conformations – affect their mechanical response. As depicted in Fig. 28, we fix the ends of fully stretched FTF crosslinked MFs with 20 monomers (length of all bonds is their equilibrium length $r_0 = 0.6\sigma$), with different monomer shape and/or magnetic nature of colloids, on the surface of two semi-infinite slit walls. By moving one of the slit walls vertically towards the other, in steps Δd, we elucidate the effects of confinement on MFs and their response to compression, with and without an external magnetic field pointing antiparallelly to the direction of compression. We run ten parallel, model specific simulations, for different values of H at constant $T = 1$. Compression was realized by moving the steric planes in increments

of 0.1 every 300000 integrations, until we reached maximum desired compression of five length-scales. With this we ensure that filaments reach equilibrium before each compression step.

The initial, fully stretched conformation (no compression) of a filament is entropically disadvantageous. Indeed, this is confirmed by Fig. 25, where one can notice that the $(R_g^*)^2$ never approaches that of a rod, $(R_g^*)^2 \sim 0.34$. As a result of this, looking at Figs. 29b and 29c the projection of the force a filament exerts the bottom wall, on the axis of compression is positive. This shows that the filaments are pulling on the bottom wall. With further compression, entropy grows as the filament is given more freedom to fluctuate. At a certain compression, d_C, the filament can reach conformations corresponding to its equilibrium $(R_g^*)^2$, shown in Fig. 25. For such conformations, no net force is exerted on the walls, and the force-displacement curves cross zero. Looking at orange curves in Fig. 29b we compare MFs with ferromagnetic spherical monomers to their counterparts with cubic ones, without an external magnetic field applied. We see that they stop pulling on the wall at different d_C. MFs with spherical monomers have a slightly higher $(R_g^*)^2$ (see Fig. 25) than their counterparts with cubic monomers. Therefore, they do not need to be given as much leeway to be able to reach equilibrium radius of gyration, corresponding a freely moving filament. For further displacement of the top wall in the range we explored, MFs with ferromagnetic monomers, regardless of monomer shape, oscillate around the zero position.

Switching on the external magnetic field, depicted by green ($H = 3$) and violet ($H = 6$) curves, we see the ramifications of correlations induced by Zeeman coupling. Stretched out configurations with head-to-tail dipole arrangements are facilitated by Zeeman coupling leading to smaller values of d_C. However, given that the $(R_g^*)^2$ profiles of freely moving MFs with spherical monomers and $r_0 = 0.6\sigma$ are basically flat, only a small difference between d_C at any strength of magnetic field applied is observed. For their counterparts with cubic monomers, a difference can be noticed if the field is switched on. This is in line with the small $(R_g^*)^2$ increase observed in Fig. 25. On further compression past d_C, the force becomes repulsive, corresponding to MFs pushing on the bottom wall. Notice that for MFs with cubic monomers, the repulsive regime is reached for larger compression, than for their counterparts with spherical monomers. This is entirely in line with the dipole de-correlation effect we referred to earlier. Force-compression curves for MFs with super-paramagnetic monomers, shown in Fig. 29c, exhibit qualitatively the same trends seen in Fig. 29b. The most apparent difference, however, is a dependence of d_C on H, for MFs with the same monomer shape. This can be understood from the magnetization curves in Fig. 26, where for MFs with ferromagnetic monomers, $H = 3$ is already sufficiently

(a)

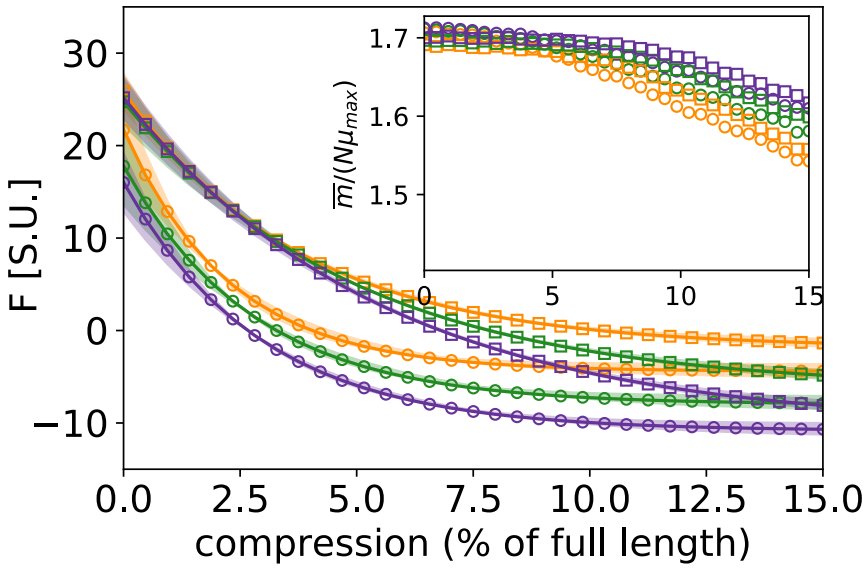

(b)

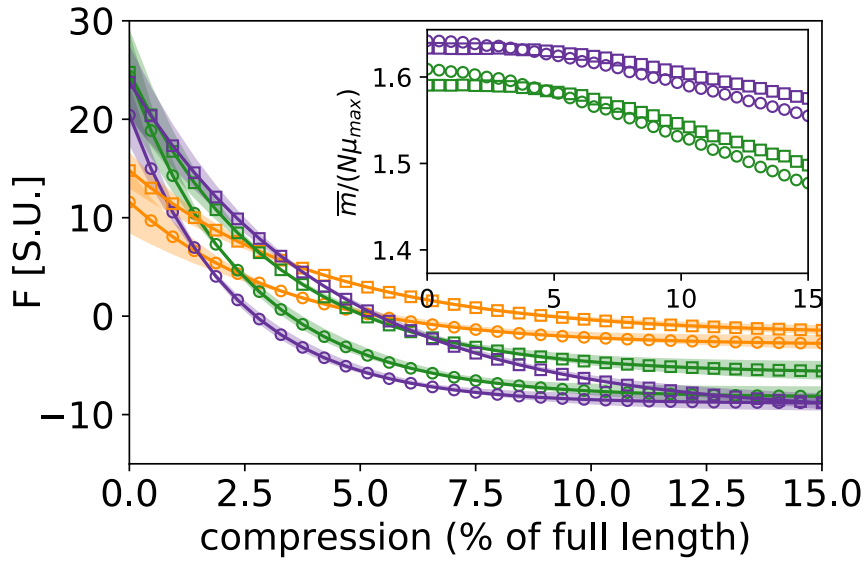

(c)

Figure 29: Force projection-compression curves for FTF crosslinked MFs with (b) ferromagnetic and (c) super-paramagnetic monomers. Exponential fits are plotted. Errors shown as confidence intervals, matching color halos around each force profile. Insets are showing the projection of the magnetization on the compression axis, at equilibrium of confined, FTF crosslinked MFs with (b) ferromagnetic; (c) super-paramagnetic monomers, respectively, as a function of compression.

strong to reach saturation magnetization, while for MFs with super-paramagnetic monomers it is not.

Looking at insets of Figs. 29b and 29c, showing the projection of the magnetization on the compression axis, at equilibrium, for MFs with ferromagnetic and super-paramagnetic monomers, respectively, we see a crossover between two linear magnetization regimes. The change of the regimes happens at corresponding values of d_C. The differences between ferro- and super-paramagnetic monomers is manifested in the absolute scale of the magnetization before d_C. Past d_C, the growing separation between the magnetization curves reflects the competition between entropy on one side and dipole-dipole interactions with Zeeman coupling, on the other.

In summary, based on the analysis of mechanical resistance to compression, cubic monomer shape of DNC MFs proves to be advantageous, compared to MFs with spherical monomers, with a smoother and more controllable response to compression.

Part IV

IN-FIELD DYNAMICS OF MFS IN SHEAR FLOW

The following chapters are dedicated to the study of conformational instability and reorientational dynamics of MFs in shear flow, with and without an applied magnetic field perpendicular to the flow direction. We show that MFs exhibit different dynamics, based on the magnetic nature and shape of monomers.

14 INTRODUCTION

Rheology of polymer-like systems in shear flow, if the list of applications presented in the Prologue is any indication, are of broad interest and great relevance in soft matter research. Polymeric systems are known to exhibit rich and varied dynamic in shear flow. Furthermore, it is understood that their non-equilibrium conformations and reorientational dynamics can be modified in a multitude of ways apart from shear rate,[32–34, 86, 103, 138, 150, 177, 198] out of which applying magnetic fields is of specific interest for this thesis.[30, 108] The most commonly observed reorientational dynamics of polymer-like systems in high Weissenberg number W shear flow [1] (*i.e.*, when the characteristic time of the flow is shorter than the polymer relaxation time) is tumbling. It is characterized by a polymer-like structure alternatively adapting stretched and collapsed conformations along the flow direction. In time, a tumbling polymer flips "head" over "tail". However, MFs with ferromagnetic monomers exposed to an external magnetic field perpendicular to the flow-vorticity plane (normal magnetic field), due to a competition of torques acting on the monomers caused by Zeeman coupling and hydrodynamic interactions, stabilize at an angle between the filament backbone and the flow direction.[108] Monomer shape effects on these conclusions were previously not explored.

Weissenberg and Deborah number are often used interchangeably. While we do not engage in such questionable semantics, I would like to encourage the reader to read the remarkable paper by Reiner [136]

In Part iii of this thesis, we brought forward that monomer shape does not really affect equilibrium properties of MFs if crosslinking is restrictive enough, meaning that very short crosslinkers or very rigid ones conceal monomer shape effects. In this case crosslinking dominates inter-particle correlations. Magnetoresponsiveness tends to be affected by monomer shape most, for MFs with relatively long and stretchy bonds, crosslinked in such a way that dipole moments point in the same direction along the filament backbone and that their translational and rotational degrees of freedom are coupled to the backbone. The latter design criterion, as discussed in Part ii, is necessary to capture the nature of ferromagnetic MNPs in a filament. Furthermore, we have seen that the magnetic response of MFs with different magnetic nature of monomers can be remarkably similar, depending on the crosslinking. The main distinction in magnetization we noted is that MFs with super-paramagnetic monomers are more responsive to weak magnetic fields than their counterparts with ferro-

1 Weissenberg number is essentially the ratio between elastic and viscous forces. Characteristic flow time, determined by viscous forces is just the inverse of the shear rate. Relaxation time of a polymer can in principle be relative to investigation goals. Usually, it is determined as the decorrelation time of the radius of gyration.

magnetic monomers. However, magnetic nature of monomers leads to vastly different filament conformations at equilibrium. Filaments with super-paramagnetic monomers tend to bend their backbone in attempts to minimize dipole-dipole interaction energy, in external magnetic fields. It is reasonable to expect that the conformational differences between MFs due to the magnetic nature of monomers in external magnetic fields, reflect greatly the rheology of filaments in shear flow in a normal magnetic field.

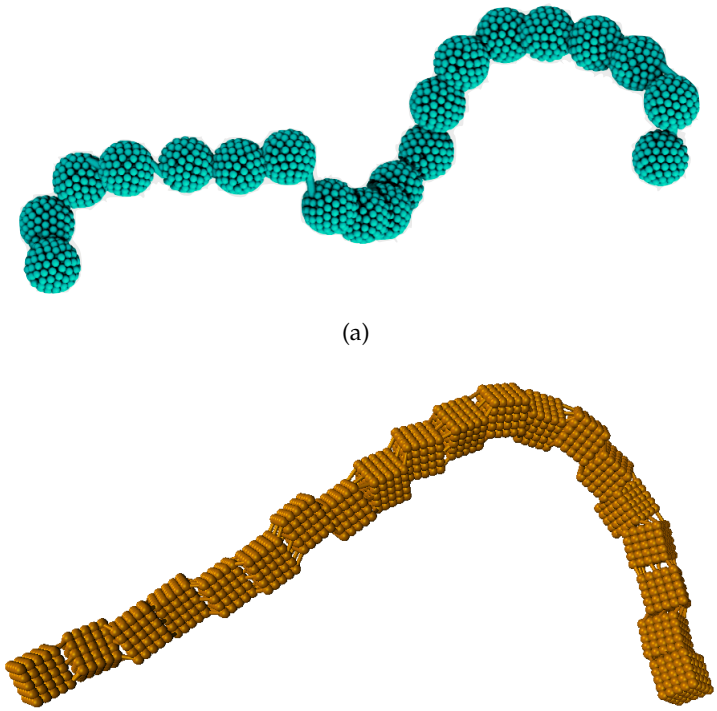

(a)

(b)

Figure 30: Simulation renders of models used to obtain results in Chapter 15 and 16. (a) is showing sMFs. (b) is showing cMFs, based on DNC nanopolymers

Here, using MD simulations coupled with the Lattice-Boltzmann method (LBM), we tackle the implications of filament architecture, monomer magnetic nature and shape on the conformational instability and reorientational dynamics of MFs in shear flow, with and without a normal magnetic field applied. Computational models we in the following chapters, namely, sMFs and cMFs, are visualized in Fig. 30. sMFs stands for filaments with spherical monomers and constrained crosslinking (see Section 5.1). cMFs stands for the M_{16}^{40} DNC nanopolymer inspired filament model, with cubic monomers and FTF crosslinking. In fact, sMFs and cMFs differ to MFs with constrained crosslinking discussed in Part ii and M_{16}^{40} cMFs discussed in Part iii, respectively, in the way the monomers were designed. This is further elaborated on in Section 14.4. Importantly, these models reflect best practice design criteria established throughout this thesis.

14.1 MESOSCOPIC FLUID DESCRIPTION

In Section 3.1 we outlined relevant time and length scales from the point of view of polymer physics, which is also where the phenomenology that is the subject of this thesis resides. The MD scheme is tuned in accordance with the physical requirements and technical restrictions. Up until this point in the thesis, we used Langevin dynamics exclusively, where the effects of a thermalized fluid are represented implicitly by sampling a random force distribution. This works well since the relevant time scales are large enough, that the atomistic picture of the fluid can be averaged out. However, in this picture, implications of hydrodynamic interactions are also averaged out.

MD simulations could in principle be used to solve the NSE. However, given that a gram of water contains 10^{22} molecules, it is not quite practical.

In general, the mathematical description of fluid dynamics relies on the continuum assumption. This is essentially a macroscopic description of fluids that relates directly to physical, experimentally accessible quantities such as viscosity and density. The governing equation of fluid dynamics macroscopically is the Navier-Stokes equation (NSE). This level of description is diametrically opposite to the microscopic, usually Hamiltonian level description, where the governing equations are Newtons equations, describing reversible dynamics. In this work, however, we are interested in a mesoscopic description of fluid dynamics, where the governing equation is the Boltzmann equation. The Boltzmann equation is the basis of the Lattice-Boltzmann method we rely on extensively throughout the rest of this thesis. The discussion that follows is formally in continuation of Section 3.1.

The length scale at which a system relaxes to local equilibrium through collision events can be quantified using the Knudsen number:

$$Kn = \frac{d_{mfp}}{d_{ch}}, \tag{14.1}$$

where d_{mfp} is the kinetic theory mean free path, and d_{ch} is the characteristic length scale of the physical quantity we are interested in resolving (see Section 14.5). For $Kn > 1$ one takes the point of view of kinetic theory. However, if we are curious about fluid flow, we should focus on length scales where one can observe the fluid migrating from one region into another, where $Kn < 1$. Hydrodynamic interactions cause objects to flow, due to viscous forces. However, object motion in general can be caused by a multitude of forces apart from viscous ones. Therefore, we distinguish the viscous regime where we observe diffusion dynamics, from inertial regime where one observes advective dynamics.[2] The ratio between the time scales of these

2 Advection and diffusion are easily understood in the context of the continuity equation $\partial\rho/\partial t + \nabla \cdot \vec{j} = 0$, where $\vec{j} = D\nabla\rho + \vec{v}\rho$. ρ is the fluid element density, D is the diffusion coefficient, $\vec{v}$ local velocity of the fluid.

two regimes for a given system is the definition of the well-known Reynolds number:

$$Re = \frac{u\sigma}{\nu}, \tag{14.2}$$

where $u = |\vec{u}|$ is the fluid velocity and ν is the kinematic viscosity of a fluid. We are interested exclusively in the $Re << 1$ regime. Furthermore, we consider only incompressible fluids. This is a sound assumption if the time scale of propagation of compression waves in a fluid is lower than the advective time scale. This is quantified using the Mach number:

$$Ma = \frac{u}{c_s}, \tag{14.3}$$

where c_s is the speed of sound. Dimensionless parameters Kn, Re and Ma form a set that defines a fluid flow. In this framework, any other fluid flow, with the same dimensionless numbers, reproduces the same physics.

14.2 THE LATTICE-BOLTZMANN METHOD

As is said in Section 14.1, in this work we are interested in the mesoscopic fluid description governed by the Boltzmann equation. The Boltzmann equation is conventionally given in the following form:

$$\Omega(f) = \frac{\partial f(\vec{x}, \vec{\xi}, t)}{\partial t} + \xi_\beta \frac{\partial f(\vec{x}, \vec{\xi}, t)}{\partial x_\beta} + \frac{\vec{F}_\beta \partial f(\vec{x}, \vec{\xi}, t)}{\partial \xi_\beta}, \tag{14.4}$$

where $f(\vec{x}, \vec{\xi}, t)$ is the particle distribution function, $\vec{\xi}$ is the microscopic particle velocity and $\vec{F}_\beta$ is the specific body force. $f(\vec{x}, \vec{\xi}, t)$ is essentially a generalization of mass density, simultaneously represented in position and velocity space. In other words, it represents the probability of finding a molecule in a phase space volume $d^3\vec{x}d^3\vec{\xi}$, at a time t. The quantity $f(\vec{x}, \vec{\xi}, t)d^3\vec{x}d^3\vec{\xi}$ corresponds to the population in a particular cell of the phase space. The Boltzmann equation is rather intuitive to understand. On the right-hand side, the first two terms of the describe advection of monomers, while the third term envelopes the forces that cause the advection at velocity $\vec{\xi}$. Therefore, we can understand the left-hand side of the equation as the source term. $\Omega(f)$ is commonly referred to as the Collision operator.

The mesoscopic fluid description is an effective bridge between the fundamental physics happening on the microscopic level, with the macroscopic quantities we can handle efficiently. This is true as long as microscopic conservation laws relate to macroscopic conservation laws. The link between is the mesoscopic level description. We make

the strong but macroscopically reasonable assumption that we conserve mass, momentum, and energy (total and internal) microscopically.[3] However, macroscopic conservation equations derived from basic kinetic theory have only mass conservation guaranteed. Momentum and energy conservation depend on the form of $f(\vec{x}, \vec{\xi}, t)$.

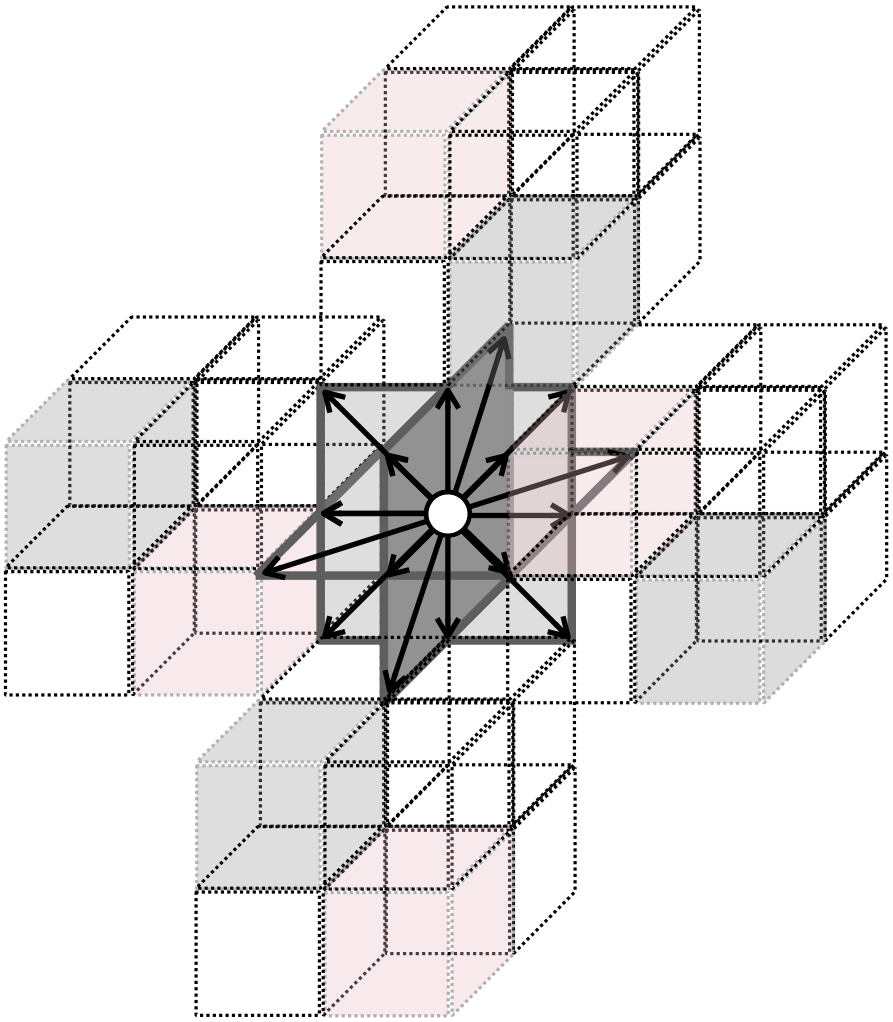

Figure 31: Schematic depiction of an LBM lattice. Fluid populations migrate between the lattice nodes in discrete timesteps and with discrete velocities. Black arrows denote the D3Q19 velocity set we used. From the central node (white circle), the velocity vectors point towards the 18 nearest neighbors' nodes. The 19-th velocity vector is the rest mode (zero velocity)

Final strong assumption we make is that $f(\vec{x}, \vec{\xi}, t)$, provided enough time has passed during which the system was not perturbed, converges to the Maxwell-Boltzmann distribution around $\vec{\xi} = \vec{u}$, denoted by $f_{eq}(|\vec{u}|)$, where $\vec{u}$ is the mean velocity. The simplest possible form of a collision operator that respects the microscopic conservation laws

3 Microscopic conservation laws are expressed as moments of the collision operator.

and ensures that a local $f(\vec{x}, \vec{\xi}, t)$ converges to $f_{eq}(|\vec{u}|)$ is the Bhatnagar, Gross, and Krook (BGK) operator:

$$\Omega(f) = -\frac{1}{\tau}(f(\vec{x}, \vec{\xi}, t) - f_{eq}(|\vec{u}|)) \tag{14.5}$$

where τ is the relaxation time, determining the rate of relaxation towards equilibrium. For the academic discussion presented here we will stick to the BGK collision operator. However, the LBM Implementation used in this thesis uses the multiple-relaxation-time (MRT) operator, which resolves some potential pitfalls, discussion of which is not very relevant for the scope of this work.[6, 20] From here, it is relatively simple to formalize how to relate kinetic theory to a macroscopic fluid. Taking the idea of Chapman and Enskog, one can use perturbation theory to generally represent $f(\vec{x}, \vec{\xi}, t)$ in terms of deviations from the equilibrium distribution. It turns out that already the first order approximation $f(\vec{x}, \vec{\xi}, t) = f_{eq}(|\vec{u}|) + \alpha f^{(1)}(\vec{x}, \vec{\xi}, t)$ can describe the macroscopic behavior of a fluid as given by NSE. With this we outline the general idea of the Lattice-Boltzmann method: from numerical solutions of the Boltzmann equation, one can find a solution to the NSE. While solving the Boltzmann equation analytically is very difficult, numerical schemes to do so are fabulously simple to implement.

A discussion of lattice-gas automata which asymptotically go to NSE such as in Frisch, Hasslacher, and Pomeau [59], is very helpful for understanding LBM. *Generally, the author finds work on cellular automata to be quite engaging readings.*

LBM is a competitive second-order accurate solver of the weakly compressible NSE. It was inspired by the lattice automata models, and it uses a discretized velocity space, in addition to spatial and temporal discretization. The key benefit in doing so is that a particle distribution function can be exchanged for a set of discrete distribution functions $f_i(\vec{x}, t)$, one for each velocity $\vec{v}_i$. In fact, velocity space discretization forms a set $\{w_i, \vec{v}_i\}$, where w_i are relative weighing coefficients. While there are many possible discretization sets, we use the D3Q19, which is the most commonly used one. (see Fig. 31) This set determines population migration from one lattice node to another, in a single timestep. The Boltzmann equation, discrete in velocity, position, and time space, also called the lattice Boltzmann equation is given by:

$$f_i(\vec{x} + \vec{v}_i \Delta t, t + \Delta t) = f_i(\vec{x}, t) - \frac{\Delta t}{\tau}(f_i(\vec{x}, t) - f_i^{eq}(\vec{x}, t)), \tag{14.6}$$

where we have used the discretized version of the BKG collision operator. The MRT operator, however, replaces the relaxation time of the BGK operator with a matrix consisting of, for the D3Q19 velocity set, 19 relaxation times. However, with judicious use of the symmetries inherent to the D3Q19 set, only four independent relaxation times remain, two of which are for the shear and bulk viscosity.[4]

4 The remaining two relaxation times are free parameters with no specific correspondence to a physical quantity. They can be adjusted to optimize algorithm stability.

Provided a reasonably simple way to determine $f_i^{eq}(\vec{x}, t)$, we have outlined the basic LBM algorithm.[5] With the assumption that $f_{eq}(|\vec{u}|)$ is the Maxwell-Boltzmann distribution, it is possible to express it as a weighted, truncated sum of Hermite polynomials. In a discrete velocity space, this is sufficient to obtain the correct macroscopic conservation laws. In summary, given an initial $f_i(\vec{x}, t)$, the LBM algorithm iteratively finds the $f_i^{eq}(\vec{x}, t)$ and the corresponding $f_i(\vec{x} + \vec{v}_i \Delta t, t + \Delta t)$, from the moments of $f_i(\vec{x}, t)$. The result is applied to neighboring nodes of our discrete space. In other words, populations migrate to lattice cells according to where the corresponding velocity points to. Subsequently, distribution functions in each lattice cell are relaxed towards the local thermodynamic equilibrium.

14.3 FROM BOUNDARY CONDITIONS TO SHEAR FLOW IN LBM

The Lattice-Boltzmann method is essentially a numerical scheme that solves a discretized version of the Boltzmann equation, which is a linear partial differential equation. Therefore, boundary conditions with LBM are relatively simple to deal with. This is in fact one of the main advantages of the Lattice-Boltzmann approach. In general, solving a time-dependent flow problem requires the specification of initial conditions in the entire domain. However, for discrete methods a more general initialization step is necessary, which takes care that computations also do not start with random values. If the objective is a steady-state solution (as it is for the purposes of this thesis), it is sufficient to set initial populations to equilibrium.

On the other hand, if a solution of our differential equation describing the physical process varies spatially, one needs to also prescribe boundary conditions. In hydrodynamics, this is normally achieved by specifying Dirichlet or Neumann conditions for the fluid velocity. Boundary conditions in numerical methods, however, must be implemented as part of the algorithm and as such must be given special attention to. In LBM, the boundary conditions are applied on the boundary nodes. In this thesis we make use of periodic boundary conditions and the bounce-back (BB) method of dealing with solid boundaries in LBM.

If the order of accuracy of boundary conditions is less than the overall accuracy of the discretized numerical scheme, the accuracy of the solution may degrade everywhere.

Periodic boundary conditions are in principle appropriate in situations where the flow solution is periodic, or at length scales where the flow profile is a steady state. Fluid passing through the boundary re-enters instantaneously from the opposite side boundary.[6] An example of a situation, of relevance for this work, where such a handling of boundaries is appropriate, is flow in a microchannel at low Reynolds numbers. On the other hand, if a population meets a solid bound-

5 The discretized equilibrium $f_i^{eq}(\vec{x}, t)$ can be obtained locally from the local density ρ and fluid velocity $\vec{u}$, which are calculated as the moments of local $f_i(\vec{x}, t)$.

6 Periodic boundary conditions conserve mass and momentum by construction

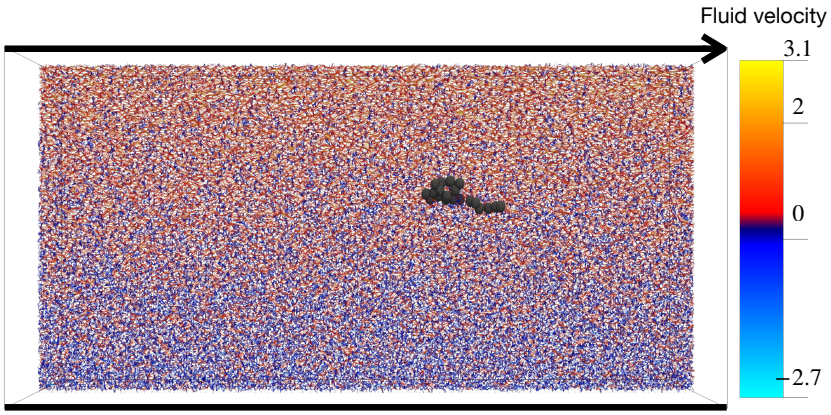

Figure 32: Visualization of an sMF in thermal shear flow from one of our simulations at $W = 30$, $T = 1$. Black lines denote the BB boundaries, where the arrow on the top boundary indicates that the boundary is moving with a given velocity along the x-axis. Simulation box is periodic in the yz-plane. Fluid streamlines are colored based on local flow axis (x-axis) velocity.

ary during propagation, BB method dictates that it will be reflected to its original location with its velocity reversed. If the boundary is moving, the momentum of bounced-back populations is adjusted to respects Galilean invariance. This implies no relative transverse motion between the fluid and the boundary. Therefore, the BB method mirrors the Dirichlet boundary condition for the macroscopic velocity at the wall and leads to a no-slip velocity condition for a resting or moving wall, located midway on the link between lattice nodes.[7]

Momentum transfer requires the knowledge of local density at the boundary. In flow configurations where there is no mass flux across the boundaries, such as in parallel shear flow, this is not an issue.

With this, we are finally able to specify how we achieve shear flow. We make a rectangular simulation box, periodic in the yz-plane. Along the x-axis we place two, 2D periodic BB boundaries, one of which is stationary, while the other can move with a specified velocity along the z-axis, which is the long axis of our rectangular box. (see Fig. 32)

14.4 FLUID-PARTICLE COUPLING AND THE RASPBERRY MODEL

We want to use a mesoscopic method (Lattice-Boltzmann) to simulate a nanoscopic polymer-like system (magnetic filament) in a flow profile (shear) of a fluid defined by macroscopically measurable quantities (*i.e.*, kinematic viscosity and density). We are trying to bridge vastly different length and time scales. Furthermore, we tackled the microscopic description of nanoscopic MFs, at some length, using

7 The boundary is midway between nodes only approximately, and placed in such a way so that the BB method can be second-order accurate.

MD simulations. To explicitly include a flow profile in our simulations, the pragmatic thing to do is to somehow include the hydrodynamic forces arising due to the fluid viscosity in to the MD scheme. This is in fact one of the ways to couple an LBM fluid with MD particles, called the frictional coupling scheme.[2, 3, 48, 107]

The general idea of the force coupling scheme is that the force acting on a point particle moving with the speed $\vec{v}$ relative to the fluid is proportional to the Stokes friction, given by:

$$\gamma_S = 6\pi\eta r_h \tag{14.7}$$

where η is the dynamic viscosity and r_h is the hydrodynamic radius of an effective "Stokes sphere". In other words, the frictional coupling scheme interprets every particle as a sphere with an effective size. However, in LBM, the proportionality factor is not quite γ_S, but an artificial friction usually called the bare friction γ_B, that is essentially a fit parameter that needs to be tuned to reproduce the actual size of the colloids we are simulating. Given that in LBM, we resolve the fluid in a discrete space, its velocity is mapped on to a smooth space (or a position of an MD particle) using trilinear interpolation.

Finally, one needs to have in mind that as such, the MD scheme and LBM run completely independent of each other. To maintain momentum conservation, the opposite force to the one acting on a particle must be distributed to the surrounding nodes. Additionally, for energy conservation, one needs to maintain a constant temperature. This is achieved by an addition of random forces, according to the fluctuation dissipation theorem, analogous to the Langevin thermostat. Altogether, the fluid-particle coupling force is given by,[3]

$$\vec{F} = -\gamma_B \vec{v} + \vec{\mathcal{F}}, \tag{14.8}$$

where $\vec{\mathcal{F}}$ is the stochastic force respecting

$$< \mathcal{F}_i(t)\mathcal{F}_j(t') >= 2\gamma_B k_B T \delta_{ij} \delta(t - t'). \tag{14.9}$$

Having outlined how LBM handles fluid-particle coupling, it would seem that it is limited to spherical particles. Furthermore, it is not possible to simulate rotational diffusion of particles in this way. To be able to accurately capture the hydrodynamic effects on the monomers in our simulations, we once again rely on the raspberry model. In Section 10.2, we used a combination of the super-ball equation and the raspberry model, to construct a monomer with a complex shape, with an emphasis on obtaining a smooth steric surface. Here, however, the raspberry is designed in accordance with the requirements of the LBM algorithm (see Fig. 33). A single particle in a simulation box can only couple to a single lattice site per timestep. Using the raspberry model, one can construct a monomer with an arbitrary shape by homogeneously filling its volume with particles that serve as fluid

coupling points. The MD scheme is coupled only to the center-of-mass particle, and all other particles in the monomer are fixed with respect to it. The moment of inertia tensor of this particle is set according to the mass and shape of the monomer. We construct raspberry monomers for sMFs using the procedure described by Fischer et al. [57]. Cubic monomers in cMFs are modeled as a $5 \times 5 \times 5$ mesh grid of virtual sites. We once again come to the important point of γ_B

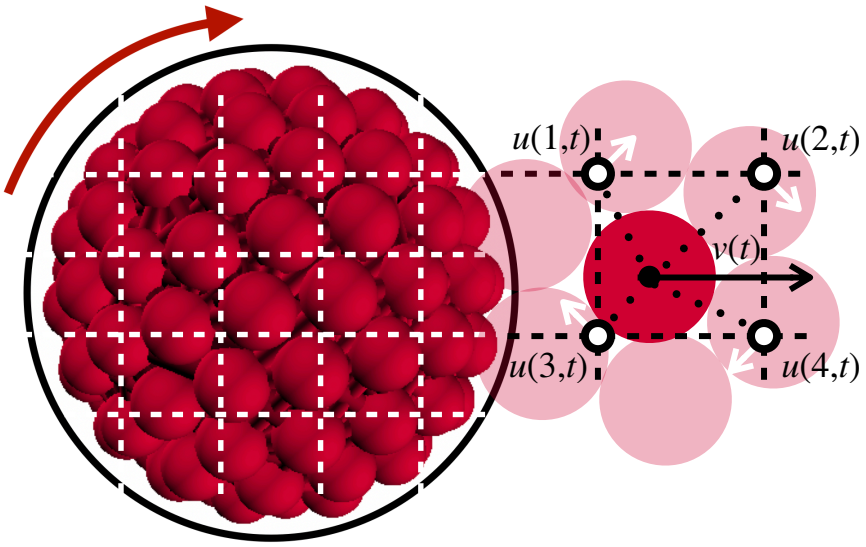

Figure 33: Schematic depiction of a raspberry monomer in LBM with the frictional coupling scheme between the fluid and particles. Local fluid velocity at the particle position is obtained by trilinear interpolation of the fluid velocity from lattice nodes immediately around it. A force is applied one each particle, based on the particle velocity relative to the interpolated fluid velocity based on Eq. (14.8)

and the effective size of monomers in simulations. While there most definitely are expressions developed to relate them, it is difficult to generalize the results of such expressions to a raspberry. Construction of raspberry monomers to be used with LBM is a balancing act between computational load, time scale, monomer shape and how finely one needs to resolve its steric surface. In general, particles filling out the volume of a raspberry monomer should be as homogeneously distributed as possible and their density, in conjunction with γ_B, should be tuned so that the translational and rotational diffusion coefficients D_t and D_r of the raspberry correspond to the expected hydrodynamic radius r_h.

Let us outline a typical workflow to check if a raspberry monomer reproduces the correct hydrodynamic size (remember that a cube can be interpreted as a Stokes sphere with an equivalent surface area.) One can obtain the translational diffusion coefficient D_t from the slope of the mean-square displacement of a monomer, in the diffu-

sive regime. The hydrodynamic radius of a Stokes sphere for a given D_t can be obtained using the Stokes-Einstein relation:

$$D_t = \frac{k_B T}{6\pi\eta r_h}. \tag{14.10}$$

One also needs to check r_h obtained from the rotational diffusion coefficient D_r, by calculating the directional correlation function of the raspberry director $d(t) \cdot d(0) = \cos\theta(t)$. Correlations between temporally separated directors of a raspberry decay exponentially, and are related to D_r with:

$$< \cos\theta > (t) = e^{-2D_r t}. \tag{14.11}$$

This approach is called the Green-Kubo method, which can also be used for D_t, where one would use the center of mass velocity autocorrelation function instead. The Stokes-Einstein relation connecting D_r with r_h is given by:

$$D_r = \frac{k_B T}{8\pi\eta r_h^3}. \tag{14.12}$$

In general, r_h^T extracted from D_T, and r_h^R extracted from D_R will not match perfectly for a porous body such as a raspberry. The art of it is to construct a raspberry that has a close match between the radii extracted from D_t and D_r.

14.5 UNITS AND IMPLEMENTATION NOTES

Analogously to Chapter 10.3, the interaction potential between a pair of monomers in our simulations is determined by the interplay between the steric interaction and the bonds between them. We match the parameters so, that the overall interaction potential between nearest neighbors is nearly the same for sMFs and cMFs. The length scale is prescribed by monomer hydrodynamic radius, which is chosen to be $r_h = 9nm$. For sMFs this means that $\sigma = 3[x]$ in reduced units, where $[x]$ is the length scale. However, raspberry monomers in sMFs reproduce $r_h = 9.72nm$ ($r_h^T/r_h^R = 0.94$) for bare friction $\gamma_B = 8$. For cMFs this corresponds to a cube side length $\sigma = 2[x]$. However, raspberry monomers in cMFs reproduce a cube side length $a = 17.2nm$ ($r_h^T/r_h^R = 0.97$), for $\gamma_B = 3$. The simulation box is a 2D periodic rectangle with dimensions $L_{box} = (140[x], 280[x], 280[x])$, with periodic boundary conditions in the y-z plane.

The energy scale corresponds to the thermal energy at room temperature $[E] = k_b 300K$. Based on interaction potential matching, we determined that the energy scale of the steric repulsion between spherical monomers in sMFs should be achieved by a WCA potential on the center-of-mass particle corresponding to monomer size $\sigma_{LJ} = 3$ and $\epsilon = 1$. Steric repulsion between cubic monomers of cMFs is

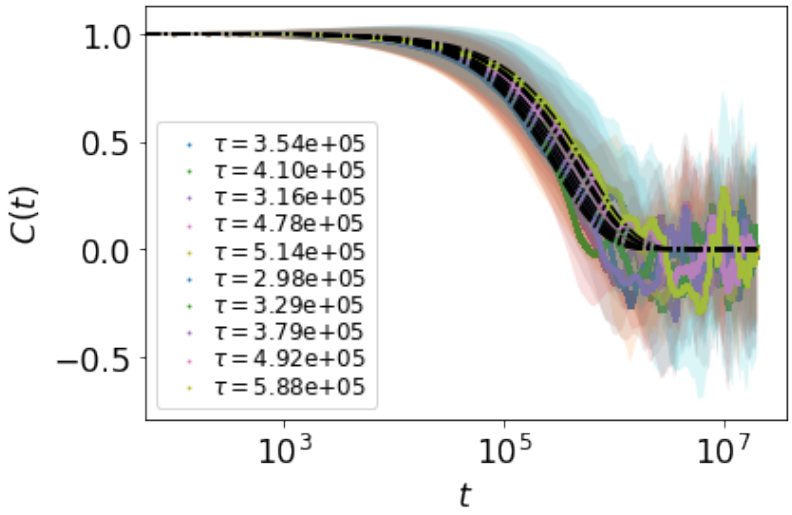

Figure 34: Showing the auto-correlation function $C(t)$ of the radius of gyration of ten randomly oriented nanopolymers with spherical monomers and constrained crosslinking, in a thermalized fluid. Black dash-dotted lines show exponential fits that decay with $1/\tau$, where τ is the characteristic time scale. Fits were performed on data until $t = 10^5$ integrations. Colored halos are confidence intervals of the fits.

achieved via a WCA potential on every particle on the surface on the monomer with $\sigma_{LJ} = 0.5$ and $\epsilon = 0.1$. Following the interaction potential matching strategy, we determined that FENE bonds in sMFs should be 9 times as rigid as the ones in cMFs. Therefore, for cMFs $K_f = 10$, while for sMFs crosslinking $K_f = 90$. Equilibrium length of FENE bonds is set to be a multiple of monomer size $r_0 = 0.6\sigma$. Maximal extension of each FENE bond, r_f, was set to be 3 times the equilibrium bond length r_0.

We choose the fluid density to correspond to water $\rho_w = 1 \times 10^3 \mathrm{kgm}^{-3}$. The LBM grid spacing is set to $a_{grid} = 1[x]$. Therefore, the mass scale for sMFs is set to $[m] = 2.15 \times 10^{-22}\mathrm{kg}$, while for cMFs $[m] = 7.3 \times 10^{-22}\mathrm{kg}$. Time scales in our simulations are $[t] = 1.37 \times 10^{-9}\mathrm{s}$ for sMFs and $[t] = 3.78 \times 10^{-9}\mathrm{s}$ for cMFs. In simulation, we adjust the timestep to match the overall time in the simulations in between sMFs and cMFs and slip velocity to match the shear forces regardless of model. In effect, we manage to match the characteristic time scales between the models (roughly), to be $\tau = 4.2 \times 10^5$ (see Fig 34).

We set the fluid kinematic viscosity to $\nu = 0.1\nu_w = 8.9 \times 10^{-8}\mathrm{m}^2\mathrm{s}^{-1}$, corresponding to $3.4[x]^2/[t]$ in simulation units for sMFs, and $4.1[x]^2/[t]$ for cMFs. This choice does not affect the physical results of our simulations while reducing simulation time by an order or magnitude.

Monomers in our simulations correspond to magnetite MNPs with a core density of $\rho_{Fe_2O_3} = 5.17 \times 10^3 \mathrm{kgm}^{-3}$, and a thin 1.5nm oleic

acid coating with $\rho_{C_{18}H_{34}O_2} = 0.89 \times 10^3 kgm^{-3}$. Therefore, dimensionless dipolar coupling parameter between the monomers in our simulations is fixed to $\lambda = 3$. This also means that the maximum of the applied magnetic field range we explored represents strong fields of about 0.26 T.

15

FIELD-INDUCED ORIENTATION OF MFS IN SHEAR FLOW

We start the discussion in this chapter by comparing the behavior of sMFs and cMFs with ferromagnetic monomers. In Fig. 35 we show the alignment angle θ of the filament backbone with respect to the flow direction, in the flow-field plane, as a function of W and H. The orientation of a filament is its principal gyration axis, calculated as the eigenvector corresponding to the largest eigenvalue of the gyration tensor, given by Eq. (3.9). Looking and Fig. 35, we see that θ as a function of W and H, is independent of monomer shape. For a fixed shear rate, increasing H leads to an increase of θ. Conversely, keeping H fixed, increase in W leads to a decrease of θ. In fact, one needs only a modestly strong normal magnetic field to eliminate tumbling in MFs with ferromagnetic monomers. Furthermore, the analytical es-

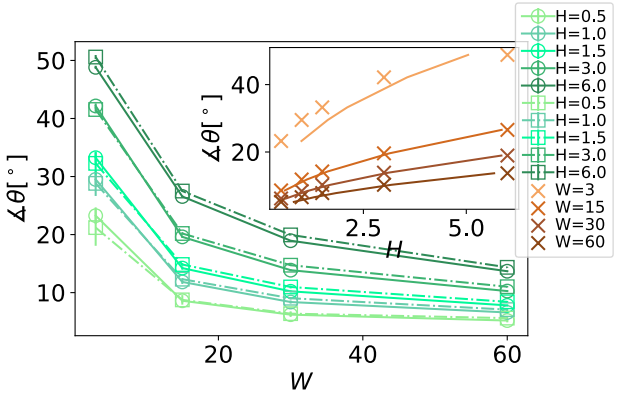

Figure 35: Showing the angle θ, for different H, as a function of W, comparing sMFs and cMFs with ferromagnetic monomers. Symbol shape corresponds to monomer shape. Error bars are calculated as the standard deviation of θ, across independent runs. Inset is showing θ as a function of H, for different filament designs and W. Data points correspond to simulation results while the lines correspond to the fit of the $H = (a/b)\sin(\theta)\tan(\theta)$ solution of Eq. (15.1), introduced in Lüsebrink et al. [108], where $b\cos(\theta) \neq 0$.

timation of θ obtained by balancing the hydrodynamic and magnetic torques acting on the center-of-mass of a filament:[108]

$$\Gamma\gamma\frac{N^2-1}{12}d_{avg}^2\sin^2(\theta) = \mu H\cos(\theta), \tag{15.1}$$

where Γ is the effective friction coefficient, γ is the shear rate and d_{avg} is the average inter-monomer distance, can be used to fit our

data, as shown in the inset of Fig. 35. This formula applies only if the stabilized filament conformations can be described as rod-like and if H and W are high enough to overcome thermal fluctuation effects. The limits of applicability are depicted in the fits for $W = 3$ (weak shear) and/or $H = 6$ (strong field). It comes as a surprise that monomer shape has no effect on θ. It is known that hydrodynamic forces excreted on cubic monomers are higher than for a corresponding sphere.[121] By proxy, the overall hydrodynamic torque for cMFs is expected to be higher than for sMFs. It must be that this increased hydrodynamic torque due to monomer cubicity is balanced with a complementary increase in magnetic torques in MFs with cubic monomers.

In Fig. 36a we plot the difference in ϕ between sMFs and cMFs, denoted as $\Delta\phi$, where ϕ is the angle the overall magnetic moment of a filament $\vec{\mu}_{tot} = \sum_{i=1}^{N} \vec{\mu}_i$, where $\vec{\mu}_i$ is the dipole moment of the i-th monomer and N is the monomer number, encloses with the filament backbone. Indeed, the difference in hydrodynamic interactions based on monomer shape is compensated with magnetic torques. Looking at Fig. 36a, $\Delta\phi$ suggests that $\vec{\mu}_{tot}$ for sMFs is on average less aligned with the filament backbone compared to cMFs. For the parameters we explored, $\Delta\phi$ is 10° at worst, and 5° at best. Low W and high H offer the least hydrodynamic counter-torque for dipole moments to reorient along $\vec{H}$. Spherical monomers easily slide past one another and rotate with respect to each other. Cubic monomer shape, on the other hand, penalizes such motion. As a result, dipole moments in filaments with cubic monomers are more aligned with the backbone than they would be in filaments with spherical monomers. Therefore, magnetic torque due to Zeeman coupling is higher for cMFs than for sMFs, and θ appears to be invariant to monomer shape. In Fig. 36b we show simulation renders for the parameter set $(W = 3; H = 6)$, corresponding to the highest $\Delta\phi$ shown in Fig. 36a, that depicts the conclusions from the paragraph above: dipole moments in an sMF fluctuate more with respect to the main axis (the deviation is color-coded, as shown on the side). Here, it can also be seen that a cMF is on average slightly more aligned with $\vec{H}$ than its counterpart with spherical monomers.

While a single filament with ferromagnetic monomers, in a normal magnetic field, stabilizes with a given alignment angle θ with respect to the flow direction, where θ is a function of H and W, MFs with super-paramagnetic monomers exhibit a far more interesting phenomenology. Super-paramagnetic MNPs have an internal relaxation mechanism and are magnetizable both by applied magnetic fields and the dipole fields of other MNPs in their environment. Because of this, MFs with super-paramagnetic monomers can access and persist in bent conformations impossible for their counterparts with ferromagnetic monomers.

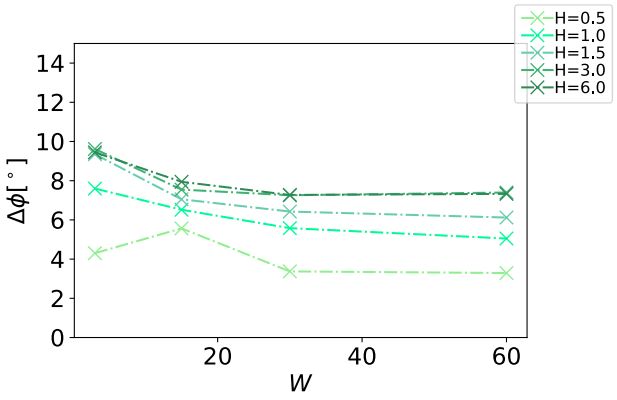

(a)

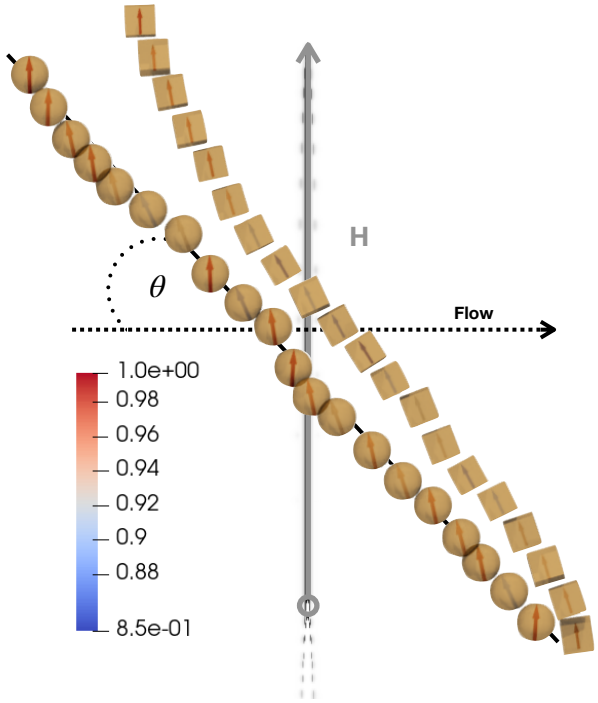

(b)

Figure 36: (a) showing the difference in ϕ between sMFs and cMFs with ferromagnetic monomers, denoted as $\Delta\phi$, as a function of W, for different H. (b) showing conformation snapshots with monomer dipole moments, corresponding to the $(W = 3; H = 6)$ parameter set, which is the point of largest $\Delta\phi$, presented in (a). Here, we also annotate magnetic field applied, flow direction, and the angle θ.

Looking in Fig. 37a, we see that the alignment angle θ tells a very different story for MFs with super-paramagnetic monomers. The overall shape of $\theta(W)$ curves is similar to the ones seen for MFs with ferromagnetic monomers in Fig. 35. However, they are grouped by monomer shape, rather than by field strength. We see a larger θ, for sMFs than cMFs, across the W range we explored. Furthermore, θ drops precipitously with increasing W, where sMFs seem to platoe around $\theta = 20^\circ$ while cMFs essentially align the backbone with the flow direction. The error bars in Fig. 37a suggest that the averages presented are representative. However, it is revealing to consider the variance of θ, as a function of H and/or W, shown in Fig. 37b.

For a given monomer shape, θ does not scale with H, but its variance does. sMFs with super-paramagnetic monomers vary more in θ than cMFs, across the range or parameters we explored. In the $W < 15$ (low shear) region, increasing H slightly decreases the variance of θ. This region coincides with the highest θ in Fig. 37a. This data point has wider error bars than any other one in Fig. 37. For low W and H we can attribute much of the variance to thermal fluctuations. As Zeeman coupling becomes stronger with increasing H, we enter the range where shear forces are low enough that MFs establish relatively persistent conformations. However, MFs with super-paramagnetic monomers tend to bend the backbone as they try to alight themselves along $\vec{H}$ and get stuck in conformations that correspond to local energy minima. This explains the wide error bars we see for $W = 3$ in Fig. 37a. Increasing H tends to increase the cost of escaping such local minima in the conformational spectrum, which is why we see a decrease in variance.

However, past the $W < 15$ region, we see inverse trends. Hydrodynamic torques become strong enough to compete with magnetic torques and filaments enter the buckling instability regime. Variance decreases with increasing W as the hydrodynamic interactions facilitate filament extension along the flow direction. Meanwhile, magnetic dipoles attempt to establish a favorable configuration along $\vec{H}$, and due to Zeeman coupling, variance increases with increasing H. For cMFs with super-paramagnetic monomers, while we see a similar trend, where an increase in W decreases variance, we do not capture a systematic scaling with H. Inspection of variance of θ, shown in Fig. 37b reveals that a single filament with super-paramagnetic monomers rotates in shear flow even when exposed to a normal magnetic field, and it does so with important differences based on its monomer shape.

Deeper insight into the mechanism responsible for the variance of θ and why it is monomer shape dependent we obtain by looking at the angle between filament $\vec{\mu}_{tot}$ and $\vec{H}$, denoted as ϕ, as a function of W and H, shown in Fig. 38a. An idealized representation of the magnetic nature of super-paramagnetic MNPs, where one discards

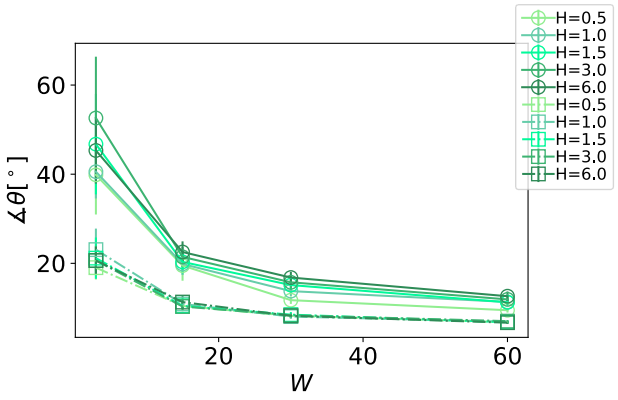

(a)

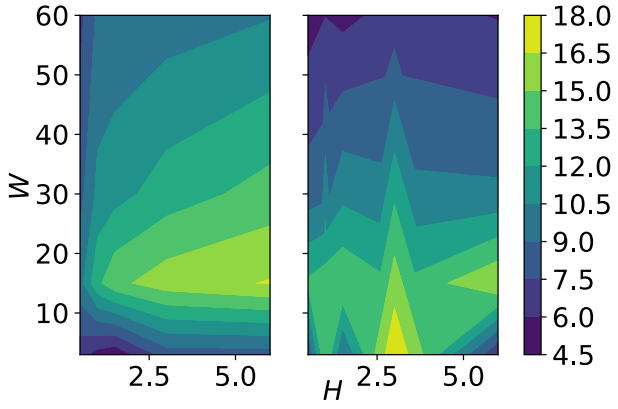

(b)

Figure 37: (a) showing a comparison in angle θ between sMFs and cMFs with super-paramagnetic monomers, for different H, as a function of W. Symbol shape corresponds to monomer shape. Error bars are calculated as the standard deviation of θ, across independent runs.(b) showing contour plots of the variance of θ. The contour plot on the left is showing results for sMFs, while the contour plot on the right is showing results for cMFs.

the magnetization effects of dipole fields, would have dipole moments fully aligned with $\vec{H}$. In other words, dipole moments in such MNPs reorient instantaneously and have magnitudes in accordance with the Langevin magnetization law. Looking at Fig. 38a, $\vec{\mu}_{tot}$ for cMFs is overall more aligned with $\vec{H}$ than for sMFs. The difference in ϕ decreases with increasing W. Interestingly, an increase in W aligns $\vec{\mu}_{tot}$ with $\vec{H}$ more, which is initially rather counter-intuitive. However, in relation with Fig. 37b, it can be understood that high W favors filament conformations aligned with the flow direction, causing a decrease in variance. The flow profile constrains the translational motion of monomers to the flow-vorticity plane, decreasing variance in the normal direction. As a result, the dipolar field configuration is more homogeneous, increasing the alignment of $\vec{\mu}_{tot}$ with $\vec{H}$. In the case of cMFs, additional steric restrictions compared to sMFs, reduce dipole field fluctuations further. Therefore, we see that $\vec{\mu}_{tot}$ for cMFs is overall more aligned with the $\vec{H}$. This is further corroborated with the variance of ϕ, shown in Fig. 38b. Overall, magnetic moment orientation is quite robust against time, where we see significant variance only for low H. It takes a moderately strong magnetic field to constrain the variance of ϕ for MFs with super-paramagnetic monomers within 5°. Analogously to what we have seen in Fig. 37b, cubic monomer shape also leads to less overall variance of ϕ. With increasing Zeeman coupling, we can also see a moderating effect on the variance of ϕ with increasing W.

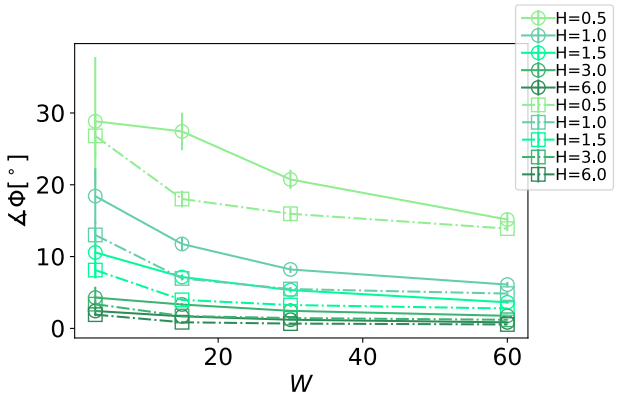

(a)

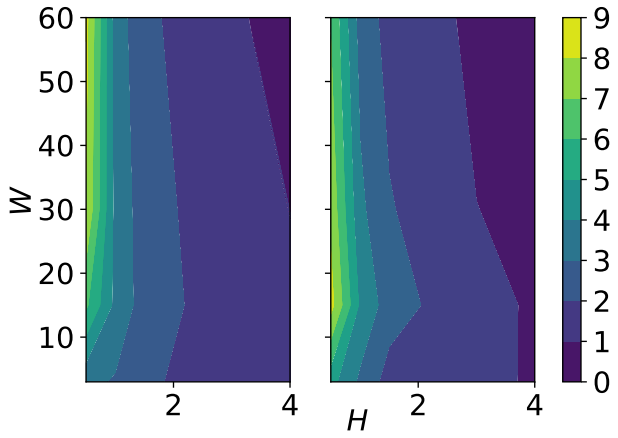

(b)

Figure 38: (a) showing the angle Φ as a function of W, and its scaling with field strength H, for MFs with super-paramagnetic monomers. Symbol shape corresponds to monomer shape. Error bars are calculated as the standard deviation of Φ, across independent runs. (b) showing contour plots of the variance of Φ. The contour plot on the left is showing results for sMFs, while the contour plot on the right is showing results for cMFs.

16

IN-FIELD TUMBLING OF MFS WITH SUPER-PARAMAGNETIC MONOMERS

In Chapter 15, we brought forward that MFs with super-paramagnetic monomers can persist in bent backbone conformations corresponding to local minima in their free energy spectrum, in low W shear flow, regardless of monomer shape. However, with increasing W, MFs with super-paramagnetic monomers start to rotate. Filaments with cubic monomers are mostly aligned with the flow direction, while filaments with spherical monomers are not, even for the highest W we explored. Furthermore, the variance of θ increases with H for sMFs, which suggests that the conformational instability for sMFs correlates with field strength. For cMFs this does not seem to be the case. Lastly, magnetic moments in cMFs with super-paramagnetic monomers are more aligned with $\vec{H}$ than in sMFs. Increase of H and/or W, aligns $\vec{\mu}_{tot}$ more with $\vec{H}$, and reduces variance, regardless of monomer shape. We can infer that the reorientational mechanism of a single filament with cubic, super-paramagnetic monomers in shear flow and normal magnetic fields must look quite different from what it looks like for its counterpart with spherical monomers.

In Fig. 39e, one can see the reorientational dynamics captured in simulations for sMFs and cMFs with super-paramagnetic monomers, establishing that MFs with super-paramagnetic monomers tumble in shear flow even in normal magnetic fields. Due to the internal relaxation and magnetization of super-paramagnetic monomers, sMFs assume bent, coiled up and collapsed conformations. Cubic monomer shape in cMFs restricts the phase-space of accessible conformations and stops the backbone from collapsing. Conformations depicted in Fig. 39e are all examples of tumbling. However, these are vastly different kinds of tumbling. It is important to have in mind that the collapsed conformations characteristic for sMFs with super-paramagnetic monomers are not assumed and held together only by entropy, but are also favored by magnetic interactions. Therefore, such collapsed conformations are not analogous to coiling.

We characterize the effects of monomer shape on tumbling using the diagonal elements of the gyration tensor to construct a cross-correlation function in the flow-field plane $C_{xz}(t)$,

$$C_{xz}(t) = \frac{< \delta G_{xx}(0) \delta G_{zz}(t) >}{\sqrt{< \delta G_{xx}^2(0) >< \delta G_{zz}^2(0) >}}$$

where $\delta G_{ab} = G_{ab} - < G_{ab} >$, is the component-wise fluctuation of G_{ab} around its mean. Generally, polymers and polymer-like systems in shear flow expand in the flow direction, with their motion

mostly constrained in the flow-vorticity plane. However, this is entropically rather unfavorable. Thermal fluctuations lead to stochastic extensions of the polymer in the normal direction, where due to the flow, the polymer experiences torque. As a result, the polymer coils, flips around, and subsequently extends again. In other words, it tumbles. Tumbling dynamics are characterized by a strong anticorrelation peak in the C_{xz}, and a correlation peak for negative lags. Given the stochastic nature of the process outlined above, C_{xz} correlations decay very quickly, implying that tumbling dynamics are cyclic rather than periodic. Filaments with super-paramagnetic monomers, however, have Zeeman coupling as an additional driving mechanism. Fig. 39 shows a C_{xz} comparison between sMFs and cMFs with super-paramagnetic monomers, with and without an external magnetic field applied ($H = 0$ or $H = 6$), at different shear rates $W \in \{3, 15, 30, 60\}$.

Looking at Fig. 39a, we see a typical C_{xz} of a polymer, as super-paramagnetic monomers have no remanent magnetization without an external magnetic field applied. We see that at $H = 0$, sMFs with super-paramagnetic monomers tumble in a cyclic fashion. Their characteristic time of tumbling scales just like it does for individual linear polymers, where $\tau_{tb} \propto W^{-2/3}$.[197] The anticorrelation peak signifies that a contraction along the flow direction is reflected in the extension in the field direction, and vice versa. In other words, as the chain tumbles, it coils. The correlation peak for negative lags relates that collapsed states along the flow are correlated with previous collapsed states along $\vec{H}$. The situation changes substantially with a strong $H = 6$ normal magnetic field. As can be seen in Fig. 39b, the slowly decaying anti-correlation peak in low shear ($W = 3$) shifts several characteristic time scales τ_r. As we increase W, we reproduce C_{xz} profiles that signal tumbling. However, τ_{tb} does not scale with W as it did for $H = 0$, and C_{xz} profiles for high W seem to be damped. As we have previously stated, MFs with super-paramagnetic monomers tend to bend their backbone as they align with $\vec{H}$, instead of rotating as a whole. For low shear, orientation of MFs is mostly determined by Zeeman coupling, and it can be understood that instead of reorientation, sMFs bend, as they follow the flow. Therefore, in addition to a shifted anticorrelation peak, we see a slowly decaying, pronounced correlation peak for negative lags. With increasing W, hydrodynamic forces become strong enough that conformations enforced by Zeeman coupling cannot persist, and filaments start to tumble. However, for high W, the filament backbone collapses in to semi-persistent, coiled up conformations, as depicted in Fig. 39e. These conformations are held together by magnetic forces in addition to entropy. This would not be possible without the magnetization effects of the dipole fields, as such conformations would be magnetically extremely unfavorable, and the chain would break apart. Furthermore, these conformations

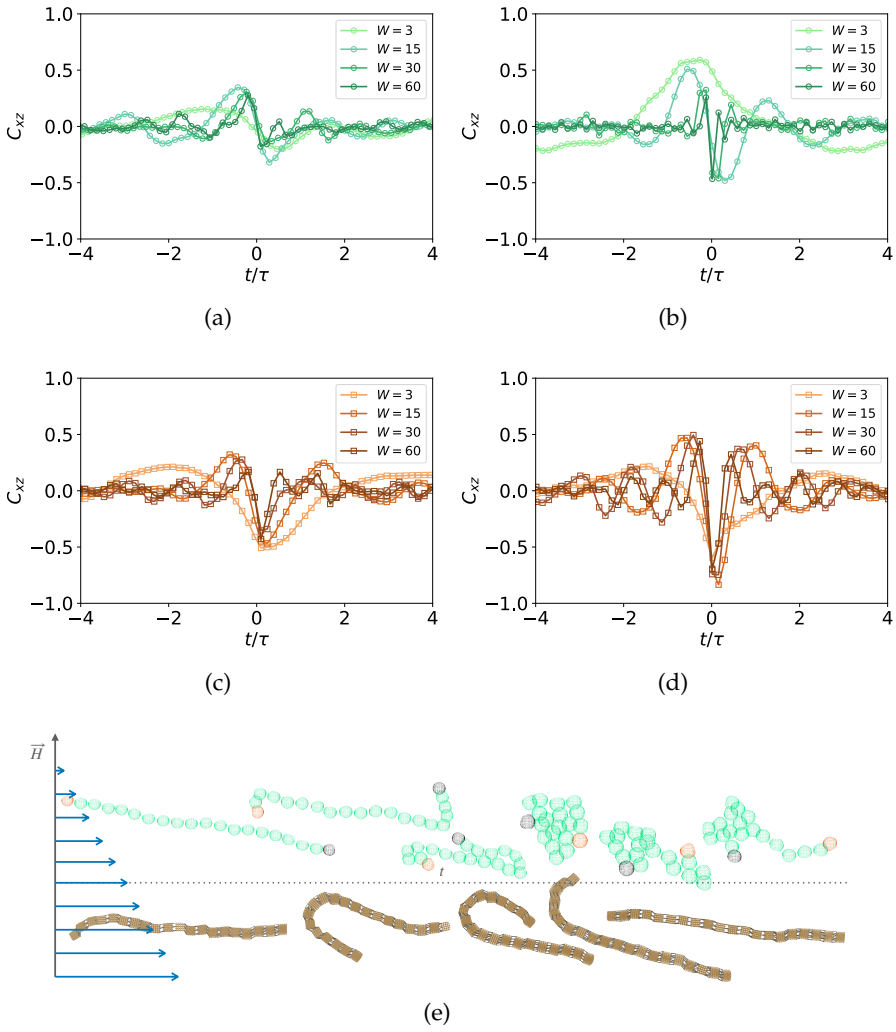

Figure 39: Showing a comparison of C_{xz} for sMFs and cMFs with super-paramagnetic monomers, with and without an external magnetic field applied ($H = 0$ or $H = 6$), at different shear rates $W \in \{3, 15, 30, 60\}$. Time is normalized by the characteristic relaxation time τ for each filament model, defined as the time it takes for the autocorrelation function of the radius of gyration to decay in a thermalized fluid. Symbol shape corresponds to monomer shape. (a) & (b) showing results for sMFs; (c) & (d) showing results for cMFs. (a) and (c) showing results for $H = 0$; (b) and (d) showing results for $H = 6$. (e) Simulation snapshots that capture of the reorientational dynamics exhibited by sMFs (up) and cMFs (down) with super-paramagnetic monomers, in shear flow $W = 30$ and external magnetic field applied in the gradient direction $H = 3.0$.

have dynamics of their own. They rotate as a whole and slowly unwind as shear tries to break the "globule" apart. Therefore, we see damped C_{xz} profiles, as characteristic times are influenced by eigenmodes of oscillation of the coiled structure, which correspond to

much higher frequencies. In fact, fitting the region $30 \leqslant W \leqslant 60$ with a power law we get $\tau_{tb} \propto W^{-1.1}$.

Looking at C_{xz} profiles for cMFs without an external magnetic field applied, shown in Fig. 39c, it is apparent that monomer shape has a tremendous impact on the dynamics of MFs in shear flow. For low shear $W = 3$, C_{xz} does not suggest that there is tumbling. Steric constrains imposed by cubic monomer shape inhibit coiling and tumbling. Therefore, τ_{tb} is shifted outside our simulation window. With increasing W, tumbling resumes, but with an overall higher τ_{tb} than for sMFs. Furthermore, we see that the C_{xz} profiles are overall more symmetric. This is interesting, as the overall symmetry of the profile can tell us a lot about how the tumbling motion looks like. As stated before, a C_{xz} correlation peak for negative lags says that a collapsed state along the flow direction is correlated with a previous collapsed state along the field direction. A C_{xz} correlation peak for positive lags on the other hand signifies that a collapsed state along the flow direction is correlated to a future collapsed state along the field direction. For sMFs, the asymmetry between the correlation peaks for positive and negative lags is there because during tumbling, once the filament coils, it tends to stay coiled or some time, in an entropically favorable configuration. However, cubic monomers make coiling difficult. Instead, cMFs tumble in a distinct bend and flip motion, as depicted Fig. 39e. Therefore, correlation peaks for both positive and negative lags are more symmetric for cMFs than they are for sMFs. Finally, once we turn on the magnetic field, while we maintain the overall shape of the profiles and do not seem to affect τ_{tb}, we intensify the correlations. Furthermore, cross-correlations decay more slowly. This means that, external magnetic field makes the reorientation of cMFs with super-paramagnetic monomers more periodic.

Further proof of our reasoning can be seen in the frequency spectrum of θ. In Fig. 40, we show the occurrence of frequencies $N(f)$, calculated by Fourier analysis of the time evolution of θ, between sMFs and cMFs with super-paramagnetic monomers, for different W. While τ_{tb} estimated from C_{xz} gives us information about the frequency of the tumbling, $N(f)$ tells us how frequent this tumbling is. Looking at Fig. 40a, for sMFs we see that with increasing W, $N(f)$ shifts to higher frequencies. Without an external magnetic field applied, the spectrum is rather smooth which suggests a lack of periodicity, regardless of W. Turning on an external magnetic field changes the $N(f)$ distribution tremendously. For low shear $W \in \{3, 15\}$, preferred frequencies become more apparent but do not change substantially in comparison to the left figure. However, for higher $W \in \{30, 60\}$ values, we see that the dominant frequencies change substantially. This corresponds the collapsed conformations of sMFs with super-paramagnetic monomers. The high frequencies correspond to the oscillation eigenmodes of these globular structures that seem to

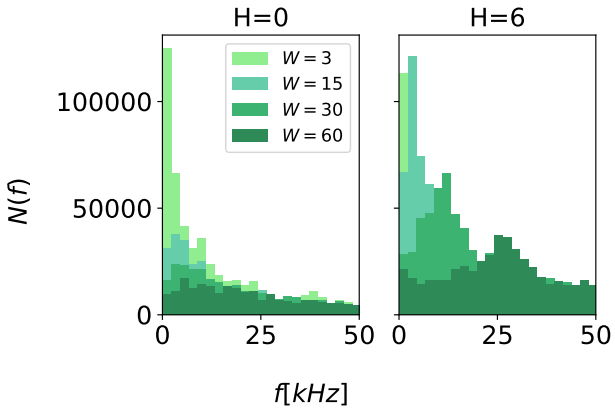

(a)

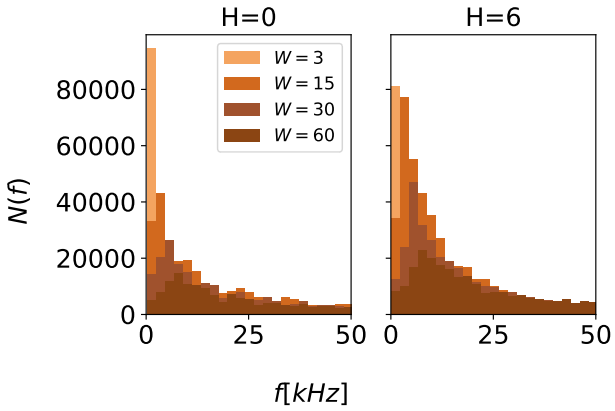

(b)

Figure 40: Frequency occurrence N(f) comparison between sMFs and cMFs with super-paramagnetic monomers, for different *W*. (a) is showing results for sMFs in shear flow with (right; H=6) and without (left; H=0) an external magnetic field applied perpendicular to the flow direction.(b) is showing results for cMFs in shear flow with (right; H=6) and without (left; H=0) an external magnetic field applied perpendicular to the flow direction.

be the dominant reorientational mode. It is important to note that this does not eliminate tumbling as such. Rather, oscillation eigenmodes of these globular structures are intertwined with tumbling. Consequently, the complexity of the dynamics exhibited by sMFs with super-paramagnetic monomers restricts how controllable they can be by magnetic fields in shear flow. To this end, as can be seen in Fig. 40b, super-paramagnetic monomers with cubic shape have a distinct advantage. Without an external magnetic field applied, N(f) of preferred reorientational modes is higher for cMFs than for sMFs, regardless of shear. Additional steric constraints imposed by monomer cubicity restrict the phase-space of accessible conformations. Turning on the external magnetic field makes the intensity of the preferred reorientational mode stand out even more. Cubic monomers preclude

the possibility that the backbone collapses like it does for sMFs. For a strong magnetic field, the main driving mechanism of the reorientation is Zeeman coupling, which restricts the phase-space even more, and makes the tumbling more periodic.

17

CONCLUSION AND OUTLOOK

While this chapter denotes the end the thesis, it most definitely does not suggest that research of MFs at a fundamental level is anywhere near being complete. The author certainly attempted to shed light on the phenomenology that MFs exhibit and pave ways for researchers to harness their potential. Starting with simple and general bead-spring models, we explored various designs of MFs, focusing on the most promising candidates for further scrutinization. We investigated how does the way MNPs are crosslinked to form a filament, and the way they are arranged along the filament backbone, reflect on the magnetoresponsiveness of MFs, using ferrofluids as a reference. Magnetoresponsiveness of MFs decreases significantly as the average inter-monomer distance increases. Therefore, a uniform distribution of MNPs crosslinked with short linkers is preferable. However, structural inhomogeneities do not affect the responsiveness of MFs to applied magnetic fields as strongly as one might expect. It is useful to think about crosslinking in terms of inter-monomer correlations. Inter-monomer correlations are intensified by long range, dipole-dipole interactions, and percolate through the backbone, helping MFs maintain a desirable magnetic response (compared to semi-dilute ferrofluids). Formally, crosslinking of MNPs forms the backbone of a magnetic filament. However, the essence of crosslinking is to couple the degrees of freedom between monomers. Therefore, crosslinking approaches can in general be distinguished based on whether they couple only the translational degrees of freedom or both the translational and rotational degrees of freedom of monomers. Which degrees of freedom are coupled not only affects the magnetoresponsiveness of MFs, but also affects what kind of magnetic response they have. In other words, one should consider the magnetic nature of monomers within a filament together with crosslinking, in order to obtain the desired magnetic response.

When it comes to the magnetic nature of MNPs one could use to synthesize MFs, we considered ferromagnetic nanoparticles, with a large and permanent magnetic moment without the necessity for an applied magnetic field, and perfectly polarizable, super-paramagnetic nanoparticles, with no remanent magnetization outside an applied magnetic field. Regardless of the magnetic nature of MNPs within them, MFs with crosslinking that couples both the translational and rotational degrees of freedom of monomers, have much improved responsiveness to external magnetic fields compared to conventional ferrofluids. Furthermore, MFs with super-paramagnetic monomers

tend to bend their backbone in applied magnetic fields, which is a tendency that has not only entropic, but also energetic advantages, especially for long filaments. In general, we focused on pinpointing the physical interactions that govern and determine the phenomenology of MFs. In a lab, however, MFs will be subjected to a multitude of experimental factors that could affect the expected response greatly. We treated the effects of νdW and/or electrostatic forces in a potential suspenspension of MFs by looking at a single filament with super-paramagnetic monomers and a central attraction between its monomers. In this way, we established general guidelines applicable to any magnetic filament design and set expectations for the equilibrium properties of MFs in a multitude of environments.

Having established best practice criteria for filament design, encompassing crosslinking, magnetic nature of monomers, microstructure, and effects of central attraction in a solution, we proposed a prospective design of MFs, based on experimentally realized systems, namely, nanopolymers synthesized through directional assembly of DNC nanoobjects. We revealed that DNC-based nanopolymers represent a compelling, finely tunable platform for creating highly magneto-responsive MFs, with unique structural properties. We scrutinized the mechanical resistance of DNC MFs to compression, revealing that cubic monomer shape proves to be advantageous, compared to MFs with spherical monomers, with a smoother and more controllable response. Furthermore, we investigated the rheology and dynamics of MFs subjected to the simultaneous action of shear flow and a stationary external magnetic field perpendicular to the flow. We showed that MFs can exhibit vastly different and systematically controllable behaviors. MFs tumble in shear flow. Applying an external magnetic field perpendicular to the flow direction, eliminates tumbling of MFs with ferromagnetic monomers. However, tumbling of a filament with super-paramagnetic monomers can be eliminated with a magnetic field perpendicular to the flow direction only in low shear. Backbone bending tendencies of MFs with super-paramagnetic monomers restrict how controllable they can be with magnetic fields in shear flow. DNC MFs have a distinct advantage to this end. Cubic monomer shape stops the backbone form collapsing. Instead, DNC MFs tumble in a distinct bend and flip motion. Occurrence of such motion can be enhanced by applying external magnetic fields.

The conclusions we made throughout this thesis, on the level of a single filament, should generalize well to filament suspensions. However, there is plenty left unexplored on that front. Sampling the free energy spectrum of DNC MFs that leads to the dynamics we outlined in this work and investing if and how these dynamics depend on filament length remains to be done. In general, there is much to be understood about the behavior of MFs in non-homogeneous, rotating or alternating magnetic fields. Initially, this thesis was not supposed

to be about MFs, but systems based on them. However, there was simply too much to be said on the level of a single filament, and a seemingly simple, but compelling story to be told. Having studied the exciting phenomenology of a single magnetic filament, it is truly exciting to see what can be done with them, when compelling MFs with a flexible backbone and a highly tunable micro- and nanostructure, become a reality. Eventually, such MFs could be used to build more elaborate magneto-responsive, soft matter systems, such as permanently crosslinked assembles of MFs into planar or spherical geometries. Furthermore, for spherical geometries, a particularly interesting idea is to combine Janus particles and MFs into superstructures we call Janus Brushes. The surface of a Janus particle has two or more distinct physical properties.[102, 206] This unique surface of a Janus particle allows two different types of chemistry to occur on the same particle. The simplest case of a Janus particle can be imagined if, for example one half of its surface is composed of hydrophilic groups and the other half hydrophobic groups.[65] In the Prologue of this thesis we stated that the 21st century could be called the Nanomaterial age. Mastering the design and harnessing the potential of magnetic filaments could very well be the development that solidifies that statement.

BIBLIOGRAPHY

[1] Nayan P Agarwal, Michael Matthies, Bastian Joffroy, and Thorsten L Schmidt. "Structural transformation of wireframe DNA origami via DNA polymerase assisted gap-filling." In: *ACS nano* 12.3 (2018), pp. 2546–2553.

[2] Patrick Ahlrichs and Burkhard Dünweg. "Lattice-Boltzmann simulation of polymer-solvent systems." In: *International Journal of Modern Physics C* 9.08 (1998), pp. 1429–1438.

[3] Patrick Ahlrichs and Burkhard Dünweg. "Simulation of a single polymer chain in solution by combining lattice Boltzmann and molecular dynamics." In: *The Journal of chemical physics* 111.17 (1999), pp. 8225–8239.

[4] T Aida, EW Meijer, and SI Stupp. "Functional supramolecular polymers." In: *Science* 335.6070 (2012), pp. 813–817.

[5] Berni Julian Alder and Thomas Everett Wainwright. "Phase transition for a hard sphere system." In: *The Journal of chemical physics* 27.5 (1957), pp. 1208–1209.

[6] Pietro Asinari. "Multiple-relaxation-time lattice Boltzmann scheme for homogeneous mixture flows with external force." In: *Physical Review E* 77.5 (2008), p. 056706.

[7] Anna C Balazs, Todd Emrick, and Thomas P Russell. "Nanoparticle polymer composites: where two small worlds meet." In: *Science* 314.5802 (2006), pp. 1107–1110.

[8] Markus B. Bannwarth, Stefanie Utech, Sandro Ebert, David A. Weitz, Daniel Crespy, and Katharina Landfester. "Colloidal Polymers with Controlled Sequence and Branching Constructed from Magnetic Field Assembled Nanoparticles." In: *ACS Nano* 9 (2015), pp. 2720–2728. DOI: 10.1021/nn5065327.

[9] M Belovs and A Cēbers. "Nonlinear dynamics of semiflexible magnetic filaments in an ac magnetic field." In: *Physical Review E* 73.5 (2006), p. 051503.

[10] M Belovs and A Cēbers. "Erratum: Ferromagnetic microswimmer [Phys. Rev. E 79, 051503 (2009)]." In: *Physical Review E* 79.6 (2009), p. 069906.

[11] Jason J. Benkoski, Steven E. Bowles, Ronald L. Jones, Jack F. Douglas, Jeffrey Pyun, and Alamgir Karim. "Self-assembly of polymer-coated ferromagnetic nanoparticles into mesoscopic polymer chains." In: *J Polym Sci, Part B: Polym Phy* 46.20 (2008), pp. 2267–2277. DOI: 10.1002/polb.21558.

[12] Jason J. Benkoski, Jennifer L. Breidenich, O. Manuel Uy, Allen T. Hayes, Ryan M. Deacon, H. Bruce Land, Jane M. Spicer, Pei Yuin Keng, and Jeffrey Pyun. "Dipolar organization and magnetic actuation of flagella-like nanoparticle assemblies." In: *J Mater Chem* 21 (20 2011), pp. 7314–7325. DOI: 10.1039/C0JM04014B.

[13] Mathieu Bennet, Luca Bertinetti, Robert K Neely, Andreas Schertel, André Körnig, Cristina Flors, Frank D Müller, Dirk Schüler, Stefan Klumpp, and Damien Faivre. "Biologically controlled synthesis and assembly of magnetite nanoparticles." In: *Faraday discussions* 181 (2015), pp. 71–83.

[14] Erik Benson, Abdulmelik Mohammed, Daniel Rayneau-Kirkhope, Andreas Gådin, Pekka Orponen, and Björn Högberg. "Effects of design choices on the stiffness of wireframe DNA origami structures." In: *ACS nano* 12.9 (2018), pp. 9291–9299.

[15] Éva Bereczk-Tompa, Ferenc Vonderviszt, Barnabás Horváth, István Szalai, and Mihály Pósfai. "Biotemplated synthesis of magnetic filaments." In: *Nanoscale* 9.39 (2017), pp. 15062–15069.

[16] Bhuvnesh Bharti, Anne-Laure Fameau, Michael Rubinstein, and Orlin D. Velev. "Nanocapillarity-mediated magnetic assembly of nanoparticles into ultraflexible filaments and reconfigurable networks." In: *Nature Materials* 14.11 (2015), pp. 1104–1109. ISSN: 1476-4660. DOI: 10.1038/nmat4364. URL: http://dx.doi.org/10.1038/nmat4364.

[17] Emanuela Bianchi, Gerhard Kahl, and Christos N. Likos. "Inverse patchy colloids: from microscopic description to mesoscopic coarse-graining." In: *Soft Matter* 7 (18 2011), pp. 8313–8323. DOI: 10.1039/C1SM05597F.

[18] Sibani Lisa Biswal and Alice P Gast. "Micromixing with linked chains of paramagnetic particles." In: *Analytical chemistry* 76.21 (2004), pp. 6448–6455.

[19] S J Blundell and F L Pratt. "Organic and molecular magnets." In: *J Phys-Condens Mat* 16 (2004), R771–R828. DOI: 10.1088/0953-8984/16/24/R03.

[20] Kaoutar Bouarnouna, Abdelkader Boutra, Karim Ragui, Nabila Labsi, and Youb Khaled Benkahla. "Multiple-relaxation-time lattice boltzmann model for flow and convective heat transfer in channel with porous media." In: *Journal of Statistical Physics* 174.5 (2019), pp. 972–991.

[21] Jennifer L. Breidenich, Michael C. Wei, Guy V. Clatterbaugh, Jason J. Benkoski, Pei Yuin Keng, and Jeffrey Pyun. "Controlling length and areal density of artificial cilia through the dipolar assembly of ferromagnetic nanoparticles." In: *Soft Matter* 8 (19 2012), pp. 5334–5341. DOI: 10.1039/C2SM25096A.

[22] Alex Buchberger, Chad R Simmons, Nour Eddine Fahmi, Ronit Freeman, and Nicholas Stephanopoulos. "Hierarchical assembly of nucleic acid/coiled-coil peptide nanostructures." In: *Journal of the American Chemical Society* 142.3 (2019), pp. 1406–1416.

[23] Eric Busseron, Yves Ruff, Emilie Moulin, and Nicolas Giuseppone. "Supramolecular self-assemblies as functional nanomaterials." In: *Nanoscale* 5.16 (2013), pp. 7098–7140.

[24] Julie Byrom, Patric Han, Michael Savory, and Sibani Lisa Biswal. "Directing Assembly of DNA-Coated Colloids with Magnetic Fields To Generate Rigid, Semiflexible, and Flexible Chains." In: *Langmuir* 30.30 (2014), pp. 9045–9052. DOI: 10.1021/la5009939.

[25] V Cabuil. "Phase behavior of magnetic nanoparticles dispersions in bulk and confined geometries." In: *Current opinion in colloid & interface science* 5.1-2 (2000), pp. 44–48.

[26] A. Cēbers. "Flexible magnetic filaments." In: *Curr Opin Colloid Interface Sci* 10.3-4 (2005), pp. 167–175. DOI: 10.1016/j.cocis.2005.07.002.

[27] A Cēbers and T Cīrulis. "Magnetic elastica." In: *Physical Review E* 76.3 (2007), p. 031504.

[28] A. Cēbers and I. Javaitis. "Dynamics of a flexible magnetic chain in a rotating magnetic field." In: *Phys Rev E* 69.2 (2004), p. 021404. DOI: 10.1103/PhysRevE.69.021404.

[29] Andrejs Cēbers. "Dynamics of a chain of magnetic particles connected with elastic linkers." In: *J. Phys.: Condens. Matter* 15.15 (2003), S1335. DOI: 10.1088/0953-8984/15/15/303.

[30] Andrejs Cebers. "Flexible magnetic filaments in a shear flow." In: *Journal of magnetism and magnetic materials* 300.1 (2006), pp. 67–70.

[31] Juan J. Cerdà, V. Ballenegger, O. Lenz, and C. Holm. "P3M algorithm for dipolar interactions." In: *J Chem Phys* 129 (2008), p. 234104. DOI: 10.1063/1.3000389.

[32] Wenduo Chen, Jizhong Chen, Lijun Liu, Xiaolei Xu, and Lijia An. "Effects of chain stiffness on conformational and dynamical properties of individual ring polymers in shear flow." In: *Macromolecules* 46.18 (2013), pp. 7542–7549.

[33] Wenduo Chen, Kexin Zhang, Lijun Liu, Jizhong Chen, Yunqi Li, and Lijia An. "Conformation and dynamics of individual star in shear flow and comparison with linear and ring polymers." In: *Macromolecules* 50.3 (2017), pp. 1236–1244.

[34] Wenduo Chen, Hongchao Zhao, Lijun Liu, Jizhong Chen, Yunqi Li, and Lijia An. "Effects of excluded volume and hydrodynamic interaction on the deformation, orientation and motion of ring polymers in shear flow." In: *Soft Matter* 11.26 (2015), pp. 5265–5273.

[35] S Chikazumi. *Physics of Ferromagnetism. Magnetic Characteristics and Practical Applications*. 1987.

[36] Won San Choi, Hye Young Koo, Ju Young Kim, and Wilhelm T. S. Huck. "Collective Behavior of Magnetic Nanoparticles in Polyelectrolyte Brushes." In: *Advanced Materials* 20.23 (2008), pp. 4504–4508. ISSN: 1521-4095. DOI: 10.1002/adma.200801423. URL: http://dx.doi.org/10.1002/adma.200801423.

[37] Laetitia Cohen-Tannoudji, Emanuel Bertrand, Lydie Bressy, Cécile Goubault, Jean Baudry, Jacob Klein, Jean François Joanny, and Jérôme Bibette. "Polymer Bridging Probed by Magnetic Colloids." In: *Phys. Rev. Lett.* 94 (3 2005), p. 038301. DOI: 10.1103/PhysRevLett.94.038301.

[38] Sheng Dai, Palaniswamy Ravi, and Kam Chiu Tam. "pH-Responsive polymers: synthesis, properties and applications." In: *Soft Matter* 4 (2008), pp. 435–449. DOI: 10.1039/B714741D.

[39] PG De Gennes and PA Pincus. "Pair correlations in a ferromagnetic colloid." In: *Physik der kondensierten Materie* 11.3 (1970), pp. 189–198.

[40] Pierre-Gilles De Gennes. *Scaling concepts in polymer physics*. Cornell university press, 1979.

[41] Peter Debye. "Einige resultate einer kinetischen theorie der isolatoren." In: *Physik Z.* 13 (1912), p. 97.

[42] Joshua M Dempster, Pablo Vázquez-Montejo, and Monica Olvera de la Cruz. "Contractile actuation and dynamical gel assembly of paramagnetic filaments in fast precessing fields." In: *Physical Review E* 95.5 (2017), p. 052606.

[43] Joe G. Donaldson and Sofia S. Kantorovich. "Directional self-assembly of permanently magnetised nanocubes in quasi two dimensional layers." In: *Nanoscale* 7 (2015), pp. 3217–3228. DOI: 10.1039/C4NR07101H.

[44] Joe G Donaldson, Per Linse, and Sofia S Kantorovich. "How cube-like must magnetic nanoparticles be to modify their self-assembly?" In: *Nanoscale* 9.19 (2017), pp. 6448–6462.

[45] P. S. Doyle. "Self-Assembled Magnetic Matrices for DNA Separation Chips." In: *Science* 295.5563 (2002), pp. 2237–2237. ISSN: 1095-9203. DOI: 10.1126/science.1068420. URL: http://dx.doi.org/10.1126/science.1068420.

[46] Patrick S Doyle, Jérôme Bibette, Aurélien Bancaud, and Jean-Louis Viovy. "Self-assembled magnetic matrices for DNA separation chips." In: *Science* 295.5563 (2002), pp. 2237–2237.

[47] Rémi Dreyfus, Jean Baudry, Marcus L. Roper, Marc Fermigier, Howard A. Stone, and Jérôme Bibette. "Microscopic artificial swimmers." In: *Nature* 437.7060 (2005), pp. 862–865. ISSN: 1476-4687. DOI: 10.1038/nature04090. URL: http://dx.doi.org/10.1038/nature04090.

[48] B Dünweg, P Ahlrichs, and R Everaers. "Dynamics-Lattice Boltzmann Scheme." In: *Computer Simulation Studies in Condensed-Matter Physics XIV: Proceedings of the Fourteenth Workshop, Athens, GA, USA, February 19–24, 2001*. Vol. 89. Springer Science & Business Media. 2012, p. 260.

[49] Ekaterina A Elfimova, Alexey O Ivanov, and Philip J Camp. "Static magnetization of immobilized, weakly interacting, superparamagnetic nanoparticles." In: *Nanoscale* 11.45 (2019), pp. 21834–21846.

[50] Barbara Elvers et al. *Ullmann's encyclopedia of industrial chemistry*. Verlag Chemie, 1991.

[51] K Ērglis, R Livanovičs, and A Cēbers. "Three dimensional dynamics of ferromagnetic swimmer." In: *Journal of Magnetism and Magnetic Materials* 323.10 (2011), pp. 1278–1282.

[52] K Ērglis, D Zhulenkovs, A Sharipo, and A Cēbers. "Elastic properties of DNA linked flexible magnetic filaments." In: *Journal of Physics: Condensed Matter* 20.20 (2008), p. 204107. ISSN: 1361-648X. DOI: 10.1088/0953-8984/20/20/204107. URL: http://dx.doi.org/10.1088/0953-8984/20/20/204107.

[53] B. A. Evans, A. R. Shields, R. Lloyd Carroll, S. Washburn, M. R. Falvo, and R. Superfine. "Magnetically Actuated Nanorod Arrays as Biomimetic Cilia." In: *Nano Lett* 7.5 (2007), pp. 1428–1434. DOI: 10.1021/nl070190c.

[54] Lang Feng, Rémi Dreyfus, Ruojie Sha, Nadrian C Seeman, and Paul M Chaikin. "DNA patchy particles." In: *Advanced Materials* 25.20 (2013), pp. 2779–2783.

[55] Richard P Feynman. "There's plenty of room at the bottom." In: *Engineering and science* 23.5 (1959).

[56] Richard Phillips Feynman, Robert B Leighton, and Matthew Linzee Sands. *Mainly electromagnetism and matter*. Vol. 2. Pearson PTR, 1989.

[57] Lukas P Fischer, Toni Peter, Christian Holm, and Joost de Graaf. "The raspberry model for hydrodynamic interactions revisited. I. Periodic arrays of spheres and dumbbells." In: *The Journal of chemical physics* 143.8 (2015), p. 084107.

[58] Shachar Frank and Paul C. Lauterbur. "Voltage-sensitive magnetic gels as magnetic resonance monitoring agents." In: *Nature* 363 (1993), pp. 334–336. DOI: 10.1038/363334a0.

[59] Uriel Frisch, Brosl Hasslacher, and Yves Pomeau. "Lattice-gas automata for the Navier-Stokes equation." In: *Physical review letters* 56.14 (1986), p. 1505.

[60] Eric M. Furst and Alice P. Gast. "Micromechanics of Dipolar Chains Using Optical Tweezers." In: *Phys Rev Lett* 82.20 (1999), pp. 4130–4133. DOI: 10.1103/PhysRevLett.82.4130.

[61] Eric M. Furst, Chiemi Suzuki, Marc Fermigier, and Alice P. Gast. "Permanently Linked Monodisperse Paramagnetic Chains." In: *Langmuir* 14.26 (1998), pp. 7334–7336. DOI: 10.1021/la980703i.

[62] Erik Gauger and Holger Stark. "Numerical study of a microscopic artificial swimmer." In: *Phys. Rev. E* 74 (2 2006), p. 021907. DOI: 10.1103/PhysRevE.74.021907.

[63] Michael Giersig, Gennady B Khomutov, et al. *Nanomaterials for application in medicine and biology*. Springer, 2008.

[64] C. Goubault, P. Jop, M. Fermigier, J. Baudry, E. Bertrand, and J. Bibette. "Flexible Magnetic Filaments as Micromechanical Sensors." In: *Phys. Rev. Lett.* 91 (2003), p. 260802. DOI: 10.1103/PhysRevLett.91.260802.

[65] Steve Granick, Shan Jiang, and Qian Chen. "Janus particles." In: *Phys. Today* 62.7 (2009), pp. 68–69.

[66] Gary S Grest and Kurt Kremer. "Molecular dynamics simulation for polymers in the presence of a heat bath." In: *Physical Review A* 33.5 (1986), p. 3628.

[67] Marek Grzelczak, Jan Vermant, Eric M Furst, and Luis M Liz-Marzán. "Directed self-assembly of nanoparticles." In: *ACS nano* 4.7 (2010), pp. 3591–3605.

[68] SP Gubin. "What is nanoparticle? Development trends for nanochemistry and nanotechnology." In: *Ross. Khim. Zh* 44.6 (2000), p. 23.

[69] SP Gubin and ID Kosobudskii. "Metal-clusters in polymer matrices." In: *Uspekhi khimii* 52.8 (1983), pp. 1350–1364.

[70] Sergei P Gubin, Yurii A Koksharov, GB Khomutov, and Gleb Yu Yurkov. "Magnetic nanoparticles: preparation, structure and properties." In: *Russian Chemical Reviews* 74.6 (2005), p. 489.

[71] Sergey P Gubin. *Magnetic nanoparticles*. John Wiley & Sons, 2009.

[72] Hugo C Hamaker. "The London—van der Waals attraction between spherical particles." In: *physica* 4.10 (1937), pp. 1058–1072.

[73] Lawrence J Hill and Jeffrey Pyun. "Colloidal polymers via dipolar assembly of magnetic nanoparticle monomers." In: *ACS applied materials & interfaces* 6.9 (2014), pp. 6022–6032.

[74] C. Holm and J.-J. Weis. "The structure of ferrofluids: A status report." In: *Curr Opin Colloid Interface Sci* 10 (2005), pp. 133–140. DOI: 10.1016/j.cocis.2005.07.005.

[75] Christian Holm and Kurt Kremer. *Advanced computer simulation approaches for soft matter sciences III*. Vol. 221. Springer, 2008.

[76] Chin-Yih Hong, IJ Jang, HE Horng, CJ Hsu, YD Yao, and Hong-Chang Yang. "Ordered structures in Fe 3 O 4 kerosene-based ferrofluids." In: *Journal of applied physics* 81.8 (1997), pp. 4275–4277.

[77] A Hosseinifar, M Shariaty-Niassar, SA Seyyed Ebrahimi, and M Moshref-Javadi. "Synthesis, characterization, and application of partially blocked amine-functionalized magnetic nanoparticles." In: *Langmuir* 33.51 (2017), pp. 14728–14737.

[78] Jiangtao Hu, Teri Wang Odom, and Charles M Lieber. "Chemistry and physics in one dimension: synthesis and properties of nanowires and nanotubes." In: *Accounts of chemical research* 32.5 (1999), pp. 435–445.

[79] Jinming Hu and Shiyong Liu. "Responsive polymers for detection and sensing applications: current status and future developments." In: *Macromolecules* 43.20 (2010), pp. 8315–8330.

[80] Shilin Huang, Giorgio Pessot, Peet Cremer, Rudolf Weeber, Christian Holm, Johannes Nowak, Stefan Odenbach, Andreas M Menzel, and Günter K Auernhammer. "Buckling of paramagnetic chains in soft gels." In: *Soft Matter* 12.1 (2016), pp. 228–237.

[81] AO Ivanov. "Magnetostatic properties of moderately concentrated ferrocolloids." In: *Magnitnaia Gidrodinamika* 28.4 (1992), pp. 39–46.

[82] Alexey O Ivanov and Olga B Kuznetsova. "Magnetic properties of dense ferrofluids: An influence of interparticle correlations." In: *Physical Review E* 64.4 (2001), p. 041405.

[83] Victor A. Ivanov and Julia A. Martemyanova. "Monte Carlo Computer Simulation of a Single Semi-Flexible Macromolecule at a Plane Surface." In: *Macromol Symp* 252.1 (2007), pp. 12–23. DOI: 10.1002/masy.200750602.

[84] Ivars Javaitis and Vineta Zilgalve. "Physics of Flexible Magnetic Filaments." In: *Adv Mat Res* 222 (2011), pp. 221–224. DOI: 10.4028/www.scientific.net/AMR.222.221.

[85] Angéla Jedlovszky-Hajdú, Francesca Baldelli Bombelli, Marco P. Monopoli, Etelka Tombácz, and Kenneth A. Dawson. "Surface Coatings Shape the Protein Corona of SPIONs with Relevance to Their Application in Vivo." In: *Langmuir* 28.42 (2012), pp. 14983–14991. ISSN: 1520-5827. DOI: 10.1021/la302446h. URL: http://dx.doi.org/10.1021/la302446h.

[86] Seung Heum Jeong, Jun Mo Kim, and Chunggi Baig. "Rheological influence of short-chain branching for polymeric materials under shear with variable branch density and branching architecture." In: *Macromolecules* 50.11 (2017), pp. 4491–4500.

[87] Florian D Jochum and Patrick Theato. "Temperature-and light-responsive smart polymer materials." In: *Chemical Society Reviews* 42.17 (2013), pp. 7468–7483.

[88] Matthew R Jones, Nadrian C Seeman, and Chad A Mirkin. "Programmable materials and the nature of the DNA bond." In: *Spherical Nucleic Acids* (2020), pp. 167–197.

[89] Richard Anthony Lewis Jones, Richard AL Jones, R Jones, et al. *Soft condensed matter*. Vol. 6. Oxford University Press, 2002.

[90] M Kamachi. "Magnetic polymers." In: *J Macromol Sci-Pol R* C42.4 (2002), pp. 541–561. DOI: 10.1081/MC-120015990.

[91] Sofia Kantorovich, Alexey O. Ivanov, Lorenzo Rovigatti, José Maria Tavares, and Francesco Sciortino. "Nonmonotonic Magnetic Susceptibility of Dipolar Hard-Spheres at Low Temperature and Density." In: *Phys. Rev. Lett.* 110 (2013), p. 148306. DOI: 10.1103/PhysRevLett.110.148306.

[92] Sofia Kantorovich, Elena Pyanzina, Cristiano De Michele, and Francesco Sciortino. "How to calculate structure factors of self-assembling anisotropic particles." In: *Soft Matter* 9 (2013), pp. 4412–4427. DOI: 10.1039/C3SM27895F.

[93] Sofia Kantorovich, Elena Pyanzina, and Francesco Sciortino. "The influence of shape anisotropy on the microstructure of magnetic dipolar particles." In: *Soft Matter* 9 (2013), pp. 6594–6603. DOI: 10.1039/C3SM50197C.

[94] Gennady B Khomutov, MN Antipina, AN Sergeev-Cherenkov, AA Rakhnyanskaya, M Artemyev, D Kisiel, RV Gainutdinov, AL Tolstikhina, and VV Kislov. "Organized planar nanostructures via interfacial self-assembly and DNA templating." In: *International Journal of Nanoscience* 3.01n02 (2004), pp. 65–74.

[95] Gennady B Khomutov and Yury A Koksharov. "Organized ensembles of magnetic nanoparticles: preparation, structure, and properties." In: *Magnetic Nanoparticles* (2009), pp. 117–195.

[96] Joseph L Kirschvink, Atsuko Kobayashi-Kirschvink, and Barbara J Woodford. "Magnetite biomineralization in the human brain." In: *Proceedings of the National Academy of Sciences* 89.16 (1992), pp. 7683–7687.

[97] Mark Klokkenburg, Ben H Erné, Johannes D Meeldijk, Albrecht Wiedenmann, Andrei V Petukhov, Roel PA Dullens, and Albert P Philipse. "In situ imaging of field-induced hexagonal columns in magnetite ferrofluids." In: *Physical review letters* 97.18 (2006), p. 185702.

[98] Slavko Kralj and Darko Makovec. "Magnetic assembly of superparamagnetic iron oxide nanoparticle clusters into nanochains and nanobundles." In: *ACS nano* 9.10 (2015), pp. 9700–9707.

[99] Steve Kuei, Burke Garza, and Sibani Lisa Biswal. "From strings to coils: Rotational dynamics of DNA-linked colloidal chains." In: *Physical Review Fluids* 2.10 (2017), p. 104102.

[100] Andrey A Kuznetsov. "Equilibrium properties of magnetic filament suspensions." In: *Journal of Magnetism and Magnetic Materials* 470 (2019), pp. 28–32.

[101] Chanseok Lee, Jae Young Lee, and Do-Nyun Kim. "Polymorphic design of DNA origami structures through mechanical control of modular components." In: *Nature communications* 8.1 (2017), pp. 1–8.

[102] Fan Li, David P Josephson, and Andreas Stein. "Colloidal assembly: the road from particles to colloidal molecules and crystals." In: *Angewandte Chemie International Edition* 50.2 (2011), pp. 360–388.

[103] Maximilian Liebetreu, Marisol Ripoll, and Christos N Likos. "Trefoil knot hydrodynamic delocalization on sheared ring polymers." In: *ACS Macro Letters* 7.4 (2018), pp. 447–452.

[104] Zhiwei Lin, Hamed Emamy, Brian Minevich, Yan Xiong, Shuting Xiang, Sanat Kumar, Yonggang Ke, and Oleg Gang. "Engineering organization of DNA nano-chambers through dimensionally controlled and multi-sequence encoded differentiated bonds." In: *Journal of the American Chemical Society* 142.41 (2020), pp. 17531–17542.

[105] Zhiwei Lin, Yan Xiong, Shuting Xiang, and Oleg Gang. "Controllable covalent-bound nanoarchitectures from DNA frames." In: *Journal of the American Chemical Society* 141.17 (2019), pp. 6797–6801.

[106] Wenyan Liu, Jonathan Halverson, Ye Tian, Alexei V Tkachenko, and Oleg Gang. "Self-organized architectures from assorted DNA-framed nanoparticles." In: *Nature chemistry* 8.9 (2016), pp. 867–873.

[107] Vladimir Lobaskin and Burkhard Dünweg. "A new model for simulating colloidal dynamics." In: *New Journal of Physics* 6.1 (2004), p. 54.

[108] Daniel Lüsebrink, Joan J Cerdà, Pedro A Sánchez, Sofia S Kantorovich, and Tomás Sintes. "The behavior of a magnetic filament in flow under the influence of an external magnetic field." In: *The Journal of chemical physics* 145.23 (2016), p. 234902.

[109] Mingliang Ma, Qiuyu Zhang, Jinbo Dou, Hepeng Zhang, Dezhong Yin, Wangchang Geng, and Yanyang Zhou. "Fabrication of one-dimensional Fe3O4/P(GMA–DVB) nanochains by magnetic-field-induced precipitation polymerization." In: *Journal of Colloid and Interface Science* 374.1 (2012), pp. 339–344. ISSN: 0021-9797. DOI: 10.1016/j.jcis.2012.02.015. URL: http://dx.doi.org/10.1016/j.jcis.2012.02.015.

[110] Robert J Macfarlane, Matthew N O'Brien, Sarah Hurst Petrosko, and Chad A Mirkin. "Nucleic acid-modified nanostructures as programmable atom equivalents: forging a new "table of elements"." In: *Angewandte Chemie International Edition* 52.22 (2013), pp. 5688–5698.

[111] Johannes Pall Magnusson, Adnan Khan, George Pasparakis, Aram Omer Saeed, Wenxin Wang, and Cameron Alexander. "Ion-sensitive "isothermal" responsive polymers prepared in water." In: *Journal of the American Chemical Society* 130.33 (2008), pp. 10852–10853.

[112] F. Martínez-Pedrero, M. Tirado-Miranda, A. Schmitt, and J. Callejas-Fernández. "Formation of magnetic filaments: A kinetic study." In: *Phys Rev E* 76.1 (2007), p. 011405. DOI: 10.1103/PhysRevE.76.011405.

[113] James Clerk Maxwell. "VIII. A dynamical theory of the electromagnetic field." In: *Philosophical transactions of the Royal Society of London* 155 (1865), pp. 459–512.

[114] KI Morozov. "Bull. Acad. Sci. USSR, Phys. Ser.(Engl. Transl.)" In: (1987).

[115] KI Morozov and AV Lebedev. "The effect of magneto-dipole interactions on the magnetization curves of ferrocolloids." In: *Journal of magnetism and magnetic materials* 85.1-3 (1990), pp. 51–53.

[116] Deniz Mostarac, Pedro A Sánchez, and Sofia Kantorovich. "Characterisation of the magnetic response of nanoscale magnetic filaments in applied fields." In: *Nanoscale* 12.26 (2020), pp. 13933–13947.

[117] Michi Nakata, Giuliano Zanchetta, Brandon D Chapman, Christopher D Jones, Julie O Cross, Ronald Pindak, Tommaso Bellini, and Noel A Clark. "End-to-end stacking and liquid crystal condensation of 6–to 20–base pair DNA duplexes." In: *Science* 318.5854 (2007), pp. 1276–1279.

[118] Louis Néel. "Théorie du traînage magnétique des ferromagnétiques en grains fins avec applications aux terres cuites." In: *Ann. géophys.* 5 (1949), pp. 99–136.

[119] Dorjderem Nyamjav and Albena Ivanisevic. "Templates for DNA-templated Fe3O4 nanoparticles." In: *Biomaterials* 26.15 (2005), pp. 2749–2757.

[120] Dmytro Nykypanchuk, Mathew M Maye, Daniel Van Der Lelie, and Oleg Gang. "DNA-guided crystallization of colloidal nanoparticles." In: *Nature* 451.7178 (2008), pp. 549–552.

[121] Kazuya Okada and Akira Satoh. "Evaluation of the translational and rotational diffusion coefficients of a cubic particle (for the application to Brownian dynamics simulations)." In: *Molecular Physics* 118.5 (2020), e1631498.

[122] Lars Onsager. "Electric moments of molecules in liquids." In: *Journal of the American Chemical Society* 58.8 (1936), pp. 1486–1493.

[123] Thomas E Ouldridge, Ard A Louis, and Jonathan PK Doye. "DNA nanotweezers studied with a coarse-grained model of DNA." In: *Physical Review Letters* 104.17 (2010), p. 178101.

[124] On Shun Pak, Wei Gao, Joseph Wang, and Eric Lauga. "High-speed propulsion of flexible nanowire motors: Theory and experiments." In: *Soft Matter* 7.18 (2011), pp. 8169–8181.

[125] Suchetan Pal, Zhengtao Deng, Baoquan Ding, Hao Yan, and Yan Liu. "DNA-Origami-Directed Self-Assembly of Discrete Silver-Nanoparticle Architectures." In: *Angewandte Chemie International Edition* 49.15 (2010), pp. 2700–2704. ISSN: 1433-7851. DOI: 10.1002/anie.201000330. URL: http://dx.doi.org/10.1002/anie.201000330.

[126] Bong Jun Park, Fei Fei Fang, and Hyoung Jin Choi. "Magnetorheology: materials and application." In: *Soft Matter* 6 (2010), pp. 5246–5253. DOI: 10.1039/C0SM00014K.

[127] Sung Yong Park, Abigail KR Lytton-Jean, Byeongdu Lee, Steven Weigand, George C Schatz, and Chad A Mirkin. "DNA-programmable nanoparticle crystallization." In: *Nature* 451.7178 (2008), pp. 553–556.

[128] V Adrian Parsegian. *Van der Waals forces: a handbook for biologists, chemists, engineers, and physicists*. Cambridge university press, 2005.

[129] Olga Philippova, Anna Barabanova, Vyacheslav Molchanov, and Alexei Khokhlov. "Magnetic polymer beads: Recent trends and developments in synthetic design and applications." In: *European polymer journal* 47.4 (2011), pp. 542–559.

[130] Roberto Piazza. *Soft matter: the stuff that dreams are made of*. Springer Science & Business Media, 2011.

[131] Zdenek Preisler, Teun Vissers, Gianmarco Munao, Frank Smallenburg, and Francesco Sciortino. "Equilibrium phases of one-patch colloids with short-range attractions." In: *Soft Matter* 10 (2014), pp. 5121–5128. DOI: 10.1039/C4SM00505H.

[132] Taisia A. Prokopieva, Victor A. Danilov, Sofia S. Kantorovich, and Christian Holm. "Ground state structures in ferrofluid monolayers." In: *Phys Rev E* 80.3 (2009), p. 031404. DOI: 10.1103/PhysRevE.80.031404.

[133] AF Pshenichnikov, VV Mekhonoshin, and AV Lebedev. "Magneto-granulometric analysis of concentrated ferrocolloids." In: *Journal of magnetism and magnetic materials* 161 (1996), pp. 94–102.

[134] Andrzej Rajca, Jirawat Wongsriratanakul, and Suchada Rajca. "Magnetic ordering in an organic polymer." In: *Science* 294.5546 (2001), pp. 1503–1505.

[135] Dennis C Rapaport. *The art of molecular dynamics simulation*. Cambridge university press, 2004.

[136] Marcus Reiner. "The deborah number." In: *Physics today* 17.1 (1964), p. 62.

[137] EL Resler and RE Rosensweig. "Magnetocaloric power." In: *AIAA Journal* 2.8 (1964), pp. 1418–1422.

[138] M Ripoll, RG Winkler, and G Gompper. "Star polymers in shear flow." In: *Physical review letters* 96.18 (2006), p. 188302.

[139] Flavio Romano and Francesco Sciortino. "Patchy from the bottom up." In: *Nature materials* 10.3 (2011), pp. 171–173.

[140] Marcus Roper, Rémi Dreyfus, Jean Baudry, Marc Fermigier, Jérôme Bibette, and Howard A Stone. "On the dynamics of magnetically driven elastic filaments." In: *Journal of Fluid Mechanics* 554 (2006), pp. 167–190.

[141] Marcus Roper, Rémi Dreyfus, Jean Baudry, Marc Fermigier, Jérôme Bibette, and Howard A Stone. "Do magnetic microswimmers move like eukaryotic cells?" In: *Proceedings of the Royal Society A: Mathematical, Physical and Engineering Sciences* 464.2092 (2008), pp. 877–904.

[142] Margaret Rosenberg, Frans Dekker, Joe G Donaldson, Albert P Philipse, and Sofia S Kantorovich. "Self-assembly of charged colloidal cubes." In: *Soft matter* 16.18 (2020), pp. 4451–4461.

[143] Ronald E Rosensweig. *Ferrohydrodynamics*. Courier Corporation, 2013.

[144] Paul W. K. Rothemund. "Folding DNA to create nanoscale shapes and patterns." In: *Nature* 440.7082 (2006), pp. 297–302. ISSN: 1476-4687. DOI: 10.1038/nature04586. URL: http://dx.doi.org/10.1038/nature04586.

[145] Paul WK Rothemund. "Folding DNA to create nanoscale shapes and patterns." In: *Nature* 440.7082 (2006), pp. 297–302.

[146] Lorenzo Rovigatti, Frank Smallenburg, Flavio Romano, and Francesco Sciortino. "Gels of DNA nanostars never crystallize." In: *ACS nano* 8.4 (2014), pp. 3567–3574.

[147] Debashish Roy, Jennifer N Cambre, and Brent S Sumerlin. "Biological- and Field-Responsive Polymers: Expanding Potential in Smart Materials." In: *Handbook of Stimuli-Responsive Materials* (2011), pp. 27–57.

[148] Michael Rubinstein and Ralph H. Colby. *Polymer Physics*. Oxford University Press, 2003.

[149] William Bailey Russel, WB Russel, Dudley A Saville, and William Raymond Schowalter. *Colloidal dispersions*. Cambridge university press, 1991.

[150] Jurij Sablić, Matej Praprotnik, and Rafael Delgado-Buscalioni. "Deciphering the dynamics of star molecules in shear flow." In: *Soft Matter* 13.29 (2017), pp. 4971–4987.

[151] Pedro A. Sánchez, Joan J. Cerdà, Tomás M. Sintes, Alexey O. Ivanov, and Sofia S. Kantorovich. "The effect of links on the interparticle dipolar correlations in supramolecular magnetic filaments." In: *Soft Matter* 11.15 (2015), pp. 2963–2972. ISSN: 1744-6848. DOI: 10.1039/c5sm00172b. URL: http://dx.doi.org/10.1039/C5SM00172B.

[152] Pedro A Sánchez, Joan J Cerda, Tomás M Sintes, Alexey O Ivanov, and Sofia S Kantorovich. "The effect of links on the interparticle dipolar correlations in supramolecular magnetic filaments." In: *Soft Matter* 11.15 (2015), pp. 2963–2972.

[153] Pedro A Sánchez, Joan J Cerdà, Tomás Sintes, and Christian Holm. "Effects of the dipolar interaction on the equilibrium morphologies of a single supramolecular magnetic filament in bulk." In: *The Journal of chemical physics* 139.4 (2013), p. 044904.

[154] Pedro A. Sánchez, Elena S. Pyanzina, Ekaterina V. Novak, Joan J. Cerdà, Tomas Sintes, and Sofia S. Kantorovich. "Supramolecular Magnetic Brushes: The Impact of Dipolar Interactions on the Equilibrium Structure." In: *Macromolecules* 48.20 (2015), pp. 7658–7669. ISSN: 1520-5835. DOI: 10.1021/acs.macromol.5b01086. URL: http://dx.doi.org/10.1021/acs.macromol.5b01086.

[155] Pedro A. Sánchez, Elena S. Pyanzina, Ekaterina V. Novak, Joan Josep Cerdà, Tomas Sintes, and Sofia S. Kantorovich. "Magnetic filament brushes: tuning the properties of a magnetoresponsive supramolecular coating." In: *Faraday Discuss.* 186 (2016), pp. 241–263. DOI: 10.1039/c5fd00133a.

[156] Debasish Sarkar and Madhuri Mandal. "Static and Dynamic Magnetic Characterization of DNA-Templated Chain-Like Magnetite Nanoparticles." In: *The Journal of Physical Chemistry C* 116.5 (2012), pp. 3227–3234. DOI: 10.1021/jp208020z.

[157] VK Sharma and F Waldner. "Superparamagnetic and ferrimagnetic resonance of ultrafine Fe3O4 particles in ferrofluids." In: *Journal of Applied Physics* 48.10 (1977), pp. 4298–4302.

[158] Valera P. Shcherbakov and Michael Winklhofer. "Bending of magnetic filaments under a magnetic field." In: *Phys. Rev. E* 70 (6 2004), p. 061803. DOI: 10.1103/PhysRevE.70.061803.

[159] Mark Isaakovich Shliomis. "Magnetic fluids." In: *Soviet Physics Uspekhi* 17.2 (1974), p. 153.

[160] Z.P. Shulman, V.I. Kordonsky, E.A. Zaltsgendler, I.V. Prokhorov, B.M. Khusid, and S.A. Demchuk. "Structure, physical properties and dynamics of magnetorheological suspensions." In: *International Journal of Multiphase Flow* 12.6 (1986), pp. 935–955. DOI: 10.1016/0301-9322(86)90036-4.

[161] Harpreet Singh, Paul E. Laibinis, and T. Alan Hatton. "Rigid, Superparamagnetic Chains of Permanently Linked Beads Coated with Magnetic Nanoparticles. Synthesis and Rotational Dynamics under Applied Magnetic Fields." In: *Langmuir* 21.24 (2005), pp. 11500–11509. DOI: 10.1021/la0517843.

[162] Harpreet Singh, Paul E. Laibinis, and T. Alan Hatton. "Synthesis of Flexible Magnetic Nanowires of Permanently Linked Core–Shell Magnetic Beads Tethered to a Glass Surface Patterned by Microcontact Printing." In: *Nano Lett* 5.11 (2005), pp. 2149–2154. DOI: 10.1021/nl051537j.

[163] AT Skjeltorp. "Ordering phenomena of particles dispersed in magnetic fluids." In: *Journal of Applied Physics* 57.8 (1985), pp. 3285–3290.

[164] Frank Smallenburg, Laura Filion, and Francesco Sciortino. "Erasing no-man's land by thermodynamically stabilizing the liquid–liquid transition in tetrahedral particles." In: *Nature physics* 10.9 (2014), p. 653.

[165] Hermann Staudinger. "Über polymerisation." In: *Berichte der deutschen chemischen Gesellschaft (A and B Series)* 53.6 (1920), pp. 1073–1085.

[166] Edmund Clifton Stoner and EP Wohlfarth. "A mechanism of magnetic hysteresis in heterogeneous alloys." In: *Philosophical Transactions of the Royal Society of London. Series A, Mathematical and Physical Sciences* 240.826 (1948), pp. 599–642.

[167] Zebin Su, Ruimeng Zhang, Xiao-Yun Yan, Qing-Yun Guo, Jiahao Huang, Wenpeng Shan, Yuchu Liu, Tong Liu, Mingjun Huang, and Stephen ZD Cheng. "The role of architectural engineering in macromolecular self-assemblies via non-covalent interactions: A molecular LEGO approach." In: *Progress in Polymer Science* 103 (2020), p. 101230.

[168] Dazhi Sun and Oleg Gang. "DNA-functionalized quantum dots: fabrication, structural, and physicochemical properties." In: *Langmuir* 29.23 (2013), pp. 7038–7046.

[169] Sha Sun, Shize Yang, Huolin L Xin, Dmytro Nykypanchuk, Mingzhao Liu, Honghu Zhang, and Oleg Gang. "Valence-programmable nanoparticle architectures." In: *Nature communications* 11.1 (2020), pp. 1–10.

[170] Yuki Suzuki, Ibuki Kawamata, Kohei Mizuno, and Satoshi Murata. "Large Deformation of a DNA-Origami Nanoarm Induced by the Cumulative Actuation of Tension-Adjustable Modules." In: *Angewandte Chemie International Edition* 59.15 (2020), pp. 6230–6234.

[171] Julie Thévenot, Hugo Oliveira, Olivier Sandre, and Sébastien Lecommandoux. "Magnetic responsive polymer composite materials." In: *Chem. Soc. Rev.* 42 (2013), pp. 7099–7116. DOI: 10.1039/C3CS60058K.

[172] Ye Tian, Julien R Lhermitte, Lin Bai, Thi Vo, Huolin L Xin, Huilin Li, Ruipeng Li, Masafumi Fukuto, Kevin G Yager, Jason S Kahn, et al. "Ordered three-dimensional nanomaterials using DNA-prescribed and valence-controlled material voxels." In: *Nature materials* 19.7 (2020), pp. 789–796.

[173] Ye Tian, Yugang Zhang, Tong Wang, Huolin L. Xin, Huilin Li, and Oleg Gang. "Lattice engineering through nanoparticle–DNA frameworks." In: *Nature Materials* 15.6 (2016), pp. 654–661. ISSN: 1476-4660. DOI: 10.1038/nmat4571. URL: http://dx.doi.org/10.1038/nmat4571.

[174] Rainer Tietze, Jan Zaloga, Harald Unterweger, Stefan Lyer, Ralf P Friedrich, Christina Janko, Marina Pöttler, Stephan Dürr, and Christoph Alexiou. "Magnetic nanoparticle-based drug delivery for cancer therapy." In: *Biochemical and biophysical research communications* 468.3 (2015), pp. 463–470.

[175] A. Tkachenko and Y. Rabin. "Coupling between Thermodynamics and Conformations in Wormlike Polymer Nematics." In: *Macromolecules* 28.25 (1995), pp. 8646–8656. DOI: 10.1021/ma00129a025. eprint: https://doi.org/10.1021/ma00129a025. URL: https://doi.org/10.1021/ma00129a025.

[176] Alexander Tokarev, Yu Gu, Andrey Zakharchenko, Oleksandr Trotsenko, Igor Luzinov, Konstantin G. Kornev, and Sergiy Minko. "Reconfigurable Anisotropic Coatings via Magnetic Field-Directed Assembly and Translocation of Locking Magnetic Chains." In: *Advanced Functional Materials* 24.30 (2014), pp. 4738–4745. ISSN: 1616-301X. DOI: 10.1002/adfm.201303358. URL: http://dx.doi.org/10.1002/adfm.201303358.

[177] David Toneian, Christos N Likos, and Gerhard Kahl. "Controlled self-aggregation of polymer-based nanoparticles employing shear flow and magnetic fields." In: *Journal of Physics: Condensed Matter* 31.24 (2019), 24LT02.

[178] Alex Travesset. "Soft skyrmions, spontaneous valence and selection rules in nanoparticle superlattices." In: *ACS nano* 11.6 (2017), pp. 5375–5382.

[179] AO Tsebers. "Thermodynamic stability of magnetofluids." In: *Magnetohydrodynamics* 18.2 (1982), pp. 137–142.

[180] George E Uhlenbeck and Leonard S Ornstein. "On the theory of the Brownian motion." In: *Physical review* 36.5 (1930), p. 823.

[181] Rein V. Ulijn. "Enzyme-responsive materials: a new class of smart biomaterials." In: *J. Mater. Chem.* 16 (2006), pp. 2217–2225. DOI: 10.1039/B601776M.

[182] Fernando Vargas-Lara, Francis W Starr, and Jack F Douglas. "Molecular rigidity and enthalpy–entropy compensation in DNA melting." In: *Soft Matter* 13.44 (2017), pp. 8309–8330.

[183] Pablo Vázquez-Montejo, Joshua M Dempster, and Mónica Olvera de la Cruz. "Paramagnetic filaments in a fast precessing field: Planar versus helical conformations." In: *Physical Review Materials* 1.6 (2017), p. 064402.

[184] Juan de Vicente, Daniel J. Klingenberg, and Roque Hidalgo-Alvarez. "Magnetorheological fluids: a review." In: *Soft Matter* 7 (2011), pp. 3701–3710. DOI: 10.1039/C0SM01221A.

[185] Thi Vo, Venkat Venkatasubramanian, Sanat Kumar, Babji Srinivasan, Suchetan Pal, Yugang Zhang, and Oleg Gang. "Stoichiometric control of DNA-grafted colloid self-assembly." In: *Proceedings of the National Academy of Sciences* 112.16 (2015), pp. 4982–4987.

[186] Hui Wang, Yifei Yu, Yubin Sun, and Qianwang Chen. "Magnetic Nanochains: a review." In: *Nano* 06.01 (2011), pp. 1–17. DOI: 10.1142/S1793292011002305.

[187] Hui Wang, Yifei Yu, Yubin Sun, and Qianwang Chen. "Magnetic nanochains: a review." In: *Nano* 6.01 (2011), pp. 1–17.

[188] Pengfei Wang, Ji-Hyeok Huh, Haedong Park, Donglei Yang, Yingwei Zhang, Yunlong Zhang, Jaewon Lee, Seungwoo Lee, and Yonggang Ke. "DNA Origami Guided Self-Assembly of Plasmonic Polymers with Robust Long-Range Plasmonic Resonance." In: *Nano Letters* 20.12 (2020), pp. 8926–8932.

[189] Yufeng Wang, Yu Wang, Dana R Breed, Vinothan N Manoharan, Lang Feng, Andrew D Hollingsworth, Marcus Weck, and David J Pine. "Colloids with valence and specific directional bonding." In: *Nature* 491.7422 (2012), pp. 51–55.

[190] Rudolf Weeber, Sofia Kantorovich, and Christian Holm. "Deformation mechanisms in 2D magnetic gels studied by computer simulations." In: *Soft Matter* 8.38 (2012), p. 9923. ISSN: 1744-6848. DOI: 10.1039/c2sm26097b. URL: http://dx.doi.org/10.1039/C2SM26097B.

[191] John D Weeks, David Chandler, and Hans C Andersen. "Role of repulsive forces in determining the equilibrium structure of simple liquids." In: *The Journal of chemical physics* 54.12 (1971), pp. 5237–5247.

[192] Jiachen Wei, Fan Song, and Jure Dobnikar. "Assembly of superparamagnetic filaments in external field." In: *Langmuir* 32.36 (2016), pp. 9321–9328.

[193] Florian Weik, Rudolf Weeber, Kai Szuttor, Konrad Breitsprecher, Joost de Graaf, Michael Kuron, Jonas Landsgesell, Henri Menke, David Sean, and Christian Holm. "ESPResSo 4.0–an extensible software package for simulating soft matter systems." In: *The European Physical Journal Special Topics* 227.14 (2019), pp. 1789–1816.

[194] Xiaogang Wen, Lin Gu, and Alexander M Bittner. "Simple Electroless Synthesis of Cobalt Nanoparticle Chains, Oriented by Externally Applied Magnetic Fields." In: *Zeitschrift für Physikalische Chemie* 232.9-11 (2018), pp. 1631–1646.

[195] Norman M Wereley, ed. *Magnetorheology. Advances and Applications*. RSC Smart Materials. The Royal Society of Chemistry, 2014, P001–396. ISBN: 978-1-84973-667-1. DOI: 10.1039/9781849737548.

[196] MSt Wertheim. "Exact solution of the mean spherical model for fluids of hard spheres with permanent electric dipole moments." In: *The Journal of Chemical Physics* 55.9 (1971), pp. 4291–4298.

[197] Roland G Winkler. "Semiflexible polymers in shear flow." In: *Physical review letters* 97.12 (2006), p. 128301.

[198] Roland G Winkler, Dmitry A Fedosov, and Gerhard Gompper. "Dynamical and rheological properties of soft colloid suspensions." In: *Current opinion in colloid & interface science* 19.6 (2014), pp. 594–610.

[199] Denis Wirtz and Marc Fermigier. "Periodic structures and substructures in magnetic suspensions." In: *Langmuir* 11.2 (1995), pp. 398–400.

[200] Younan Xia, Peidong Yang, Yugang Sun, Yiying Wu, Brian Mayers, Byron Gates, Yadong Yin, Franklin Kim, and Haoquan Yan. "One-dimensional nanostructures: synthesis, characterization, and applications." In: *Advanced materials* 15.5 (2003), pp. 353–389.

[201] Yan Xiong, Zhiwei Lin, Deniz Mostarac, Brian Minevich, Qiuyuan Peng, Guolong Zhu, Pedro A Sánchez, Sofia Kantorovich, Yonggang Ke, and Oleg Gang. "Divalent Multilinking Bonds Control Growth and Morphology of Nanopolymers." In: *Nano Letters* 21.24 (2021), pp. 10547–10554.

[202] Yan Xiong, Shize Yang, Ye Tian, Aaron Michelson, Shuting Xiang, Huolin Xin, and Oleg Gang. "Three-Dimensional Patterning of Nanoparticles by Molecular Stamping." In: *ACS nano* 14.6 (2020), pp. 6823–6833.

[203] Ying Xiong, Qianwang Chen, Nan Tao, Jing Ye, Yan Tang, Jiansheng Feng, and Xiaoyu Gu. "The formation of legume-like structures of Co nanoparticles through a polymer-assisted magnetic-field-induced assembly." In: *Nanotechnology* 18.34 (2007), p. 345301. ISSN: 1361-6528. DOI: 10.1088/0957-4484/18/34/345301. URL: http://dx.doi.org/10.1088/0957-4484/18/34/345301.

[204] Shao Hui Xu, Guang Tao Fei, Hao Miao Ouyang, Yao Zhang, Peng Cheng Huo, and Li De Zhang. "Controllable fabrication of nickel nanoparticle chains based on electrochemical corrosion." In: *Journal of Materials Chemistry C* 3.9 (2015), pp. 2072–2079.

[205] Tao Yang, Tonguc O Tasci, Keith B Neeves, Ning Wu, and David WM Marr. "Magnetic microlassos for reversible cargo capture, transport, and release." In: *Langmuir* 33.23 (2017), pp. 5932–5937.

[206] Zhenzhong Yang, Axel HE Muller, Chenjie Xu, Patrick S Doyle, Joesph M DeSimone, Joerg Lahann, Francesco Sciortino, Sharon Glotzer, Liang Hong, Dirk AL Aarts, et al. *Janus particle synthesis, self-assembly and applications*. Royal Society of Chemistry, 2012.

[207] Guangbao Yao, Jiang Li, Qian Li, Xiaoliang Chen, Xiaoguo Liu, Fei Wang, Zhibei Qu, Zhilei Ge, Raghu Pradeep Narayanan, Dewight Williams, et al. "Programming nanoparticle valence bonds with single-stranded DNA encoders." In: *Nature materials* 19.7 (2020), pp. 781–788.

[208] Chenglin Yi, Hong Liu, Shaoyi Zhang, Yiqun Yang, Yan Zhang, Zhongyuan Lu, Eugenia Kumacheva, and Zhihong Nie. "Self-limiting directional nanoparticle bonding governed by reaction stoichiometry." In: *Science* 369.6509 (2020), pp. 1369–1374.

[209] Reza M. Zadegan and Michael L. Norton. "Structural DNA Nanotechnology: From Design to Applications." In: *International Journal of Molecular Sciences* 13.6 (2012), pp. 7149–7162. ISSN: 1422-0067. DOI: 10.3390/ijms13067149. URL: http://dx.doi.org/10.3390/ijms13067149.

[210] Giuliano Zanchetta, Fabio Giavazzi, Michi Nakata, Marco Buscaglia, Roberto Cerbino, Noel A Clark, and Tommaso Bellini. "Right-handed double-helix ultrashort DNA yields chiral nematic phases with both right-and left-handed director twist." In: *Proceedings of the National Academy of Sciences* 107.41 (2010), pp. 17497–17502.

[211] Feng Zhang and Chang-Chun Wang. "Fabrication of One-Dimensional Iron Oxide/Silica Nanostructures with High Magnetic Sensitivity by Dipole-Directed Self-Assembly." In: *The Journal of Physical Chemistry C* 112.39 (2008), pp. 15151–15156. ISSN: 1932-7455. DOI: 10.1021/jp804452r. URL: http://dx.doi.org/10.1021/jp804452r.

[212] Wen-Bin Zhang, Xinfei Yu, Chien-Lung Wang, Hao-Jan Sun, I-Fan Hsieh, Yiwen Li, Xue-Hui Dong, Kan Yue, Ryan Van Horn, and Stephen ZD Cheng. "Molecular nanoparticles are unique elements for macromolecular science: From "nanoatoms" to giant molecules." In: *Macromolecules* 47.4 (2014), pp. 1221–1239.

[213] Yugang Zhang, Fang Lu, Kevin G. Yager, Daniel van der Lelie, and Oleg Gang. "A general strategy for the DNA-mediated self-assembly of functional nanoparticles into heterogeneous systems." In: *Nature Nanotechnology* 8.11 (2013), pp. 865–872. ISSN: 1748-3395. DOI: 10.1038/nnano.2013.209. URL: http://dx.doi.org/10.1038/nnano.2013.209.

[214] Yugang Zhang, Fang Lu, Kevin G Yager, Daniel Van Der Lelie, and Oleg Gang. "A general strategy for the DNA-mediated self-assembly of functional nanoparticles into heterogeneous systems." In: *Nature nanotechnology* 8.11 (2013), pp. 865–872.

[215] Jingjing Zhao, Di Du, and Sibani Lisa Biswal. "Nonlinear multimode buckling dynamics examined with semiflexible paramagnetic filaments." In: *Physical Review E* 98.1 (2018), p. 012602.

[216] Jianping Zheng, Jens J Birktoft, Yi Chen, Tong Wang, Ruojie Sha, Pamela E Constantinou, Stephan L Ginell, Chengde Mao, and Nadrian C Seeman. "From molecular to macroscopic via the rational design of a self-assembled 3D DNA crystal." In: *Nature* 461.7260 (2009), pp. 74–77.

[217] Zhihan Zhou, Guojun Liu, and Dehui Han. "Coating and Structural Locking of Dipolar Chains of Cobalt Nanoparticles." In: *ACS Nano* 3.1 (2008), pp. 165–172. ISSN: 1936-086X. DOI: 10.1021/nn8005366. URL: http://dx.doi.org/10.1021/nn8005366.

[218] Zhihan Zhou, Guojun Liu, and Dehui Han. "Coating and Structural Locking of Dipolar Chains of Cobalt Nanoparticles." In: *ACS Nano* 3.1 (2009), pp. 165–172. DOI: 10.1021/nn8005366.

[219] Miklós Zrınyi, Dénes Szabó, and Hanns-Georg Kilian. "Kinetics of the shape change of magnetic field sensitive polymer gels." In: *Polymer Gels and Networks* 6.6 (1998), pp. 441–454.